AD-768 652

ANALYTICAL MODELING OF LIQUID AND SOLID PARTICLE EROSION

William F. Adler

Bell Aerospace Company

Prepared for:

Air Force Material Laboratory

July 1973

Best
Available
Copy

NOTICE

When Government drawings, specifications, or other data are used for any
purpose other than in connection with a definitely related Government
procurement operation, the United States Government thereby incurs no
responsibility nor any obligation whatsoever; and the fact that the
government may have formulated, furnished, or in any way supplied the said
drawings, specifications, or other data, is not to be regarded by implication
or otherwise as in any manner licensing the holder or any other person
or corporation, or conveying any rights or permission to manufacture, use,
or sell any patented invention that may in any way be related thereto.
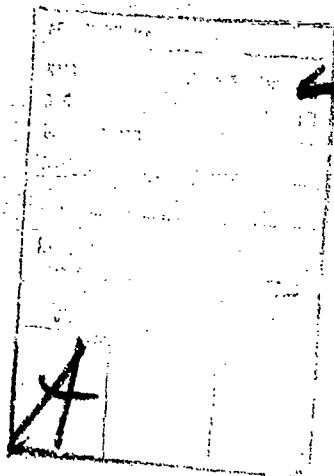
Copies of this report should not be returned unless return is required by
security considerations, contractual obligations, or notice on a specific
document.

ANALYTICAL MODELING OF LIQUID
AND SOLID PARTICLE EROSION

William F. Adler

Textron's Bell Aerospace Company

Technical Report AFML-TR-73-174

September 1973

Air Force Materials Laboratory
Air Force Systems Command
Wright -Patterson Air Force Base, Ohio

FOREWORD

This report was prepared by Bell Aerospace Company, Buffalo, New York 14240 under Air Force Contract F33615-71-C-1528. It was initiated under Project No. 7342, "Fundamental Research on Macromolecular Materials and Lubrication Phenomena," Task No. 734202, "Studies on the Structure-Property Relationships of Polymer Materials."

The work was administered under the direction of the Air Force Materials Laboratory, Air Force Systems Command, Wright-Patterson Air Force Base, Ohio with George F. Schmitt, Jr. of the Elastomers and Coatings Branch, Nonmetallic Materials Division, acting as project engineer.

This report covers the work carried out during the period from June 1972 through May 1973 and was submitted by the author in June 1973.

This technical report has been reviewed and is approved.

MERRILL L. MINGES, Acting Chief
Elastomers and Coatings Branch
Nonmetallic Materials Division
Air Force Materials Laboratory

AD 768652

DOCUMENT CONTROL DATA - R & D

(Security classification of title, body of abstract and indexing annotation must be entered when the overall report is classified)

1. ORIGINATING ACTIVITY (Corporate author)	2a. REPORT SECURITY CLASSIFICATION
Bell Aerospace Company Buffalo NY 14240	Unclassified
	2b. GROUP

3. REPORT TITLE

"Analytical Modeling of Liquid and Solid Particle Erosion"

4. DESCRIPTIVE NOTES (Type of report and inclusive dates)

Summary June 1972 - May 1973

5. AUTHOR(S) (First name, middle initial, last name)

William F. Adler

6. REPORT DATE	7a. TOTAL NO. OF PAGES	7b. NO. OF REFS
July 1973	185 *201*	40

8a. CONTRACT OR GRANT NO.	9a. ORIGINATOR'S REPORT NUMBER(S)
F33615-71-C-1528	
b. PROJECT NO. 7342	
c. Task No. 734202	9b. OTHER REPORT NO(S) (Any other numbers that may be assigned this report) AFML-TR-73-174
d.	

10. DISTRIBUTION STATEMENT

Approved for public release; distribution unlimited.

11. SUPPLEMENTARY NOTES	12. SPONSORING MILITARY ACTIVITY
Details of illustrations in this document may be better studied on microfiche	Air Force Materials Laboratory Air Force Systems Command Wright-Patterson AFB, Ohio 45433

13. ABSTRACT

The analytical model for the erosion of a brittle material by multiple particle impacts [1] is revised in accordance with microscopic observations of the erosion damage due to the direct impact of glass beads. Procedures are described for obtaining the quantitative data required to make the model a predictive tool. Erosion tests were conducted in the AFML-Bell erosion facility using 70 and 290 micron diameter glass beads and uniformly graded quartz sand impacting flat-faced specimens of borosilicate glass directly and at an oblique angle. Excellent agreement was found between the average ring fracture diameter and the diameter of the contact area predicted by the Hertzian theory of impact for the glass bead impacts. The damage mechanisms for glass plates impacted by sand particles and liquid drops were investigated through microscopic examination of the progressively-eroded surfaces.

Weight-loss data are available for ultra-high molecular weight polyethylene, nickel-coated glass-fiber reinforced epoxy, and graphite-fiber reinforced epoxy specimens exposed to rain and sand erosion environments. The polyethylene exposed to a rain environment eroded in a preferential manner as hypothesized in the analytical model being developed for glass plates based on the concept of pit nucleation and growth. Cutting wear was the primary erosion mechanism for sand erosion of the UHMW polyethylene. Nickel-coated composite specimens with 3 and 6 mil coatings exposed to the sand erosion environment and the 3 mil coating in the rain environment exhibited buckling of the coating. Microscopic examination of these specimens did not provide buckling of the coatings. The erosion mechanisms associated with the intermediate to long time rain and sand erosion of the graphite-fiber reinforced epoxy specimens have been identified. A micromechanical model for material removal due to liquid droplet impacts is proposed using simple beam theory. The critical material parameters in this case are values of the mode I fracture toughness evaluated for an initial crack lying parallel and transverse to the graphite fibers. Examination of the graphite-fiber reinforced epoxy specimens exposed to a sand environment reveals that both cutting and direct deformation erosion are equally effective in removing fragments of material from the surface which at most contain a few short segments of fiber and the surrounding matrix.

DD FORM 1473 (1 NOV 65)

14 WORDS	LINK A		LINK B		LINK C	
	ROLE	WT	ROLE	WT	ROLE	WT
Analytical Modeling						
Solid Particle Erosion						
Liquid Particle Erosion						
Glass						
Graphite Fiber Composites						
Nickel Coatings						

ABSTRACT

The analytical model for the erosion of a brittle material by multiple particle impacts[1] is revised in accordance with microscopic observations of the erosion damage due to the direct impact of glass beads. Procedures are described for obtaining the quantitative data required to make the model a predictive tool. Erosion tests were conducted in the AFML-Bell erosion facility using 70 and 290 micron diameter glass beads and uniformly-graded quartz sand impacting flat-faced specimens of borosilicate glass directly and at an oblique angle. Excellent agreement was found between the average ring fracture diameter and the diameter of the contact area predicted by the Hertzian theory of impact for the glass bead impacts. The damage mechanisms for glass plates impacted by sand particles and liquid drops were investigated through microscopic examination of the progressively-eroded surfaces.

Weight-loss data are available for ultra-high molecular weight polyethylene, nickel-coated glass-fiber reinforced epoxy, and graphite-fiber reinforced epoxy specimens exposed to rain and sand erosion environments. The polyethylene exposed to a rain environment eroded in a preferential manner as hypothesized in the analytical model being developed for glass plates based on the concept of pit nucleation and growth. Cutting wear was the primary erosion mechanism for sand erosion of the UHMW polyethylene. Nickel-coated composite specimens with 3 and 6 mil coatings exposed to the sand erosion environment and the 3 mil coating in the rain environment exhibited buckling of the coating. Microscopic examination of these specimens did not provide insight into the critical conditions required to produce buckling of the coatings. The erosion mechanisms associated with the intermediate to long time rain and sand erosion of the graphite-fiber reinforced epoxy specimens have been identified. A micromechanical model

for material removal due to liquid droplet impacts is proposed using simple beam theory. The critical material parameters in this case are values of the mode I fracture toughness evaluated for an initial crack lying parallel and transverse to the graphite fibers. Examination of the graphite-fiber reinforced epoxy specimens exposed to a sand environment reveals that both cutting and direct deformation erosion are equally effective in removing fragments of material from the surface which at most contain a few short segments of fiber and the surrounding matrix.

CONTENTS

LIST OF ILLUSTRATIONS

LIST OF ILLUSTRATIONS

LIST OF ILLUSTRATIONS

LIST OF ILLUSTRATIONS

LIST OF ILLUSTRATIONS

LIST OF ILLUSTRATIONS

LIST OF TABLES

1.0 INTRODUCTION

The initiation stage of the general erosion process for brittle and semibrittle materials can be idealized and described in qualitative terms as follows. Particles impact a solid material surface. The bulk material has a certain microstructure and a certain flaw distribution. The form of the microstructure may be the grains in a polycrystalline solid, crystalline phases in a semicrystalline polymer, or a disperse phase in a composite such as the fibers in a fiber-reinforced composite. The flaw distribution may be precipitates in ductile metals, microscopic surface cracks in inorganic glasses, or delaminated regions at the fiber/matrix interface in composites. The localized loadings are not sustained but generate stress pulses which propagate through the material. These stress pulses can induce minute flaws in the material if they are not already present through interactions with the microstructural features of the material, or they can extend existing flaws to a point where they become unstable. This process continues as a random function of time until localized flaw distributions reach a critical stage whereby pieces of material are freed from the surface. The efficiency with which material removal is initiated will depend on the magnitude, duration, and frequency of the localized loadings and the material's response to these loadings.

In order to understand the erosion process in these terms and to obtain analytical evaluations for the erosion of specific materials, three major areas of investigation must be considered:

●Characterization of the localized, time-dependent pressure distribution applied to a material surface by an impacting particle.

- Characterization of the transient stress distribution within the body due to the impacting particles; propagation of stress and shock waves.

- Characterization of the dynamic fracture behavior of materials based on the interaction of propagating stress waves with the material's microstructure and distributed defects.

The complex conditions described here are only an indication of the overall problem. The objective in our modeling studies has been to find justification for reasonable simplifications in the general analyses required. Evidence has already been provided for inorganic glass plates impacted by spherical glass beads that certain results from the Hertzian (quasi-static) theory of impact are applicable to a problem which involves highly transient stress distributions. In the area of fracture mechanics we are attempting to delimit those conditions under which the statically determined fracture data can be applied to dynamic fracture problems. Results of this type provide a rational basis for expecting correlations between erosion behavior and the mechanical properties of particular materials which are determined from micromechanical analyses based on microscopic examination of the erosion damage at various stages of the overall erosion process. Failure to examine the erosion process at the level we are suggesting has resulted in the general sparcity of correlations between erosion and mechanical behavior as exemplified by the negative results of numerous investigators. While the research reported here has not completely solved this problem, considerable headway has been made in understanding and analyzing the erosion behavior of moderately complex material systems.

2.0 SUMMARY

A portion of the research reported here is a continuation of research described by Adler and Sha.[1] The microscopic observations of 70 and 290 micron glass beads impacting glass plates have provided a complete picture of the erosion process for the entire range of particle sizes which are of interest in dust, sand, and ice particle erosion at subsonic velocities.

The general formulation of an analytical model describing the erosion of brittle materials[1] has been made more explicit in accordance with the experimental findings pertaining to the erosion of glass plates. The present research establishes experimental and analytical procedures for the attainment of quantitative data to specify the functions required in the revised equations governing the erosion process. The results of the erosion tests using borosilicate glass plates (Corning Glass Works designation Pyrex 7740) for the erosion targets indicated that the diameters of the ring fractures produced on the specimen surfaces by both the 70 and 290 micron glass beads impacting over a velocity range of from 200 to 450 fps were in excellent agreement with the diameters of the maximum contact areas calculated from the Hertzian theory of impact. This fact implies that the transient nature of the bead impacts is of secondary importance in the specification of the information required to describe the general erosion process.

The weight-loss data obtained for oblique impacts by spherical glass beads at the same normal velocity used in the case of direct impacts on glass plates indicate that under nearly equivalent conditions the magnitude of the weight loss at the same exposure time for oblique impacts was two to three times greater than the corresponding value for direct impacts. The ring fracture diameters were found to be approximately

equal for both impact conditions, however the penetration
depths of the cone fractures were noticeably less for the
oblique impacts especially as the impact velocity increased.
It is concluded, for a reason yet to be discovered, that the
probability for producing ring fractures for the oblique
impacts was considerably higher than for direct impacts.

Exploratory investigations for the direct and oblique
impact of quartz sand particles on glass plates were initiated.
For both impact conditions the normal component of the par-
ticle impact velocity was held constant. It was found that
the steady-state erosion rates were nearly identical. The
slightly greater values obtained for oblique impacts may be
due to the fact that the specimen receives approximately 30
percent more particle impacts per revolution in this case.
Microscopic examination of the damage occurring during the
early stages of the erosion process did not reveal any signi-
ficant differences between the direct and oblique impacts.
As would be expected the erosion rates for the irregularly-
shaped particles are considerably higher than those for glass
beads of an equivalent dimension. The basic requirements for
characterizing the particle shapes in a distribution of
irregularly-shaped particles are described in conjunction with
the extension of the analytical model to erosion of brittle
materials by sand particles.

The initial damage observed on the flat surface of a
glass specimen arising from liquid droplet impacts is due
primarily to the transient pressure distribution locally
applied to the surface. Plane glass surfaces offer the advan-
tage of an inherently simple mechanical response to the
applied loadings which closely approximates that considered
in most of the mathematical analyses of stress wave propaga-
tion in an elastic half-space. A procedure is outlined for
estimating the magnitude of the time- and spatially-dependent
pressure pulse applied to a deformable surface during the
initial stages of a spherical liquid drop striking a material

-4-

surface at low to moderate velocities. The interaction between the deforming solid surface and the liquid drop is taken into account and the transient stress distribution within the solid target can be evaluated. The erosion tests on glass plates provided insights into the fracture patterns which developed due to droplet impacts at 300 to 500 fps. Direct correlations with the numerical evaluation of the transient stress distributions which could be made on the basis of the above analysis are not available, since the acquisition of this information requires fairly extensive computer programming which will be initiated in the future. The erosion tests established that material removal in a rain environment was a preferential process of pit nucleation and growth, however weight-loss data are not available due to cracking of the specimens which occurred before a sufficient number of data points could be obtained. This experimental observation and the transient stress wave analysis described above provide a basis for extending the analytical model developed for solid particle impacts to liquid drop impacts.

Weight-loss data are available for ultra-high molecular weight (UHMW) polyethylene, nickel-coated glass-fiber epoxy, and graphite-fiber reinforced epoxy specimens exposed to rain and sand erosion environments. A number of specimens eroded to various stages of the overall erosion process are also available for direct microscopic identification of the operative erosion mechanisms supplementing the microscopic investigations which were conducted while the specimens were being incrementally eroded in the AFML-Bell rotating-arm facility.

The rain erosion characteristics of UHMW polyethylene exhibited a strong tendency toward a process of pit nucleation and growth. Over a velocity range of from 500 to 1120 fps the time scale for which a particular erosion mechanism is operative in these specimens is only contracted or expanded as the impact velocity is increased or decreased but no change

is evident in the sequence of operative erosion mechanisms.
Material removal from aerodynamically-shaped specimens by
sand particles is due to the cutting action of the particles:
more material is removed at locations on th specimen's sur-
face away from the leading edge than at the leading edge.
A steady-state erosion rate is quickly established in this
case.

The nickel-coated composites exposed to a rain environ-
ment developed a dense array of cracks in the coating which
rarely penetrated the full thickness of the coating. The
influence of the coating thickness on erosion behavior was
investigated. A specimen with a 3 mil coating failed by
localized buckling of the coating followed by catastrophic
failure of the entire buckled area. At this time a few ero-
sion pits could be found on the surface which almost penetra-
ted the coating thickness. A specimen with a 6 mil coating
did not exhibit the buckling instability, but rather the
coating was completely eroded in a localized region on the
leading edge of the specimen at an exposure time which was
seven times longer than that at which buckling occurred for
the 3 mil coating. No measurable weight loss was observed in
either case. Specimens with both the 3 and 6 mil nickel coat-
ings were exposed to a sand environment at 730 fps. Both
coating thicknesses failed by buckling of the coatings which
extended over approximately one-half the length of the speci-
men. Measurable weight losses were recorded in both cases.
The rate of material removal was constant after a short incu-
bation period and essentially identical for both specimens.
The 6 mil coating lasted three times longer than the 3 mil
coating in the sand environment, and the specimen with the
6 mil coating had a weight loss approximately three times
the weight loss for the 3 mil coating at the time of failure.
Microscopic examination of the nickel-coated composite speci-
mens did not provide insight into the critical conditions
required to produce buckling of the coating.

The erosion mechanisms associated with the intermediate
to long time rain and sand erosion of the graphite-fiber
reinforced epoxy specimens have been identified. For a rain
environment a micromechanical model is presented for material
removal based on simple beam theory. According to this model
the important material characteristics involved in the erosion
behavior of the composite are its mode I fracture toughness
values evaluated under dynamic conditions for an initial crack
parallel to the fiber reinforcement and transverse to the
fiber reinforcement. The sand erosion of the graphite-fiber
reinforced epoxy specimens occurs through fine-scale cracking
of both the fiber and matrix. The eroded fragments would con-
tain at most a few short segments of the fibers and the sur-
rounding matrix. A steady-state erosion rate is quickly
established at an impact velocity of 730 fps after a very short
incubation period. On the basis of the uniformity of the
eroded surface of the aerodynamically-shaped specimens, direct
deformation and wear deformation are equally effective in
removing material from the surface of this composite.

3.0 EROSION OF GLASS SPECIMENS

Erosion data were obtained for borosilicate glass speci-
mens (Corning Glass Works designation Pyrex 7740) subjected
to the direct and oblique impact of 70-micron glass beads,
290-micron glass beads, and quartz sand with a mean diameter
of approximately 90 microns. The erosion tests conducted are
recorded in Table I. Due to the scope of the present program
it was only possible to run one or at most two specimens under
the same test conditions, so the findings reported here are
only indications of the general features of the erosion process.
These results are adequate however for providing guidance in
extending the solid-particle modeling studies to more general
erosion conditions.

3.1 General Considerations

Glass specimens were used in the erosion tests. The
mechanical properties of Pyrex, fused silica, and soda lime
glass are listed in Table II. Table III indicates the magni-
tude of the relevant indentation parameters based on the
Hertzian theory of impact. To slide rule accuracy the change
in the magnitude of the impact parameters is negligible for
Pyrex impacted by soda lime glass beads compared with fused
silica impacted by soda lime glass beads. Microscopic inves-
tigation of the general features of the erosion process in
each case show them to be identical.

The glass specimens were rectangular parallelepipeds:
3.25 in. x 0.875 in. x 0.5 in. In order to obtain a uniform
distribution of particle impacts on the face of the specimen
and to eliminate edge effects, thin metal plates were inserted
in the specimen holder so that only the central portion of the
specimen's surface is exposed to the particles dropping from
the nozzle at the end of the blast tube in the AFML-Bell ero-
sion facility. The specimen configurations for direct impacts

TABLE I

EROSION TEST SCHEDULE - GLASS SPECIMENS

Specimen No.	Normal Velocity (fps)	Erosive Medium	Exposure Time (sec)	Remarks
PY-1	300	rain	2400	Specimen fractured
PY-2	500		30	Specimen fractured
PY-3	500		-	Specimen fractured
PY-4	400		1200	Weight-loss data - specimen fractured
PY-5	500		750	Weight-loss data - specimen fractured
PY-10	200	290µ beads	585	Weight-loss data
PY-11	375		14	Weight-loss data
PY-12	Variable		50	Ring fracture threshold determination
PY-13	132		10	Ring fracture threshold determination
PY-14	151		10	Ring fracture probability evaluation
PY-15	170		10	Ring fracture probability evaluation
PY-16	188		10	Ring fracture probability evaluation
PY-17	208		10	Ring fracture probability evaluation
PY-18	226		10	Ring fracture probability evaluation
PY-19	246		10	Ring fracture probability evaluation
PY-20	375	70µ beads	60	Distribution of ring fracture diameters
FY-21	450		120	Distribution of ring fracture diameters
PY-22	375		780	Weight-loss data
PY-23	450		440	Weight-loss data
PY-24	375		10	Specimen fractured
PY-25	375		360	Weight-loss data - initial phase - end of specimen chipped
PY-26	375		360	Weight-loss data - initial phase
PY-27	450		240	Weight-loss data - initial phase

TABLE I (continued)

Specimen No.	Normal Velocity (fps)	Erosive Medium	Exposure Time (sec)	Remarks
PY-30	300	70μ beads - oblique	1440	Weight-loss data
PY-31	375		480	Weight-loss data
PY-32	275		150	Weight-loss data - initial phase
PY-33	375		50	Microscopic examination
PY-34	200	290μ beads - oblique	275	Weight-loss data
PY-35	300		22	Weight-loss data
PY-36	375		2	Weight-loss too high - flow rate adjusted
PY-37	200		30	Microscopic examination
PY-38	200		30	Microscopic examination
PY-39	200		90	Microscopic examination
PY-40	200	90μ sand	500	Weight-loss data
PY-41	300		135	Weight-loss data
PY-42	375		36	Weight-loss data
PY-43	200		5	Microscopic examination
PY-44	300		2	Microscopic examination
PY-45	300		7	Microscopic examination
PY-46	375		1	Microscopic examination
PY-50	200	90μ sand - oblique	190	Weight-loss data
PY-51	300		235	Weight-loss data
PY-52	375		27	Weight-loss data
PY-53	200		5	Microscopic examination
PY-54	300		2	Microscopic examination
PY-55	375		1	Microscopic examination

TABLE II

MECHANICAL PROPERTIES
OF
GLASS BEADS AND SPECIMENS

	Soda Lime Glass	Fused Silica	Pyrex
Density (lb./in.^{3})	0.0866	0.0795	0.0805
Poisson's Ratio	0.22	0.17	0.22
Young's Modulus (lb./in.^{2})	10.0×10^6	10.68×10^6	9.8×10^6

TABLE III
HERTZIAN IMPACT PARAMETERS

	Equivalent Static Load, P(lb.)	Radius of Contact Circle, a(in.)	Duration of Contact, T(sec)
70 Micron Glass Beads			
200 fps	0.215	0.350×10^{-3}	1.19×10^{-7}
300 fps	0.355	0.415×10^{-3}	1.10×10^{-7}
400 fps	0.504	0.465×10^{-3}	1.04×10^{-7}
500 fps	0.653	0.506×10^{-3}	0.99×10^{-7}
290 Micron Glass Beads			
200 fps	3.56	1.430×10^{-3}	4.76×10^{-7}
300 fps	5.88	1.692×10^{-3}	4.40×10^{-7}
400 fps	8.35	1.900×10^{-3}	4.15×10^{-7}
500 fps	10.80	2.078×10^{-3}	3.97×10^{-7}

and oblique impacts when the normal to the specimen's surface is inclined at an angle of 50° to the plane of the rotating arm are indicated in Fig. 1. For direct impacts the exposed area on the face of the specimen is 0.82 in.^{2} (1.05 in. x 0.78 in.) and for the oblique impacts it is 1.81 in.^{2} (0.59 in. x 3.07 in.).

A sieve analysis was made of the 70-micron glass beads and a quartz sand supplied by the American Graded Sand Company, Paterson, New Jersey, which was to be narrowly distributed around a mean particle size of 70 microns. The sieve sizes used are listed in Table IV, and a comparison of the size distribution for the sand and glass beads is shown in Fig. 2. It is seen that the diameters of the glass beads are quite narrowly distributed around a mean diameter of 70 microns. The mean maximum lateral dimension of the quartz sand particles is estimated to be 92 microns; the size distribution is not very narrow, but fairly smoothly spread over a 100-micron range above 63 microns. The angularity of the sand particles can be seen in Fig. 3. As a matter of convenience in writing, the quartz sand will be referred to as the 90-micron sand.

Modification of the formula derived earlier[1] for estimating the number of particles impacting the surface of the specimen is required to include the reduction in the surface area of the specimen exposed to particle impacts and the inclusion of particles striking the surface of the specimen obliquely. The final result is simply

$$N_I = \frac{N}{720\sqrt{2gh}} \; \frac{\ell}{\ell'} \; d' \cos\theta \tag{1}$$

where N_I is the number of particle impacts the specimen experiences per revolution of the rotating arm

N is the number of particles released per minute

$\sqrt{2gh}$ = 21.233 ft. for the AFML-Bell erosion facility

ℓ is the lateral dimension of the nozzle in inches

Impact velocity

Exposed area on specimen's surface

Not to scale

40°

3.07"

0.59"

1.50"

0.75"

Dimensions of nozzle for oblique impacts

Stream of particles dropping from nozzle

Impact velocity

0.18"

1.05"

1.575"

0.4575"

Dimensions of nozzle for direct impacts
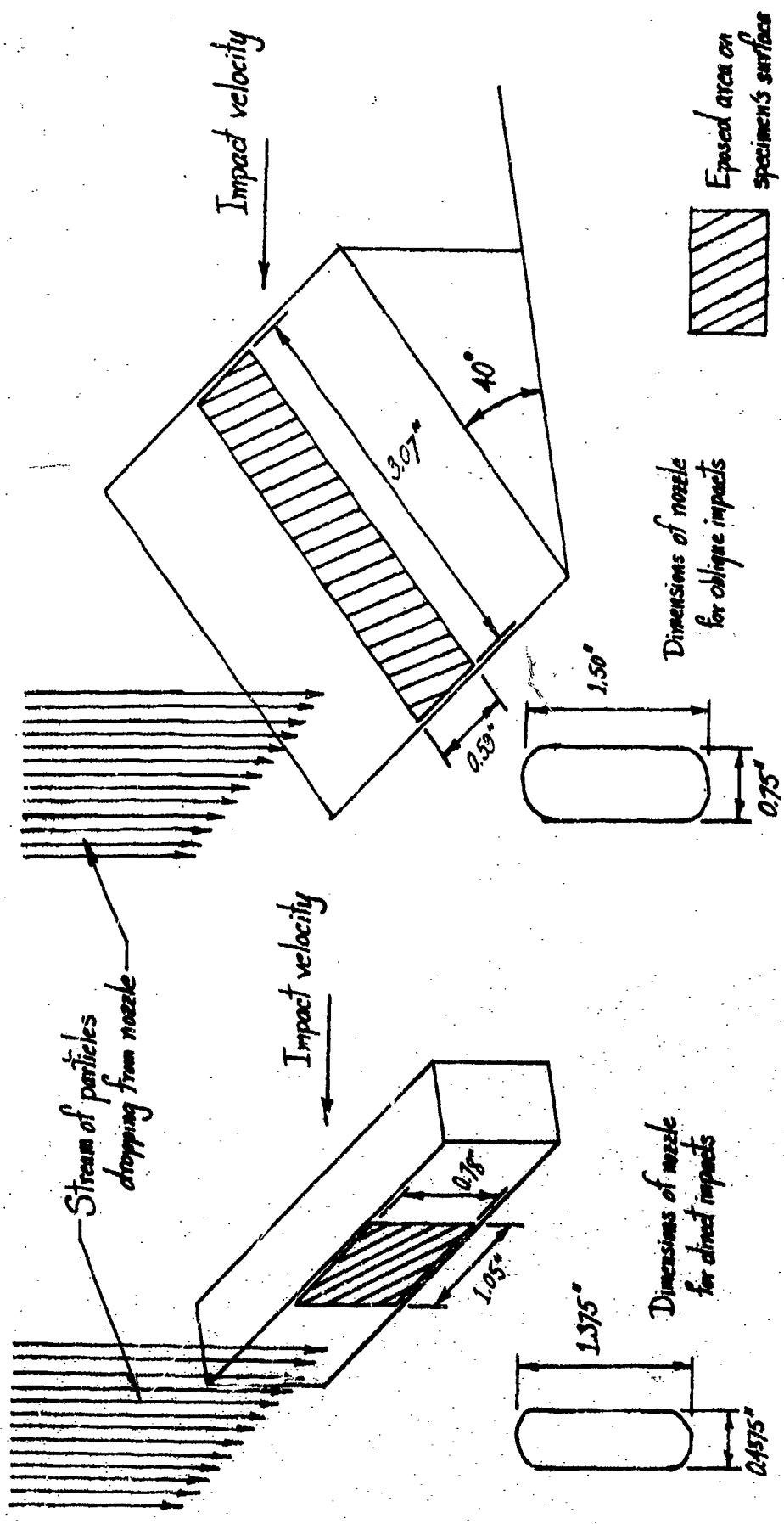
FIGURE 1   Nozzle dimensions and experimental arrangement for direct and oblique solid particle impacts.

TABLE IV

SIEVE SIZES USED IN THE DETERMINATION OF PARTICLE SIZE DISTRIBUTION FOR GLASS BEADS AND QUARTZ SAND

Sieve Number Tyler Equivalent Mesh	Mesh Opening Microns	Inches
80	177	0.0070
140	105	.0041
170	90	.0035
230	63	.0025
270	53	.0021
325	44	.0017
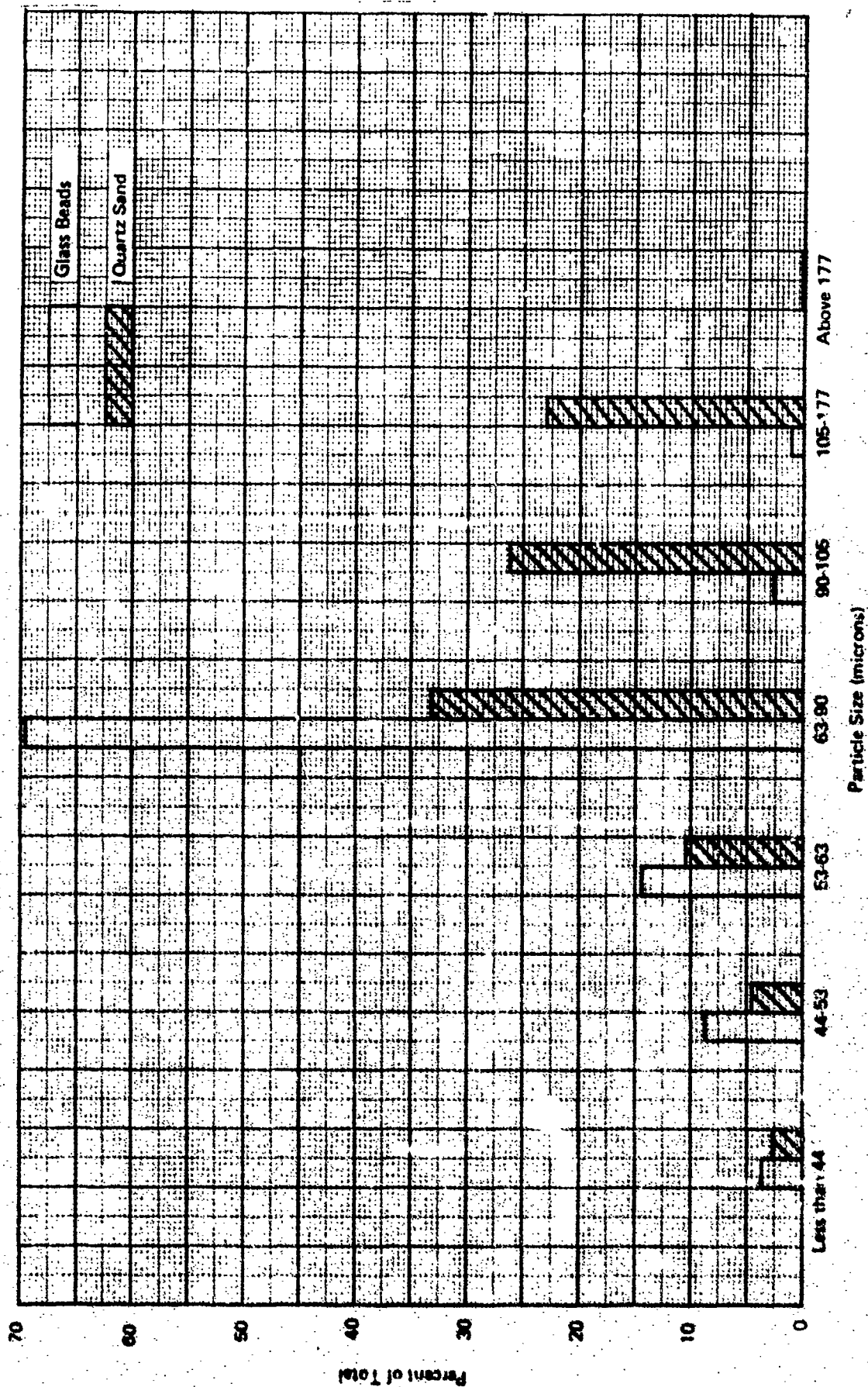
FIGURE 2   Particle size distributions for 70-micron glass beads and 90-micron sand.
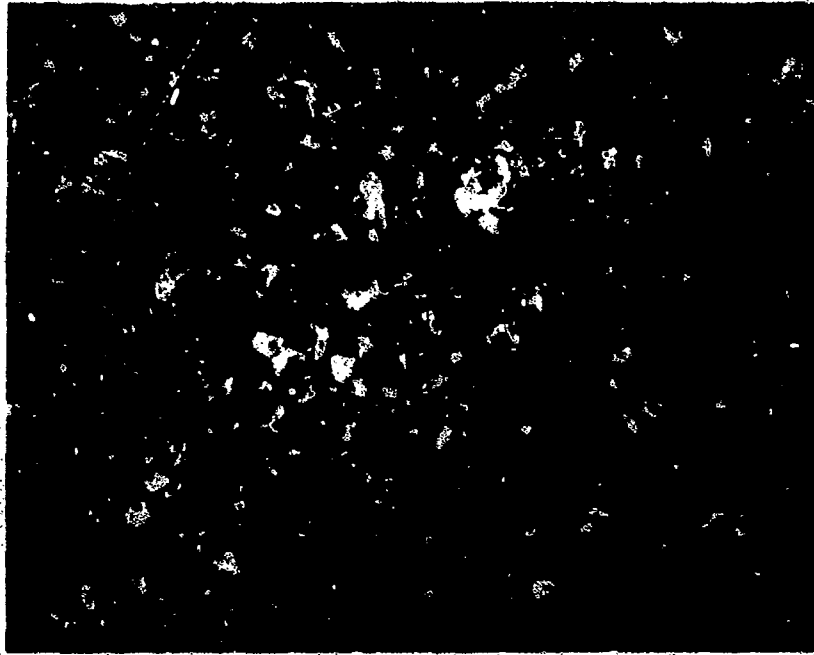
(a) Sieve size below 44 microns

(b) 44 to 75 microns

FIGURE 3. Particle characteristics for quartz sand. (80X)

- 35 -

(c) 53 to 63 microns

(d) 63 to 90 microns

FIGURE 3 Particle characteristics for quartz sand. (80v)

-36-
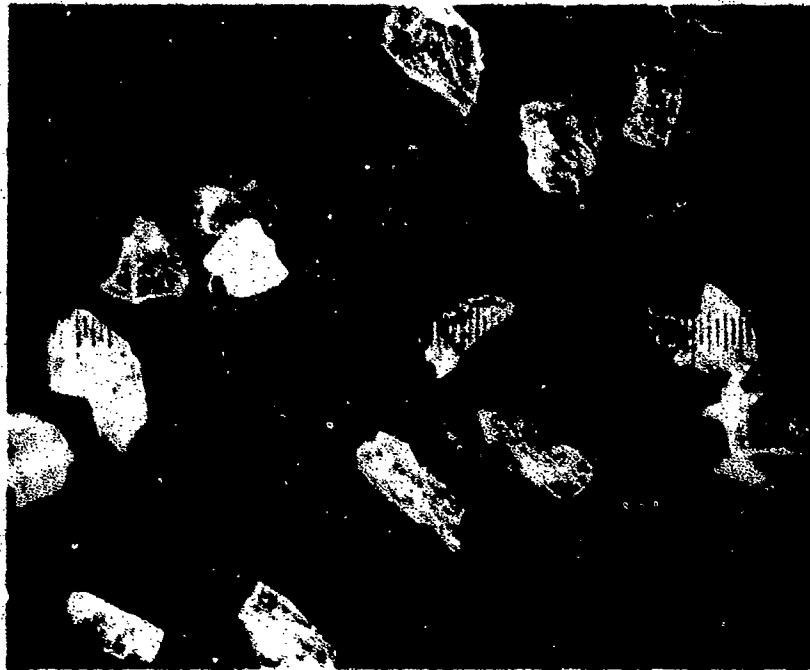
(e)   40 to 105 microns

(f)   105 to 177 microns

FIGURE 3. Particle characteristics for quartz sand. (80X)

l' is the lateral dimension of the exposed area on the specimen's surface in inches

d' is the transverse dimension of the exposed area on the specimen's surface in inches

θ is the angle of inclination between the normal to the specimen's surface and the plane of the rotating arm.

When $\theta = 90°$, $N_I = 0$ according to Eq. (1). This result is consistent with the implicit assumption that the vertical velocity of the particles is negligible with respect to the velocity of the specimen.

For the experimental arrangement illustrated in Fig. 1, when $\theta = 0°$, $l = 1.375$ in., $l' = 1.05$ in., and $d' = 0.78$ in. and when $\theta = 50°$, $l = 1.50$ in., $l' = 0.59$ in., and $d' = 3.07$ in. It has been assumed that the lateral dimension of the nozzle is representative of the equivalent uniform particle distribution across the specimen for the entire volume of particles dropping through the path of the specimen. Admittedly this approximation does not properly account for the observed lateral flaring of the particle flow as it leaves the nozzle, however the uniformity of the flow near the center of the specimen does not seem to be affected by the decrease in the particle flow density at the ends of the specimen. The results of Eq. (1) should therefore provide a reasonable estimate of the number of bead impacts per revolution for the experimental arrangement used in the erosion tests.

For the glass beads a reasonable estimate can be made for the number of impacts the specimen would experience for a given bead flow rate and velocity. Further assumptions are required to provide a similar estimate for the sand particles. The simplest approach is to assume that the sand particles are equivalent to 90-micron diameter quartz spheres and compute the number of impacts on the basis of the formula in Eq. (1). The result for this case and for the two sizes of glass beads are listed in Table V.

TABLE V

CALCULATED NUMBER OF PARTICLE IMPACTS PER REVOLUTION

Particle Description	Number of Particles per 1000g	Particle Flow Rate (g/min)	(Particles/min.)	Calculated Number of Particle Impacts/Revolution* Direct	Oblique
70-micron glass beads	2.34×10^9	950	2.22×10^9	8.6×10^4	1.12×10^5
290-micron glass beads	3.28×10^7	370	1.21×10^7	470**	615
90-micron quartz sand	1.19×10^9	260	3.10×10^8	1.2×10^4	1.57×10^4

*In the AFML-Bell erosion facility, 1 RPM = 1.06V where V is the velocity measured in feet per second at the midpoint of the specimen in the plane of the rotating arm.

**Cover plates were not used in the erosion tests for the direct impact of the 290-micron beads. Under these conditions the specimen experiences 595 impacts/revolution and the exposed surface area is 2.25 sq. in.

3.2 Direct Impact by Glass Beads

The direct impact of spherical glass beads on glass plates provides idealized conditions for a combined analytical and experimental study of the erosion process and its relation to the mechanical behavior of the colliding bodies and impact parameters. The mechanical properties of the target material and impacting particles are those of a brittle elastic solid. The simplified geometry of the impacting particles allows the introduction of concepts and results from the Hertzian theory of impact. The relations required from the Hertzian theory are discussed by Adler and Sha[1]. Additional experimental and analytical results which are essential to the development of the analytical model proposed by Adler and Sha[1] will be described.

3.2.1 Description of Erosion Process

The erosion mechanisms operative on flat surfaces of Pyrex and fused silica glass specimens impacted by 70 and 290 micron glass beads have been established through detailed microscopic investigation of a number of progressively eroded surfaces. The following patterns emerge.

The basic element for the initiation of erosion damage in glass specimens is the ring fracture[1]. The diameter of the ring and the geometry of the conical fracture surface extending into the bulk of glass plates impacted by glass beads is dependent on the radius and impact velocity of the glass beads as well as the material properties of the colliding bodies. For the range of conditions used in this program the conical fracture surfaces are typically 5 to 20 microns deep and on the order of 1 mil in diameter at the surface of the glass plate for the 70 micron beads. The 290 micron beads produce fracture surfaces which are 50 to 90 microns deep and approximately 3 mils in diameter at the surface of the glass plate.

Subsequent impacts in the vicinity of the shallow fracture frustrums produced by the 70 micron beads initiate chipping of material from the surface on a very fine scale. Microscopic observations of the time evolution of the eroded surface indicate that once a ring fracture occurs it is the nucleation site for the removal of material. The series of micrographs in Fig. 4 and 5 show the change in the surface of the specimen before a measurable weight loss is recorded. The micrographs were taken in bright field, so the black spots on the white field represent the material that has been removed from the surface. The details of the eroded surface are not visible, but the extent of the area removed is quite distinct. The eroded areas grow preferentially around a ring fracture by fine-scale chipping of material due to intersecting ring fractures. This process continues to remove material from the surface layer and expose a highly-fractured and irregular subsurface from which material is removed by chipping of small pieces with each impact.

In the case of the 290 micron beads another impact in the vicinity of a deep conical fracture surface is generally not sufficient to cause material removal but contributes instead to a more severely fractured subsurface. Additional impacts in this region produce a predictable pattern of subsurface fractures at depths which still allow a substantial layer of overlying material to remain intact. It is only after a number of impacts have occurred in the vicinity of the initial ring fracture that removal of the material exterior to the developing distribution of conical frustrums takes place. The material contained within the frustrums formed by the conical fracture surfaces is more resistant to erosive attack than the highly fractured interstitial regions, therefore material removal from the interstitial volumes takes place at a higher rate than during the ring fracture development phase. The interstitial material is removed leaving a dense distribution of solid frustrums protruding from the bulk
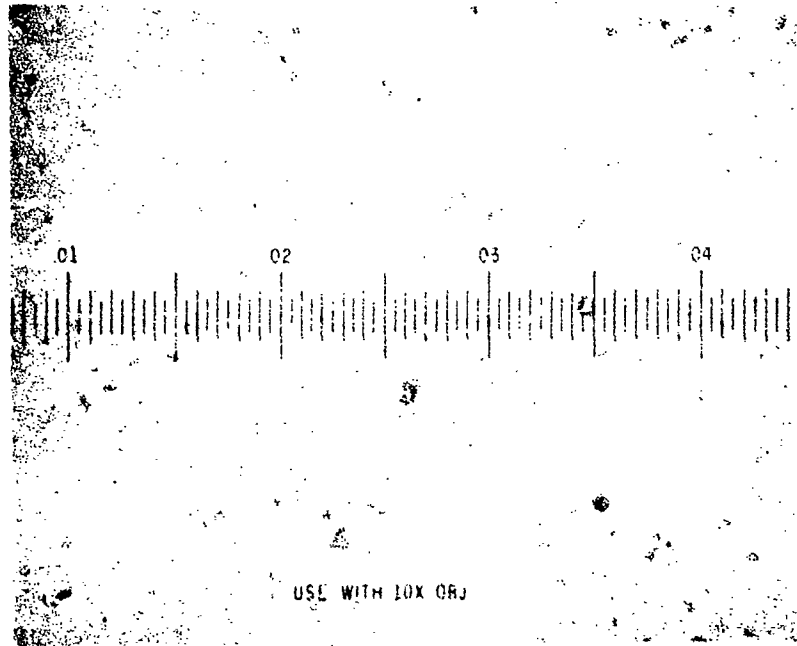
(a) 1 minute exposure
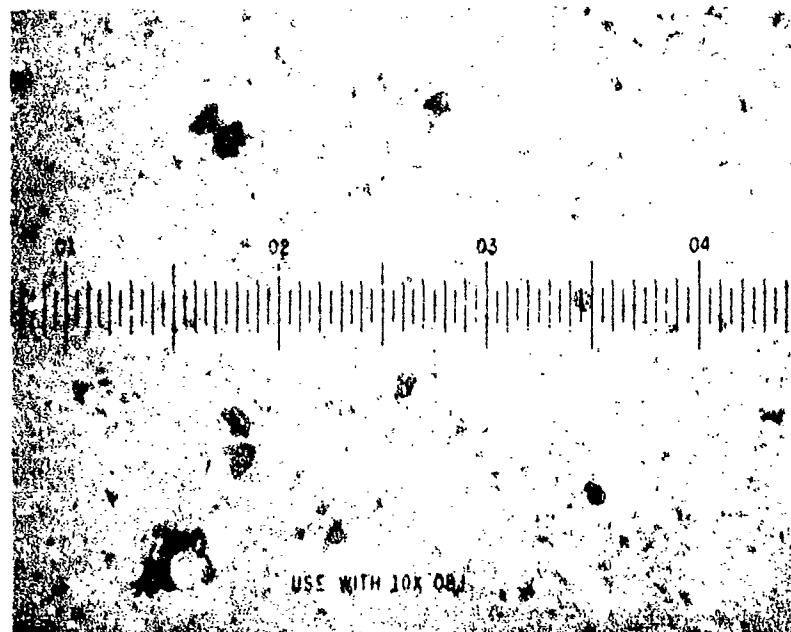
(b) 2 minute exposure

Figure 4   Progressive Erosion of a Glass Plate by 70-Micron Beads at
375 fps 110X (Sheet 1 of 2)
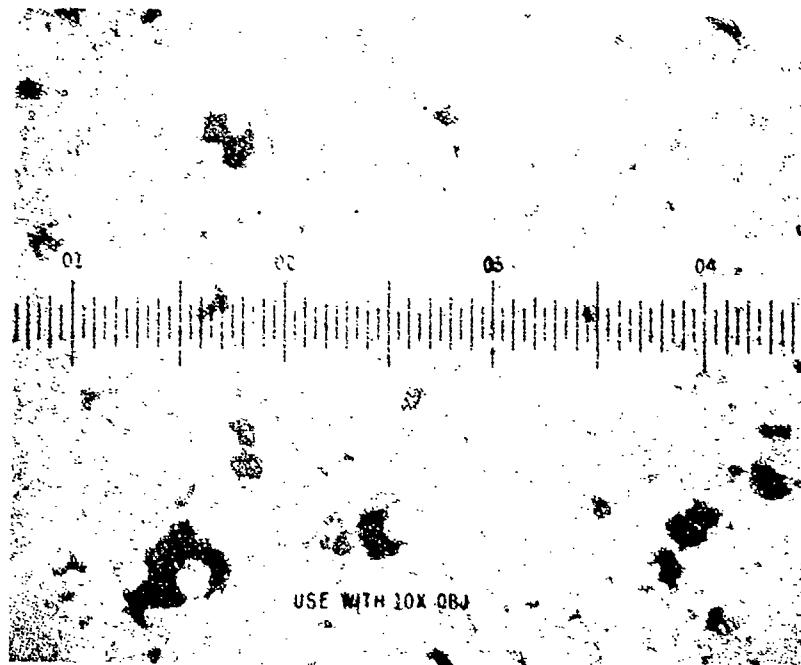
(c) 3 minute exposure
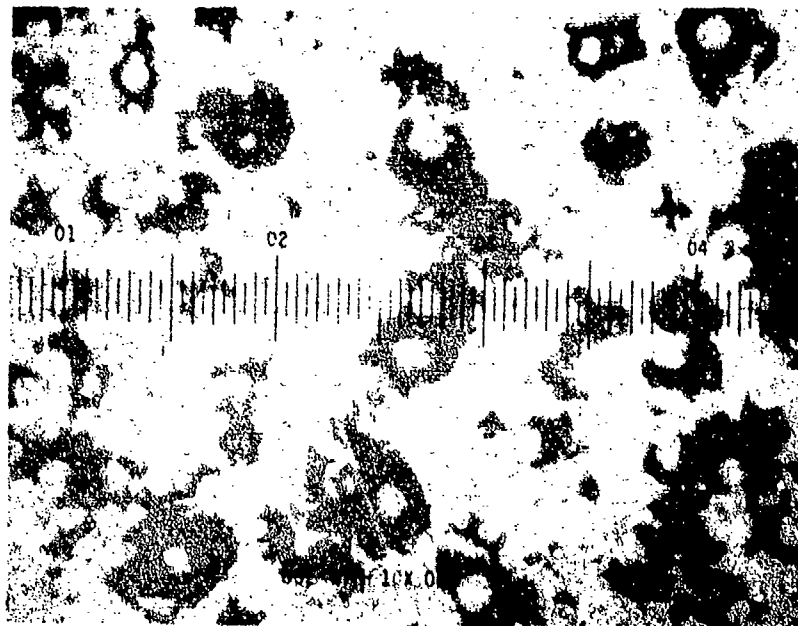
(d) 4 minute exposure

Figure 4 Progressive Erosion of a Glass Plate by 70-Micron Beads at
375 fps 110X (Sheet 2 of 2)
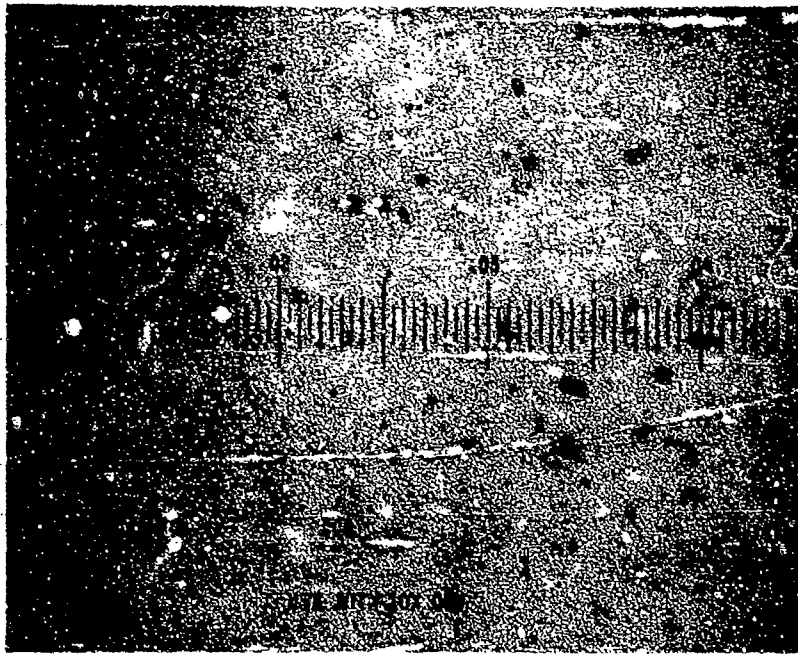
(a)   1 minute exposure
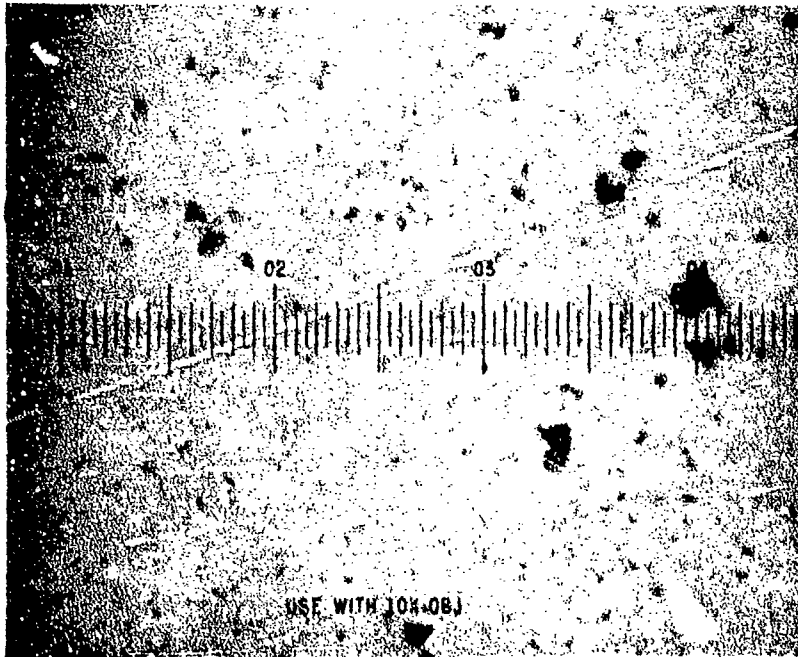
(b)   2 minute exposure

Figure 5   Erosion of pyrex by 70 micron beads
at 375 fps (Area 3)   110X
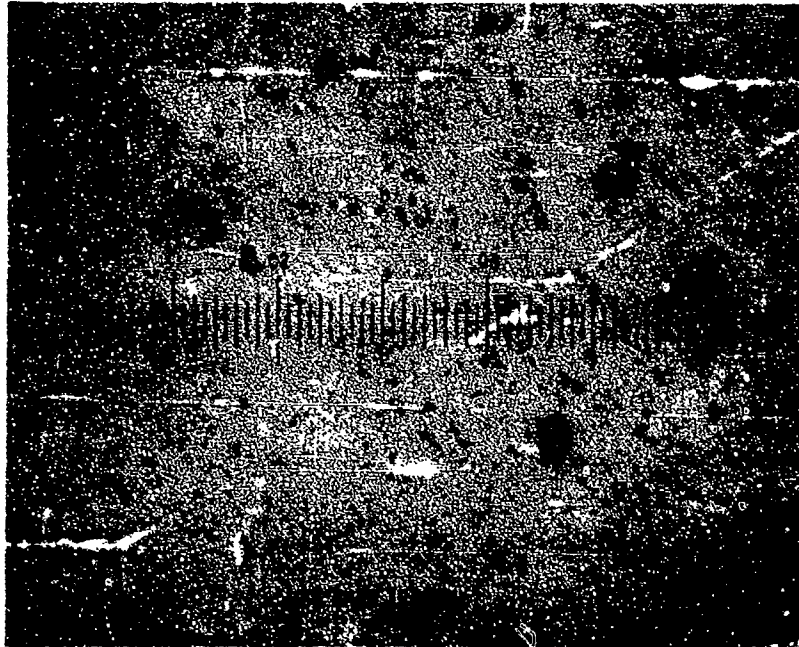
(c) 3 minute exposure
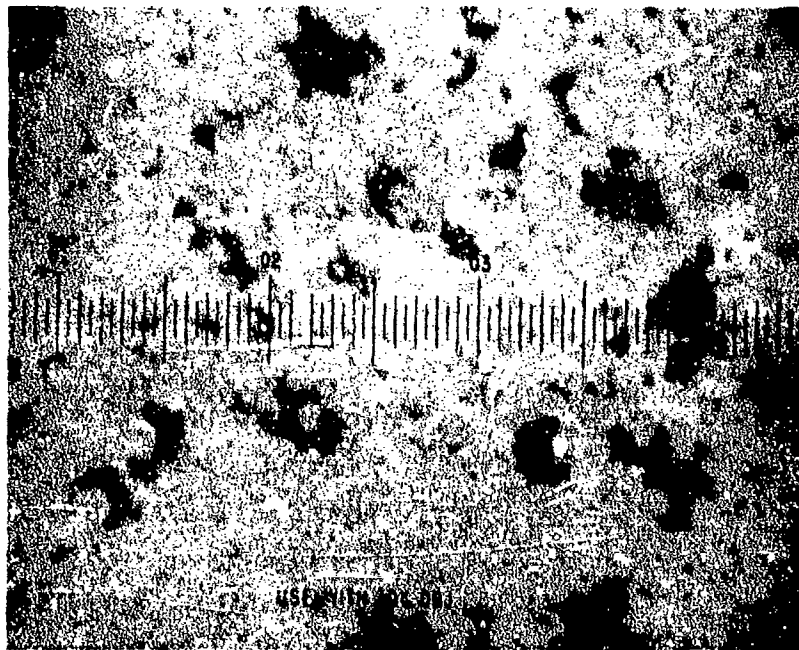
(d) 4 minute exposure

Figure 5 Erosion of pyrex by 70 micron beads at
375 fps (Area 3) 110 X

specimen. The various stages in the material removal process are shown in Fig. 6. The impacting beads chip small pieces of material from these frustrums at a slower rate than in the interstitial material removal stage. As the frustrums erode, more surface area is susceptible to bead impacts. Chipping of the highly-fractured and irregular surface of the bulk material takes place at a uniform rate and constitutes the final phase of the erosion process.

The microscopic observations of the erosion process associated with the two bead sizes used in the erosion tests indicate that the depth of the cone fracture surface determines whether a single impact in the vicinity of a pre-existing ring fracture will result in material removal or a number of impacts are required before material removal is therefore dependent on the radius and velocity of the impacting glass beads, however the general erosion process remains unchanged over the range of bead sizes and impact velocities used in this research.

The mechanisms for material removal described above are summarized as follows:

(1) material removal during ring fracture formation,

(2) material removal during the growth of nucleated erosion pits,

(3) material removal due to chipping of the conical frustrums resulting from the fracture process in glass plates,

(4) material removal due to chipping of the bulk material.

Now that these mechanisms have been identified, this information will be included in the mathematical formulation of the basic erosion model.[1]
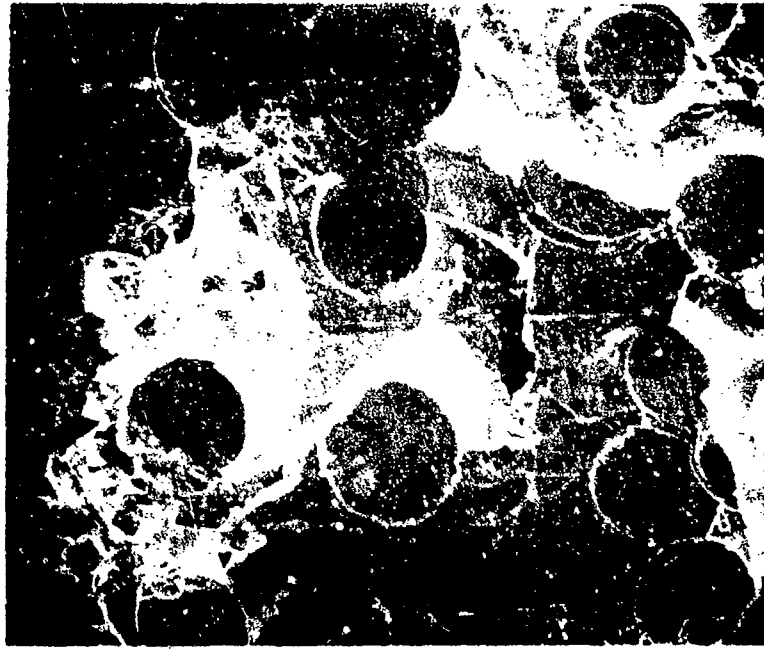
(a) 230X
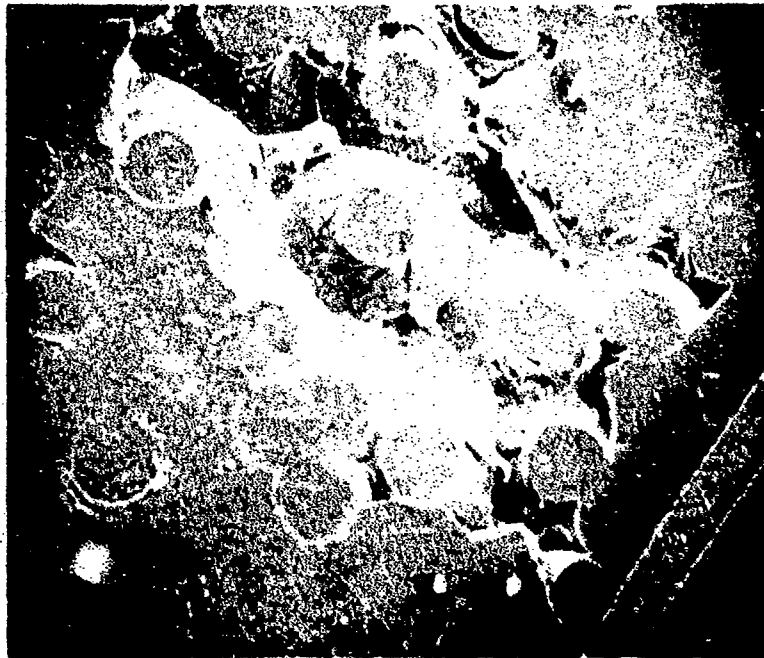
(b) 110X

Figure 6   Progression of erosion damage on the surface
of a glass plate due to impacts by 290-
micron glass beads

(c) 116X
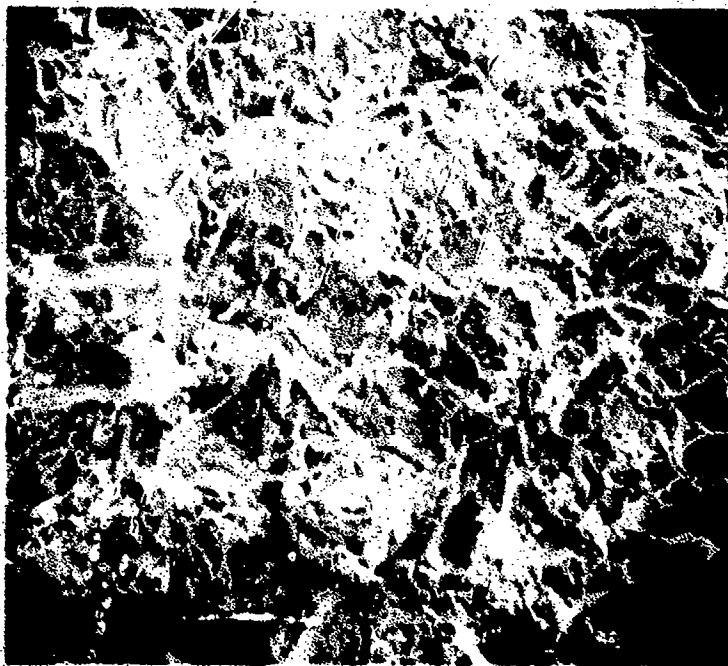
(d) 116X

Figure 6 Progression of erosion damage on the surface of a glass plate due to impacts by 290-micron glass beads.

3.2.2 Analytical Model for Solid Particle Impacts

The general erosion process can be divided into three phases. The total volume of material removed is

$$\Delta V(t) = \Delta V_1(t) + \Delta V_2(t) + \Delta V_3(t) \tag{2}$$

where $\Delta V_1(t)$ is the volume of material removed at the time t due to the formation and growth of erosion pits on the surface of the specimen

$\Delta V_2(t)$ is the volume of material removed due to chipping of the conical frustrums

$\Delta V_3(t)$ is the volume of material removed due to chipping of the bulk material

In terms of the previous model,[1] the general erosion process can be described by dividing the specimen into two platelets: a surface layer defined by the mean depth of penetration, D, of the conical fracture surfaces and the remainder of the bulk material. The volume V_1 of the surface layer is now composed of two components,

$$V_1 = AD = \lim_{t \to \infty} \left(\Delta V_1(t) + \Delta V_2(t) \right) \tag{3}$$

where A is the area of the specimen exposed to the erosive environment.

$$\Delta V_1(t) = \eta D \Delta A_1(t) \tag{4}$$

where η is a shape factor which will be described below and $\Delta A_1(t)$ is the area removed at time t from the free surface of the first platelet. With $\Delta V_1(t)$ defined, the evaluation of $\Delta A_1(t)$ is of major concern.

The number of ring fractures formed on a unit area of the specimen at any time t is

$$N(t) = \int_0^t \left(1 - \Delta A_1(\tau) - N(\tau)A_o\right) n\varphi(\tau) d\tau \qquad (5)$$

where $\Delta A_1(\tau)$ is the area removed from a unit area of the sur-
face layer at any time $\tau = t$ due to the impacting
particles

A_o is the area of a ring fracture

n is the number of impacts/unit area-time

$\varphi(\tau)$ is a time-dependent probability that a ring
fracture will occur.

The variables are now expressed in terms of a unit of surface
area. Corresponding adjustments should be made in Eq. (2) to
(4).

The surface area of the specimen exposed to
the erosive environment changes with the exposure time, and
the material removal due to the growth of pits once they are
formed must be subtracted from the total area available for
producing new ring fractures. Although overlapping ring frac-
tures do occur, it is assumed here that once a ring fracture
is formed there is no possibility for another ring to be
formed in the same area. This is a valid assumption for the
shallow fracture surfaces where an impact in the vicinity of
a pre-existing ring is more likely to contribute to the growth
of an erosion pit than the formation of a new ring fracture.
It is for this reason that the total effective area of the
ring fractures present at any instant is also excluded from
the surface area available for the formation of ring fractures.

Referring to Fig. 4 and 5 it can be seen that
very few ring fractures are produced during the earliest stage
of the erosion process. There is abundant evidence that
numerous particles have struck the surface by the distribu-
tion of very small nicks in the surface, however, these flaws
exhibit relatively minor growth during subsequent exposure
to the particle impacts. The ring fracture population begins

to increase after an incubation period. It is conjectured that ring fractures are being produced on the surface due to multiple impacts at velocities which are substantially below those which would be required to produce a ring fracture due to a single particle impact. The reasoning is as follows. The original surface has an initial flaw distribution, but as the particles collide with the surface a more extensive flaw distribution evolves. The probability that a ring fracture will result is increased with increasing exposure time. This effect can be seen most clearly in Fig. 5 where a negligible number of ring fractures are observed on the surface of the specimen after an exposure time of one minute. During the next one minute increment in the exposure time numerous ring fractures are formed. Research on the evaluation of the probability for ring fracture formation on glass plates due to solid particle impacts has concentrated on single particle collisions over a range of particle sizes which is above that usually of interest in erosion studies. In order to account for the observed time-dependent probability function in multiple particle collisions, it is necessary to devise an adjunct experimental program to obtain the data required. Consideration is being given to static and dynamic indentation tests using particle sizes corresponding to those used in the erosion tests and glass specimens which have been exposed to multiple particle impacts for a range of exposure times which are less than those at which ring fractures are first observed. It is known[2] that the threshold fracture stress in dynamic tests is higher than that found in static tests, however the attainment of the velocities required for single impacts of glass beads less than 300 microns in diameter would involve a much more extensive experimental facility than the static tests.

Let φ_o be the probability that a ring fracture will be produced under conditions corresponding to those for a lightly eroded surface. The time lag in the formation of ring fractures on the surface of the glass specimens can be represented by

$$\varphi(t) = \varphi_0 \left(\frac{t}{1+m_1 t} \right)^{m_2} \tag{6}$$

with the values of the parameters m_1 and m_2 being obtained from microscopic observations on ring fractures. General trends in $\varphi(t)$ for different size beads and impact velocities can be noted in order to establish relationships between m_1, m_2 and the variables which are to be specified in the model.

As material begins to be removed from the surface layer, an increasing number of impacting beads contribute to the growth of the nucleated erosion pits and cannot be considered to be available for ring fracture production. In order to take this effect into account in the modeling studies, the form of the time-dependent ring fracture probability function in Eq. (6) can be modified so that after reaching a maximum it approaches zero as the exposure time increases. It is preferable to modify φ and let the number of impacting particles remain constant, instead of trying to devise a method for deciding on the number of beads contributing to ring fracture formation and the number contributing to the growth of erosion pits as a function of time.

The formation of erosion pits is a function of the ring fractures formed on the surface of the specimen. Guided by the microscopic investigations of multiple particle impacts,

$$N_u = g(D)N(t) \tag{7}$$

where $N_u(t)$ is the number of erosion pits nucleated at time t per unit surface area

$g(D)$ is a function of the thickness of the surface layer which is determined by the penetration of the fracture surface into the bulk of the specimen and is dependent on the radius and velocity of the impacting glass beads.

-34-

For the very small glass beads, $g(D)$ can be equated to unity. Each ring fracture is essentially a nucleation site for an erosion pit as can be seen in Fig. 4 and 5.

The area removed from the surface of the specimen through the growth of erosion pits is specified by

$$\Delta A_1(t) = \int_0^t \frac{dN_u(\tau)}{d\tau} K_1(t-\tau)d\tau \tag{8}$$

which simply is the summation of the number of erosion pits nucleated in the time interval τ, $\tau+d\tau$ times the growth rate, K_1, they experienced from the time they were formed to the current time t.

Combining Eq. (5), (7), and (8),

$$\frac{N(t)}{n} = \int_0^t \varphi(\tau)d\tau - g(D)\int_0^t \varphi(\tau)\int_0^t \frac{dN(\theta)}{d\theta} K_1(\tau-\theta)d\theta d\tau - A_0\int_0^t N(\tau)\varphi(\tau)d\tau \tag{9}$$

The erosion of the surface layer can be evaluated by solving this single integral equation for $N(t)$. The erosion tests and adjunct experimental programs are being used in conjunction with the Hertzian analysis of solid particle impacts to supply explicit representation for the functions $\varphi(t)$, $K_1(t)$, $g(D)$, and A_0.

A limiting case of Eq. (9) can be considered to substantiate its validity. For very small beads at a sufficiently high impact velocity the probability for ring fracture formation approaches unity and $g(D)$ should also be unity, then Eq. (9) reduces to

$$\frac{N(t)}{n} = \int_0^t d\tau - \int_0^t \int_0^t \frac{dN(\theta)}{d\theta} K_1(\tau-\theta) d\theta d\tau - A_0 \int_0^t N(\tau)d\tau \tag{10}$$

To further simplify this equation, assume $K_1(t) = 0$ for $0 \leq t \leq \infty$, which means $\Delta A_1(t) = 0$, then

$$\frac{dN}{dt} + nA_0N = n$$

$$N(t) = \frac{1}{A_0}(1-e^{-nA_0t}) \tag{11}$$

The maximum number of ring fractures which can be found on a unit area of the surface of the first platelet is given by

$$N_{max} = \frac{1}{A_0} \tag{12}$$

where A_0 is the area of a single ring fracture. It is seen that this is a reasonable result in view of the assumptions made. The form of Eq. (11) also shows that the number of ring fractures increases as a function of time when the number of impacts on the surface is increased.

Once $\Delta A_1(t)$ is determined from Eq. (8), it can be substituted into Eq. (4) to obtain the volume eroded from the first platelet. It was stated earlier that the eroded volume from the first platelet was composed of two components: ΔV_1 and ΔV_2. As ΔV_1 increases with time, a distribution of conical frustrums are exposed on the eroded surface. This phenomenon is particularly evident for the 290 micron beads as shown in Fig. 6(b). The frustrum density after removal of the interstitial material reaches a fairly saturated state before the frustrums are eroded further. The distribution of frustrums on the specimen surface constitute the portion of the first layer for which ΔV_2 represents the eroded volume. The parameter η is taken to be a constant defined by

$$\lim_{t \to \infty} \Delta V_1(t) = \eta V_1 \tag{13}$$

Then the evaluation of η can be made by assuming that a typical frustrum is enclosed by a rectangular parallelepiped with volume DH^2. The parameter η is related to the difference in volume between the parallelepiped and the volume of the frustrum,

$$\eta = 1 - \frac{\pi}{3}\left[\left(\frac{S}{H}\right)^2 + \left(\frac{Sr_o}{H^2}\right) + \left(\frac{r_o}{H}\right)^2\right] \qquad (14)$$

where r_o is the radius of the ring fracture at the surface of the platelet ($A_o = \pi r_o^2$) and S is the radius at the base of the frustrum a depth D below the surface. It is observed that a near dense array of frustrums remains after the interstitial material is removed for the 290 micron beads. In this case $H \approx 2S$, so

$$\eta = 1 - \frac{\pi}{12}\left[1 + \frac{r_o}{S} + \left(\frac{r_o}{S}\right)^2\right] \qquad (15)$$

Microscopic observation of the erosion process as a function of time for the 290 micron beads shows that the density of ring fractures increases to a maximum value and then decreases toward a number approaching that for an array of frustrums whose bases almost completely cover a unit area. Frustrums are removed with the interstitial material when their bases are not in contact with the bulk material but lie in-between two adjacent frustrums[1]. This behavior should be taken into account in the present formulation of the model. In the case of the 70 micron beads, the growth of nucleated pits and chipping of conical frustrums occur a very short time after a ring fracture develops.

The form of the governing equation for the erosion of the surface layer in the basic model can be compared with the corresponding equation derived in the earlier stages of this research (Reference 1, Eq. (4)) which may be written

$$\Delta V_1(t) = D \int_0^t G_1^2 (t-\tau)^2 \, I_1(\tau)(1-\Delta A_1(\tau))d\tau \qquad (16)$$

Substituting Eq. (7) into (8) and using Eq. (5), Eq. (4) becomes

$$\Delta V_1(t) = \eta D \int_0^t K_1(t-\tau)g(D)n\varphi(\tau)\left(1-\Delta A_1(\tau)-N(\tau)A_o\right)d\tau \qquad (17)$$

-37-

The general growth rate function $K_1(t-\tau)$ replaces $G_1^2(t-\tau)^2$ and the pit nucleation probability function is now more explicit,

$$I_1(t) = g(D)n\varphi(t) \tag{18}$$

The microscopic observation of the eroded surfaces also showed that the area of the number of rings nucleated should be excluded from the area available for additional ring fracture formation as indicated by the last term in Eq. (17).

Now that the erosion mechanisms contributing to ΔV_2 and ΔV_3 have also been identified, more explicit mathematical representations will be provided for determining the volume removal due to these stages of the general erosion process. For different erosion conditions the measured differences in the weight-loss data are associated with the time at which each erosion mechanism (contributing to ΔV_1, ΔV_2, or ΔV_3) becomes operative and the degree to which it influences the overall erosion behavior. It is now concluded that the overall erosion behavior can be described for a broad range of bead diameters and impact velocities in terms of the present formulation of the analytical model.

3.2.3 Experimental Evaluation of Model Parameters

Programs are underway to acquire data pertaining to each of the parameters required to obtain explicit results from the analytical model as represented by Eq. (9). Each of the four parameters, A_0, φ, D, and K_1 will be discussed here in relation to methods for obtaining the necessary information.

3.2.3.1 Ring Fracture Size Distribution and Probability Function

Quantitative data pertaining to the ring fractures formed by the collision of the glass beads with glass plates on a scale appropriate to solid particle erosion are required in the development of the basic model. Tests PY-12 to PY-19 (see Table I) were run to obtain information on the probabilities for ring fracture formation as a function of impact velocity. In order to determine the threshold velocity for ring fracture initiation, specimen PY-12 was run for 10 sec. intervals beginning at 38 fps and proceeding in increments of 19 fps in the velocity until ring fractures were observed on the surface. When ring fractures were found at approximately 170 fps, the number of rings at several locations on the specimen surface were counted using an optical microscope at 440X. These areas were then scanned a second time and the diameters of the rings were measured and recorded. The distribution of ring diameters for impact velocities of 188, 208, 226 and 246 fps are given in Fig. 7 to 10. The average diameter in each case is listed in Table VI. The average diameter of the ring fractures for an impact velocity of 246 fps is decisively greater than 226 fps and the distribution curves show a shift to an increased population of larger diameter rings. Each value was determined on a sampling of 200 rings. The agreement with the Hertzian theory (Table III) is excellent. Comparing the average ring diameter for Pyrex impacted by the 290 micron beads at approximately 200 fps with the corresponding value for fused silica, 3.17 mils compared with 2.63 mils[1], it is seen that there is a sizable difference between the two glasses. The explanation for this difference requires further investigation.

The near equality of the average ring diameter at velocities below 226 fps is not given any significance at this time, since the sampling at 208 fps was 130
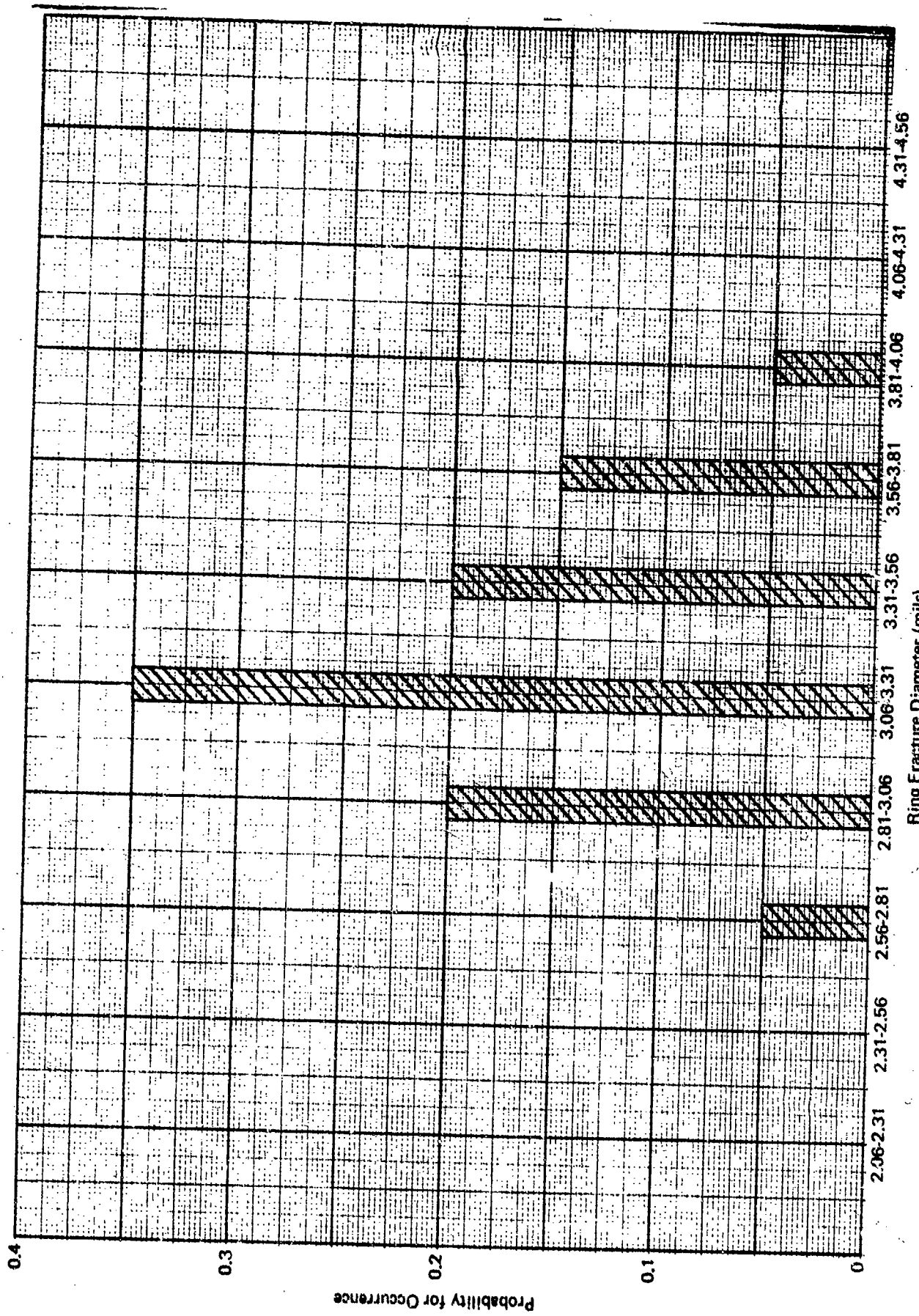
FIGURE 7. Distribution of ring fracture diameters for 290-micron beads at 188 fps
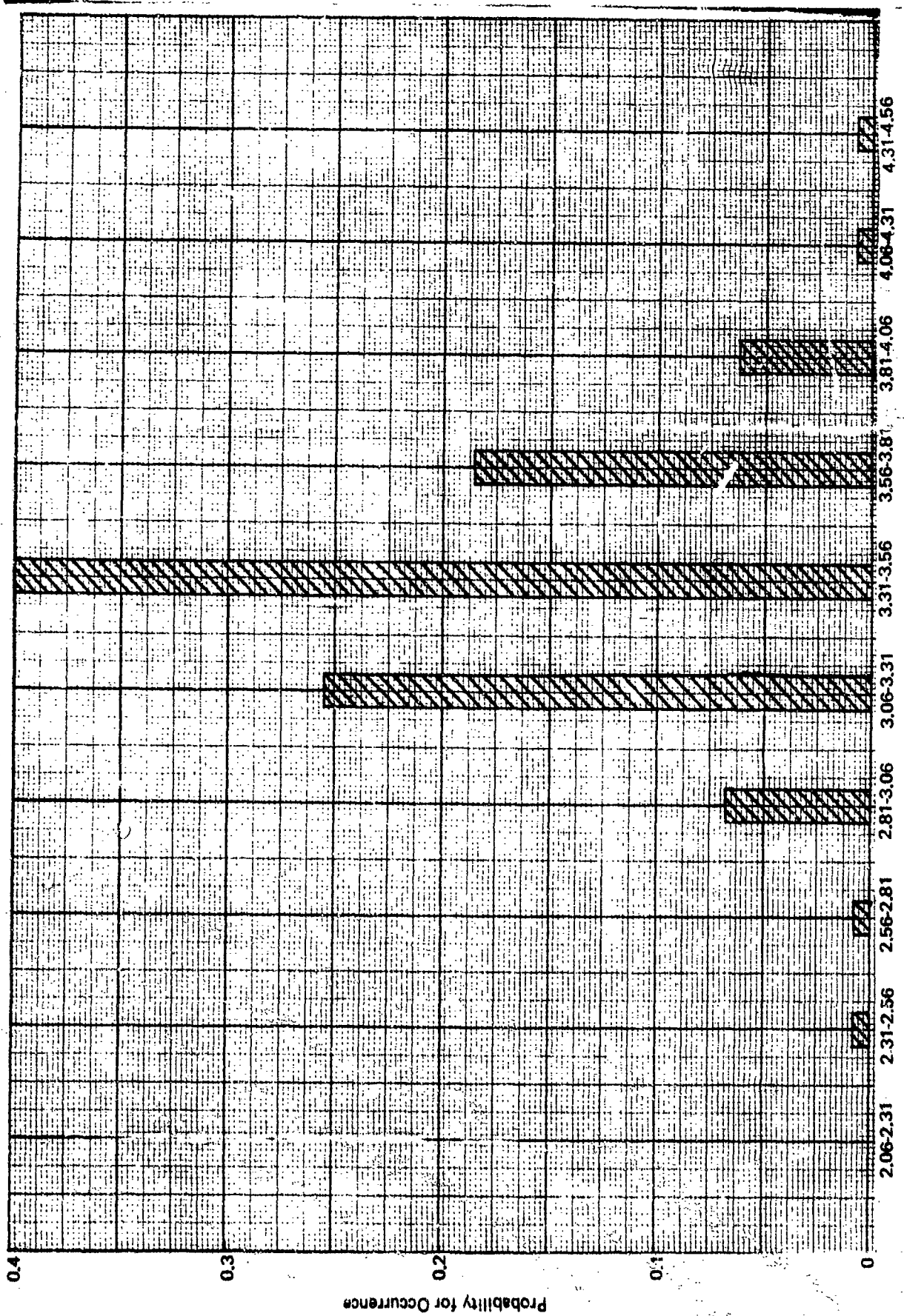
FIGURE 8. Distribution of ring fracture diameters for 290-micron beads at 208 fps
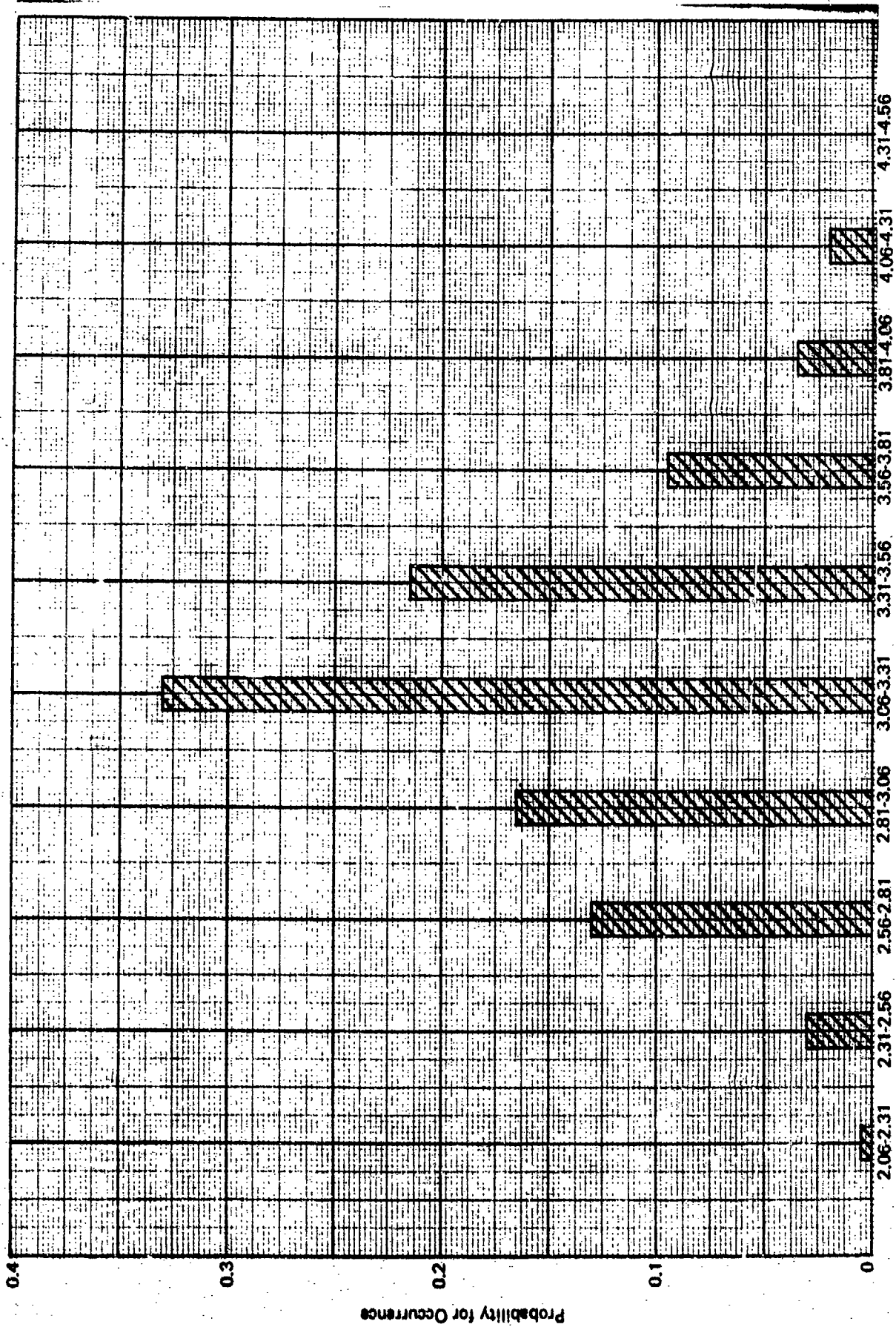
FIGURE 9. Distribution of ring fracture diameters for 290-micron beads at 226 fps
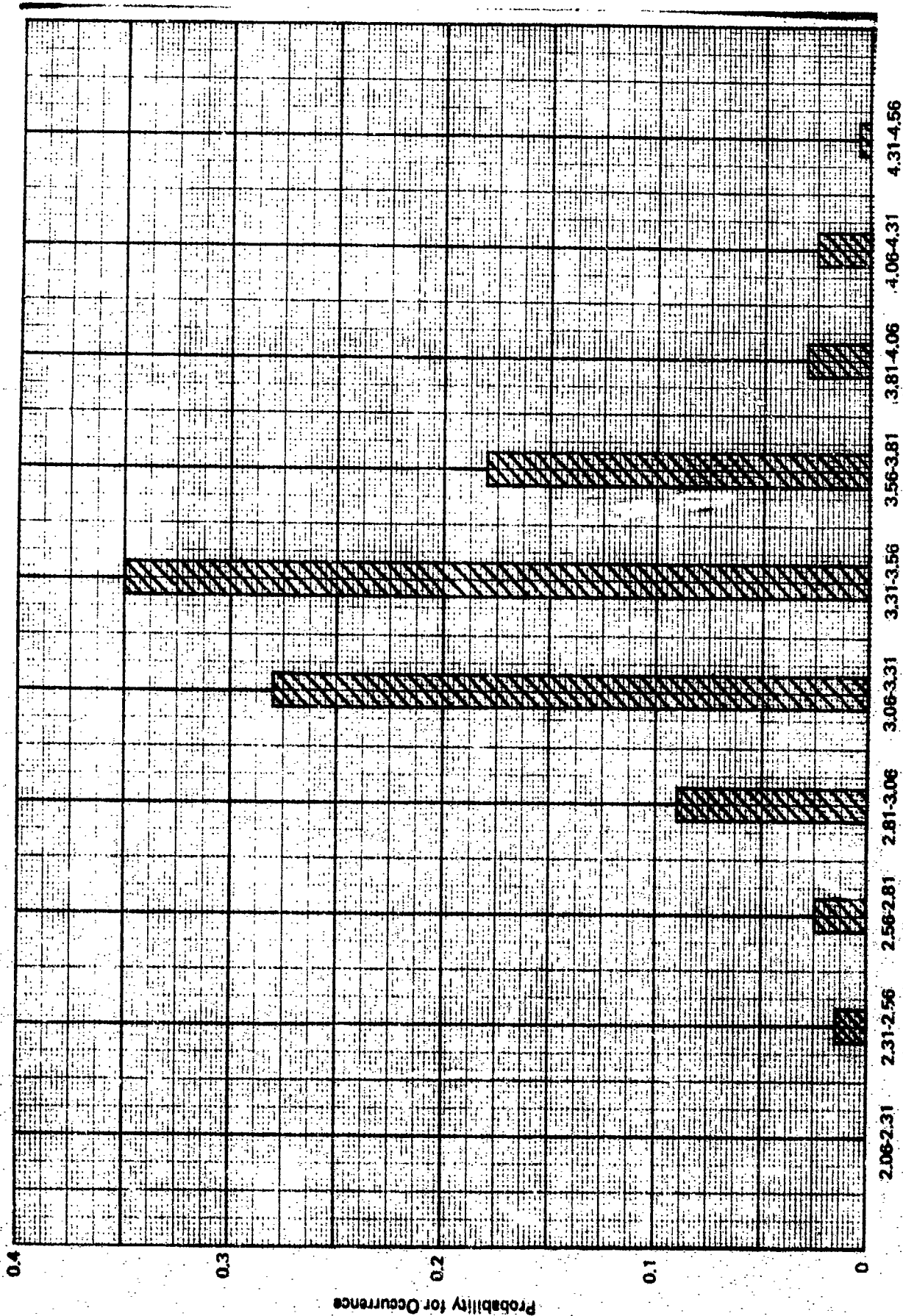
FIGURE 10. Distribution of ring fracture diameters for 290-micron beads at 246 fps

Ring Fracture Diameter (mils)

Probability for Occurrence

TABLE VI

RING FRACTURE PROBABILITIES AND AVERAGE DIAMETERS

Impact Velocity		Number of Impacts per sq. in.	Number of Ring Fractures per sq. in.	φ	Average Diameter of Ring Fracture (mils)
RPM	fps				
200	188	9,500	1,725	0.18	3.15
220	208	10,400	5,710	0.55	3.17
240	226	11,400	7,900	0.69	3.17
260	246	12,300	11,000	0.90	3.38

rings and at 188 fps it was only 40 rings due to the sparse
ring fracture population. These tests will be continued at
velocities greater than those reported here to observe further
the trend in the average ring diameter as a function of velo-
city. So far the results are most promising in terms of the
Hertzian analysis, since ring fractures generally do occur
slightly beyond the contact area as predicted by Hertz theory.

It was already pointed out that the proba-
bility for the formation of ring fractures is a time-dependent
function due to the changing surface condition of the glass
plate when progressively bombarded by the glass beads. Quan-
titative measurements of the time-variation of the probability
function φ will be made subsequently. The tabulations in
Table VI are simply based on the number of ring fractures
produced by a known number of bead impacts. These results
are still tentative but do provide some perspective on the
relationship between the impact velocity and φ.

A series of tests (PY-20 and PY-21) were
run in order to obtain the distribution of ring fracture dia-
meters for the 70-micron beads (Fig. 11 and 12). The mean
diameter at 375 fps is 1.25 mil and 1.28 mil at 450 fps. The
mean depth of the ring fracture surface was found to be
approximately 9 microns at 375 fps and 10 microns at 450 fps.
Both values are consistent with the Hertzian predictions of
the maximum contact diameters which are slightly less than
1 mil as computed in Table III. The data obtained are based
on the measurement of 200 ring fractures using optical micro-
scopy at a magnification of 440X.

3.2.3.2   Geometry of Conical Fracture Surfaces

When viewing the eroded surface of the
glass specimens in the microscope, the depth h of the cone
fractures can be measured in microns by focusing at the
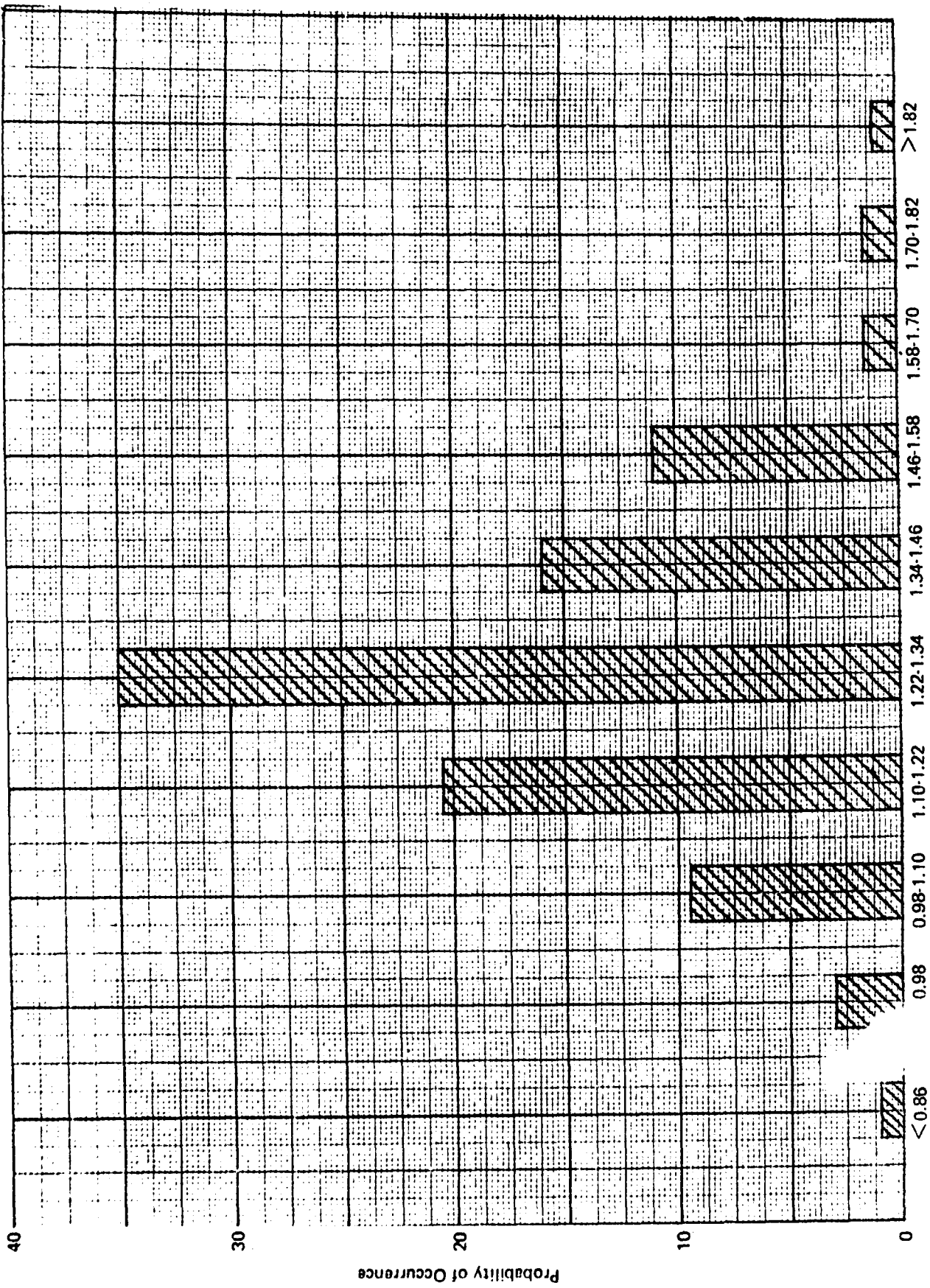
-49-

FIGURE   Distribution of ring fracture diameters for 70-micron glass
beads impacting on glass at 375 fps.
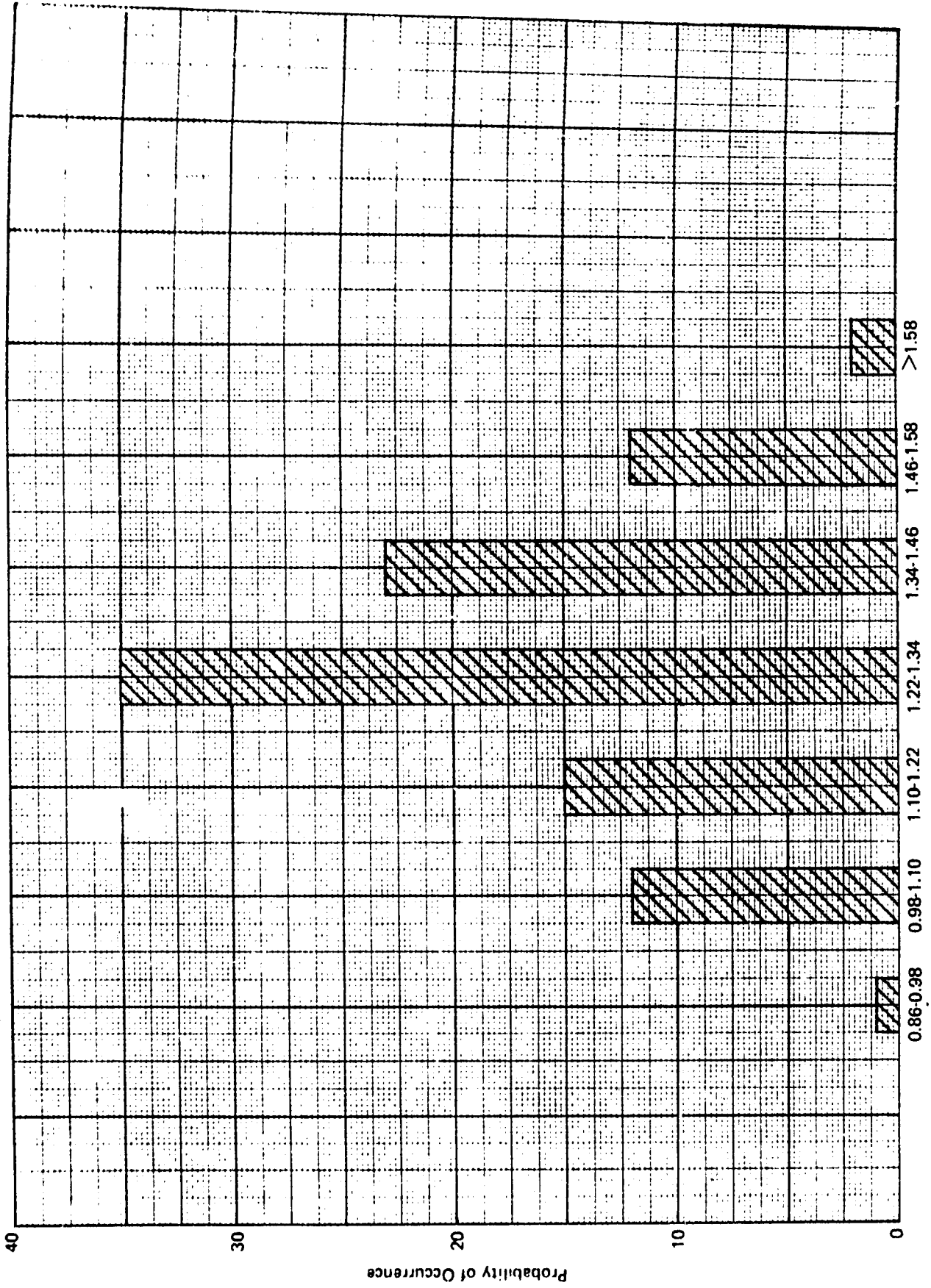
FIGURE 12 Distribution of ring fracture diameters for 70-micron glass beads impacting on glass at 450 fps.

surface and then the base of the frustrums once they are exposed. The lateral scale on the microscope can be read to an accuracy of a few microns. The tangent of the cone semi-angles obtained in this way never agreed with the values of 68.5° for glass and 65.5° for fused silica[3] measured under quasistatic loadings. The measured values of the semiangles under the present impact conditions were found to range from 45° to 60°. A similar observation was made by Bowden and Field[4] in conjunction with a lead slug striking the edge of a 0.25 in. glass plate which was 3 inches square. They observe from their high-speed photographic studies that an important feature of cone fractures is their angle of inclination with the top surface of the glass plate which lies primarily in the range of 50 to 60 degrees. This means that the included semi-angle is in the range of 30 to 40 degrees which is in conformity with the rough estimates made for the semi-angles for the primary cone fractures investigated in this program. Bowden and Field[4] note that if the horizontal and vertical displacements at the surface for the steady state solution of a Rayleigh wave are used to compute the direction of the maximum tensile stress, an included semi-angle of 34° is predicted. Due to the passage of a Rayleigh wave the material particles at the surface of a semi-infinite half-space follow an elliptical path with major axis in the vertical direction. When Poisson's ratio is 0.25, it turns out that the cotangent of the ratio of the major to minor axis of the elliptical path corresponds to an angle of approximately 34°; however the physical meaning of this result is not clear.

A number of investigators have considered the formation of cone fractures in glass plates, however there are only limited data pertaining to the fracture of glass specimens impacted by small diameter solid spheres. While qualitative aspects of the fracture process under these conditions can be described, the quantitative evaluation of the derived relations must await future experimentation on the specific materials used in the erosion tests.

The experimental work of Hamilton and Rawson[5] on two different glasses with various surface treatments indicates that the linear proportionality between the applied load and the indentor radius at fracture is not generally true in the Auerbach range[1]. The following relation is obtained

$$P_c = KR^{m'} \qquad (19)$$

where the values of K and m' listed in Table VII are determined from the data plotted in their paper. P_c is the critical fracture load applied to a spherical indenter of radius R. The values of the parameters K and m' are for P_c in kilograms and R in millimeters. On the basis of the variability in the form of Eq. (19), Hamilton and Rawson argue that the linear P_c-R (Auerbach) relation is not a universal relation and thereby dismiss Roesler's[6] argument that the linearity of the P_c-R relation would require a special flaw distribution function common to all brittle surfaces. It is our observation from the data reported by Hamilton and Rawson[5] that the relation for the Hertzian range

$$P_c = K'R^2 \qquad (20)$$

is similarly replaced by a general relation of the form given in Eq. (19). The values of K and m' for this case are also listed in Table VII.

Roesler[7] developed a scaling relation for describing the propagation of a Hertzian crack as the load applied to a cylindrical indenter is increased. The radius of the ring fracture, S, measured parallel to the plane of the glass plate asymptotically reaches a state which is described by the relation

$$2S = \kappa P^{2/3} \qquad (21)$$

TABLE VII

EXPERIMENTALLY-EVALUATED PARAMETER FOR
THE DETERMINATION OF THE CRITICAL FRACTURE LOAD

	Auerbach Range		Hertz Range	
	m'	K	m'	K
Polished Plate Glass				
As received	1.032	14.1	1.706	2.28
4 minute etch	0.812	32.0	1.671	5.29
7 minute etch	0.720	43.6	1.558	36.2
Float Glass				
Tin bath surface	0.778	35.5	1.606	6.14
Free surface	0.694	43.0	1.576	37.7

Roesler estimates that this relation holds for a load P equal to twice the load required for initiation of fracture, P_c, since after this point crushing of the glass surface takes place. The experiments in support of the scaling relation derived by Roesler were carried out with a flat-faced cylindrical indentor instead of a spherical indentor. According to Roesler these test conditions were used rather than the customary spherical indentor, since spherical indentors do not produce large and regular cone fractures. For spherical indentors secondary fractures, multiple ring fractures, develop as the contact area grows with increasing load. It will be assumed that Eq.(21) is also valid for a sphere impacting an elastic half-space.

Benbow[3] carried out a series of experiments employing the cylindrical indentor and an unidentified fused silica. The experimental results are reported in graphical form in his paper. The values obtained from the line fitted to the experimental data provides an explicit representation for Eq.(21). It is estimated that $\kappa = 3.84 \times 10^{-3}$ in/(lb)$^{2/3}$.

The depth of penetration of a single cone fracture can be determined from the information which has been accumulated. The load applied to the specimen by an impacting bead is determined by equating the kinetic energy of the impacting particle to the strain energy at the time of maximum impression. According to the Hertz-Huber theory,[1]

$$P_m = \frac{4}{3} \left(\frac{5}{4}\pi\rho_2\right)^{3/5} (k_1 + k_2)^{-2/5} V_o^{6/5} R^2 \tag{22}$$

where ρ_2 is the density of the impacting sphere

V_o is the impact velocity

$k_1 = \dfrac{1-\nu_1^2}{E_1}$, $k_2 = \dfrac{1-\nu_2^2}{E_2}$ are the elastic moduli for the sphere and half-space, respectively. (ν is Poisson's ration and E is Young's modulus).

Values of P_m are listed in Table III for the materials and impact conditions used in the experimental program. Assuming Roesler's scaling relation is valid for a spherical indenter,

$$2S = \kappa P_m^{2/3} \quad \text{when } P_m > P_c \qquad (23)$$

where according to the experimental data of Hamilton and Rawson[5] the critical fracture load is given by Eq.(19). Hence, referring to Fig. 13, we finally obtain

$$D = \frac{S-r_o}{\tan\beta} \qquad (24)$$

where $r_o = K_2 a$ is the radius of the inner ring fracture at the surface of the specimen and a is the radius of the contact area computed from Hertz theory.

For the present only very rough approximations will be made for the parameter appearing in Eq.(24). The coefficient κ in Eq.(23) will be equated to the value determined by Benbow for fused silica: $\kappa = 3.84 \times 10^{-3}$ in/ $(lb)^{2/3}$. The radius of the inner fracture ring will be equated to the radius of the maximum contact area determined from the Hertz-Huber theory and listed in Table III; and, until more accurate measurements have been made, β will be set equal to 60°. The values of D calculated for both bead radii and listed in Table VIII over the velocity range used in the experimental program are in general agreement with the experimentally-determined values. Table VIII also provides the values of the shape factors, η, calculated from Eq.(15) using the computed value of S and the value of $r_o = a$ as recorded in Table III.
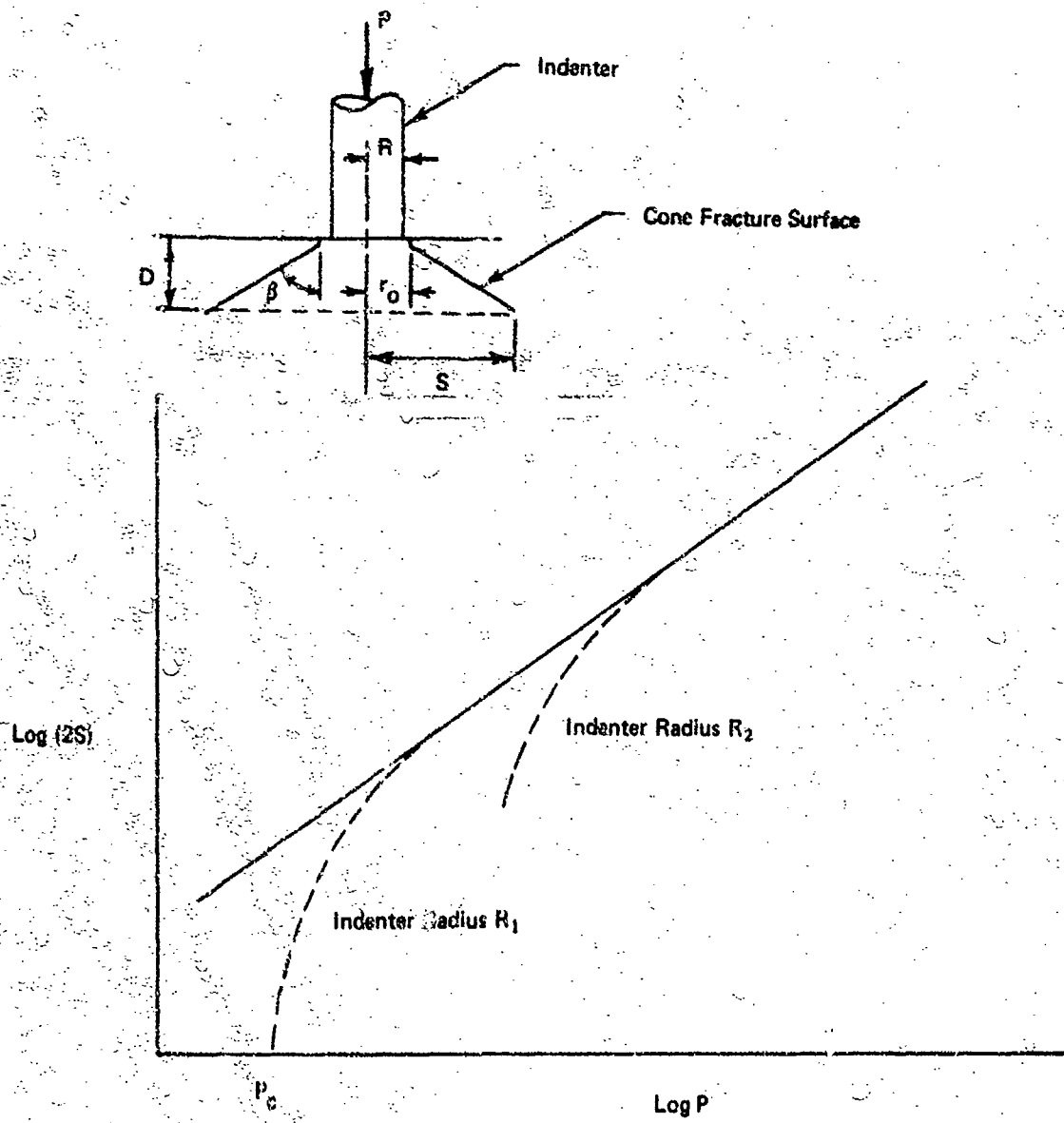
Figure 13. Relation between the Load Applied to a Cylindrical Indenter and the Maximum Radius of the Cone Fracture Produced in Glass

TABLE VIII

COMPUTED FRACTURE CONE GEOMETRIC PARAMETERS

	Radius at base of cone fracture, S(in.)	Depth of cone fracture below surface, D (in.)	Shape factor η
70 Micron Glass Beads			
200 fps	0.73×10^{-3}	0.204×10^{-3} (5.2μ)	0.552
300 fps	0.96×10^{-3}	0.306×10^{-3} (7.8μ)	0.577
400 fps	1.22×10^{-3}	0.433×10^{-3} (11.0μ)	0.601
500 fps	1.44×10^{-3}	0.508×10^{-3} (12.9μ)	0.614
290 Micron Glass Beads			
200 fps	4.48×10^{-3}	1.75×10^{-3} (44.5μ)	0.628
300 fps	6.25×10^{-3}	2.62×10^{-3} (66.5μ)	0.648
400 fps	7.90×10^{-3}	3.46×10^{-3} (88.0μ)	0.660
500 fps	9.35×10^{-3}	4.20×10^{-3} (106.5μ)	0.667

3.2.3.3 Eroded Area Growth Rates

The growth rate, $K_1(t)$, for nucleated erosion pits can be determined through direct observation of areas from which material is being removed as a function of the exposure time; however, for both bead sizes the areal patterns have geometrically intricate forms which are tedious to measure accurately. In order to obtain more detailed information for the statistical analysis of the growth rate function, an electronic image analyzer was used in conjunction with a low power optical microscope. The experimental setup was only preliminary in order to evaluate the feasibility of using this arrangement to obtain quantitative measures of the change in the eroded area at a number of locations on the specimen surface as a function of the time of exposure.

The evolution of damage on the surfce of a glass specimen impacted by 70 micron beads is shown in Fig. 4 and 5. In bright field the details of the eroded surface are suppressed but the outline of regions from which material has been removed standout as black patches on a white surface. A video camera is used to view a portion of the specimen surface through the eyepiece of an optical microscope. A magnification factor of 15 is satisfactory in accordance with the scale of the erosion damage.

By using the specular reflection characteristics of a smooth reflective surface, measurements can be made of the percentage of an arbitrary rectangular area that is undamaged. The first step in this evaluation is to illuminate the surface to separate, through the reflected light intensity, the original surface areas from the pitted areas. This is done by forcing the illumination angle and the viewing angle to both be perpendicular to the surface. The undamaged areas then appear very bright due to the strong specular reflection from them, while pitted areas appear dark. This lighting scheme is depicted in Fig. 14. If the intensity

Light Ray Striking
Undamaged
Perpendicular
Surface

50/50
Beam
Splitter

Light Source

Light Ray Striking
Damaged Oblique
Surface

Surface to be
Examined
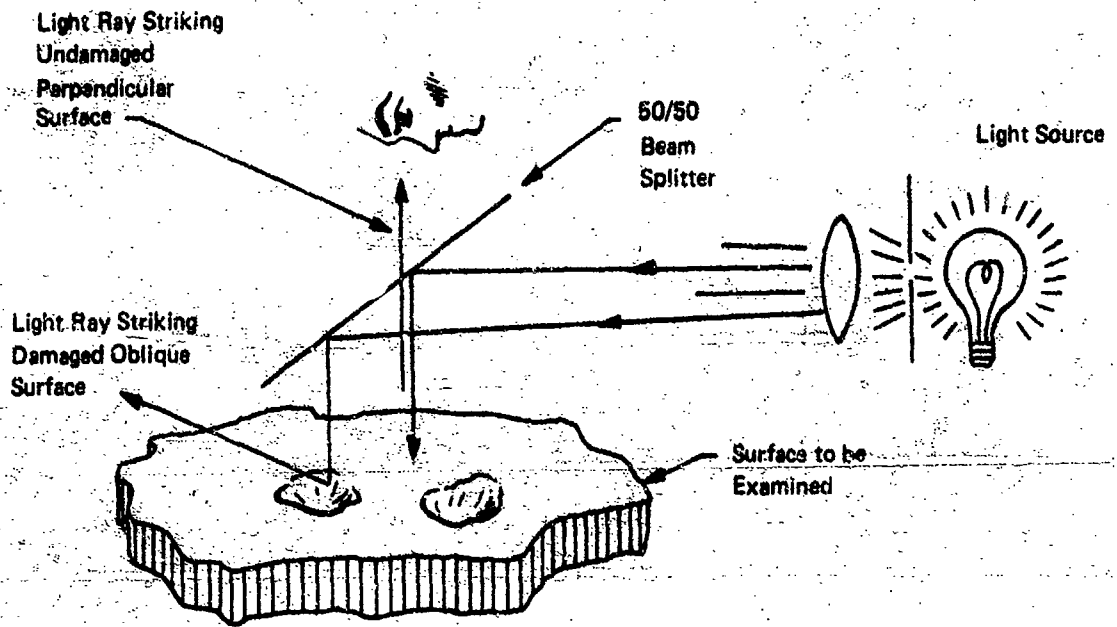
Figure 14   Illumination scheme to separate damaged regions from
undamaged regions by intensity

Relative
Area

Damaged
Surface

Undamaged
Surface

T

Intensity Increasing
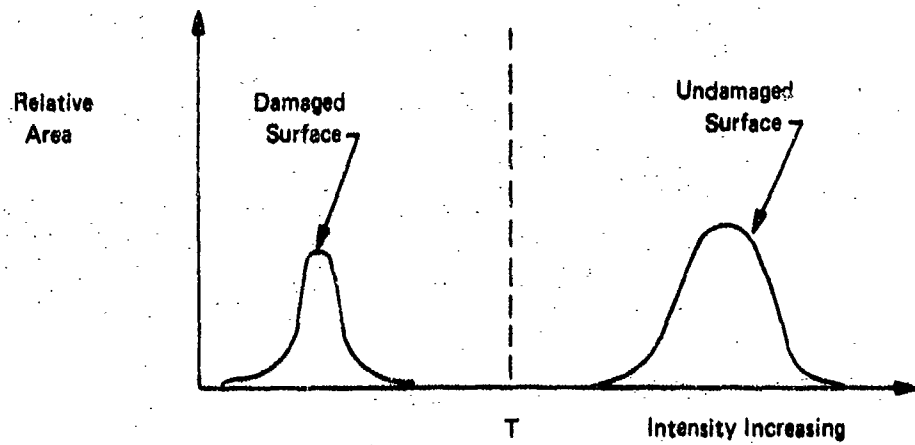
Figure 15   Intensity distributions of partially damaged surface

distribution of the surface, when viewed with this lighting were graphed, it would appear as in Fig. 15.

In subsequent development of the areal measurement equipment the surface, illuminated in the manner described, will be viewed by the television camera with the aid of a microscope equipped with a two-dimensional micrometer stage, so the same area can be viewed after additional exposure to the erosive environment. Since the video signal is a faithful voltage analog of the light intensity, the voltage distribution of the signal is the same as that shown in Fig. 14.

This video signal is first split into two components. A threshold circuit has a bilevel output; it is high whenever the input signal is above an arbitrary but fixed level and low when the input signal is below that level. If this threshold level is chosen to be T as shown in Fig. 15, then the threshold output will be high when undamaged surface is being scanned by the television camera and low when the surface being scanned is damaged. The relative amount of time the signal is high is then proportional to the amount of undamaged surface area in the video picture. The rest of the processor consists of a circuit to measure the amount of time the threshold signal is high. This is accomplished by gating an oscillator to a counter with the threshold video. An additional useful feature is a variable window which can be used to frame exactly that region to be measured.

The arrangement used in the initial tests included a plate which masked the face of the specimen except for a hole approximately 0.2 inch in diameter. A holder was fabricated for the specimen and a scale was used to position the hole over the same area on the specimen at the next increment in the exposure time. The accuracy in returning to the

same location was not satisfactory, so the readings taken at this stage in the development of the equipment are of little value. The sides of the hole in the plate also produced a reflection on the video picture which further hindered the attainment of acceptable results.

3.2.4 Weight-loss Data

Weight-loss data were obtained for the direct impact of the 290 micron glass beads in test numbers PY-10 and PY-11, and for the 70 micron glass beads in test numbers PY-22 and PY-23 as recorded in Table I. The weight-loss curves in each case are shown in Fig. 16 to 19. Reference to Table V provides information on the area exposed to the erosive environment and estimates of the number of particles striking the exposed area. It should be noted that the direct impact tests for the 290 micron glass beads were for a different experimental arrangement than that shown in Fig. 1. In this case 2.25 sq.in. of the specimen's surface are exposed to the bead impacts. In these initial tests the arrangement in the AFML-Bell erosion facility for dropping glass beads in the path of the specimen at the end of the rotating arm resulted in a non-uniform distribution of beads across a portion of the lateral dimension of the specimen. The disadvantage of this arrangement is that different areas on the specimen surface will be at different stages of the erosion process due to the non-uniform number of bead impacts occurring along the specimen surface. The measured weight-loss data are then reflecting the cumulative effect of two or more erosion mechanisms being operative as a function of the lateral dimensions of the specimen and not simply a function of the exposure time. Simple modifications were made in the nozzle at the end of the blast tube, but the desired result was not achieved. Cover plates were then used as indicated in Fig. 1 so that the specimen is exposed to a uniform distribution of particles which exists near the center of the stream of particles

falling in the path of the specimen. This modification in the testing procedure is more in line with the analytical model which does account for a temporal but not a spatial dependence of the erosion mechanisms that have been identified in the solid particle erosion of glass specimens. The nozzle used in tests PY-10 and PY-11 did spread the beads over the full length of the specimens; but when the arm was rotating, the density of bead collisions with the specimen was skewed to the outboard end.

The general form of the weight-loss curve in Fig. 16 correlates quite well with the microscopic observations of the operative erosion mechanisms as described in Section 3.2.1. On the basis of the analysis provided in Section 3.2.3.2 it is also possible to check quantitative details of the erosion process. The cone depth calculated for 290 micron beads at an impact velocity of 200 fps (test PY-10) is 1.75 mils (Table VIII). The mass of material comprising the surface layer of the specimen as defined in Section 3.2.2 is 144 mg. The volume of the surface layer is divided into two components: ΔV_1 representing the interstitial material for a dense rectangular array of frustrums covering the exposed surface area of the specimen, and ΔV_2 corresponding to the volume contained within the frustrums. The mass of the material in ΔV_1 is 90 mg. using the shape factor in Table VIII. The curve in Fig. 16 shows an initial incubation period before measurable weight loss occurs, a period of accelerated weight loss when the material is removed from the highly-fractured interstitial region between the more erosion resistant frustrums, and a period of uniform material removal corresponding to chipping of the frustrums and the bulk material. Microscopic examination of specimen PY-10 at the end of the test indicated that most of the surface layer was removed except for a small portion of the surface at the inboard end of the specimen where frustrums were still intact. The calculated mass of material corresponding to ΔV_1 and V_1 show excellent agreement with observed erosion behavior of the specimen.
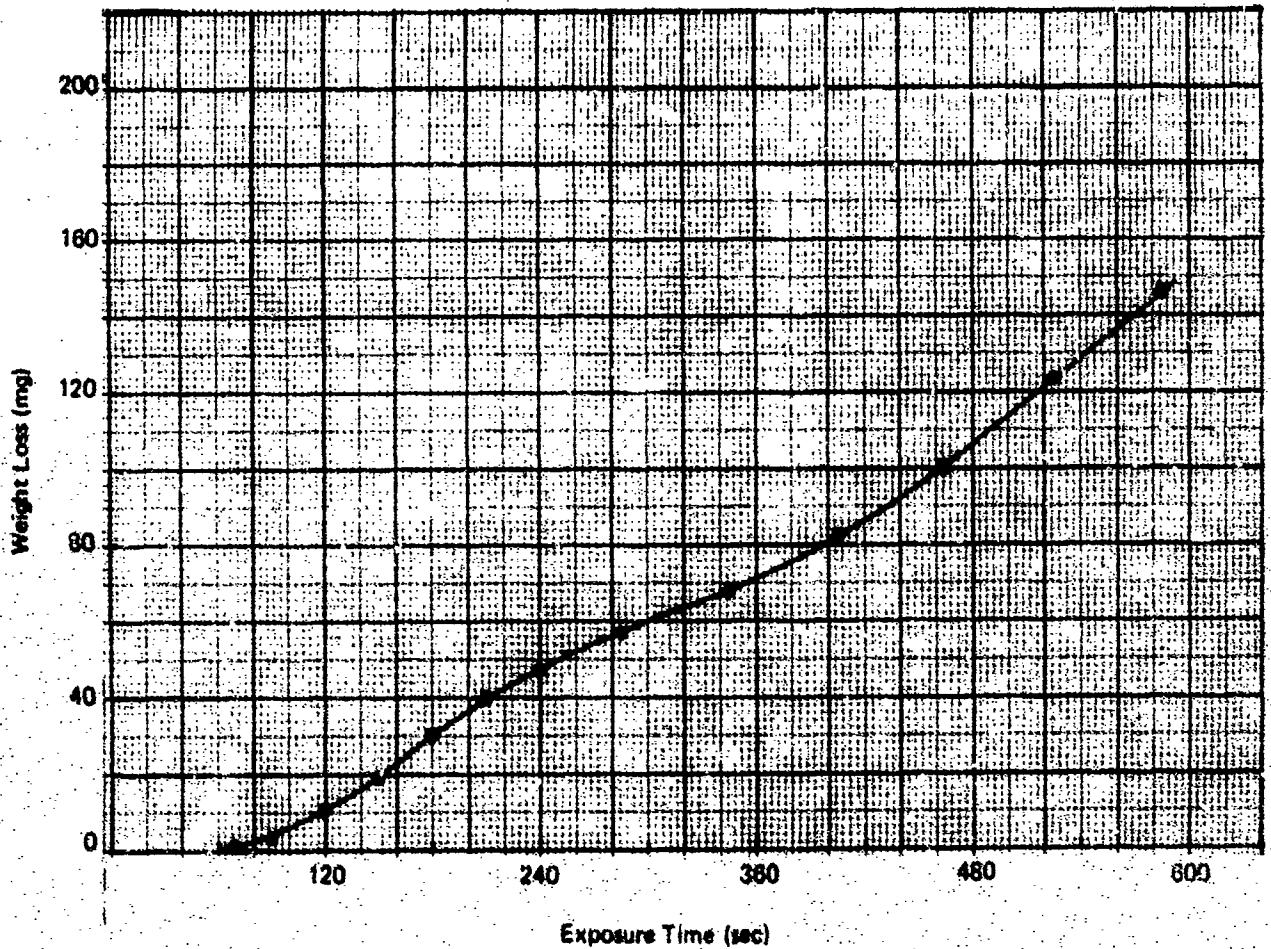
Figure 16   Weight-loss data for specimen PY-10 impacted by
290-micron glass beads at 200 fps

A similar analysis for test PY-11 (Fig. 17) indicated that the mass of material corresponding to ΔV_1 and V_1 is 218 mg. and 328 mg., respectively. Microscopic examination of specimen PY-11 revealed that relatively few collisions were occurring over the inboard half of the specimen. When the test was terminated, the surface layer at the outboard end of the specimen was almost completely removed, but about one-sixth of the specimen surface was sparsely eroded at the inboard end. A moderately dense array of frustrums covered the central portion of the specimen. Since several erosion mechanisms were operative across the lateral dimensions of the specimen, it is difficult to correlate the anticipated erosion behavior with the form of the curve in Fig. 17. However, on the basis of the condition of the eroded specimen surface at the end of the test, the calculated masses for the surface layer are quite reasonable.

The weight-loss data for the 70-micron glass beads impacting glass specimens PY-22 at 375 fps and PY-23 at 450 fps and a bead flow rate of 950 g/min are given in Fig. 18 and 19. A second glass specimen was run in each case (PY-25 and PY-26) to obtain the weight loss during the early stages of the erosion process and these results are also shown in the figures. The duration of the initial stage of the erosion process is seen to vary considerably between the specimens tested; however, the indication in Fig. 19 is that the erosion rates are comparable in the later stages of the erosion process, even though the magnitude of the weight loss may not be close for the same exposure time.

Again, using the data in Table VIII, the mass of the surface layer for specimen PY-22 and PY-23 is 11.9 mg and 14.3 mg, respectively. The surface area exposed to particle impacts is 0.821 sq.in. Referring to Fig. 18 and 19, it is seen that the 70 micron beads do not produce the bulge in the weight-loss data as in the case of the 290 micron beads. The steady-state erosion rate is quite uniform at
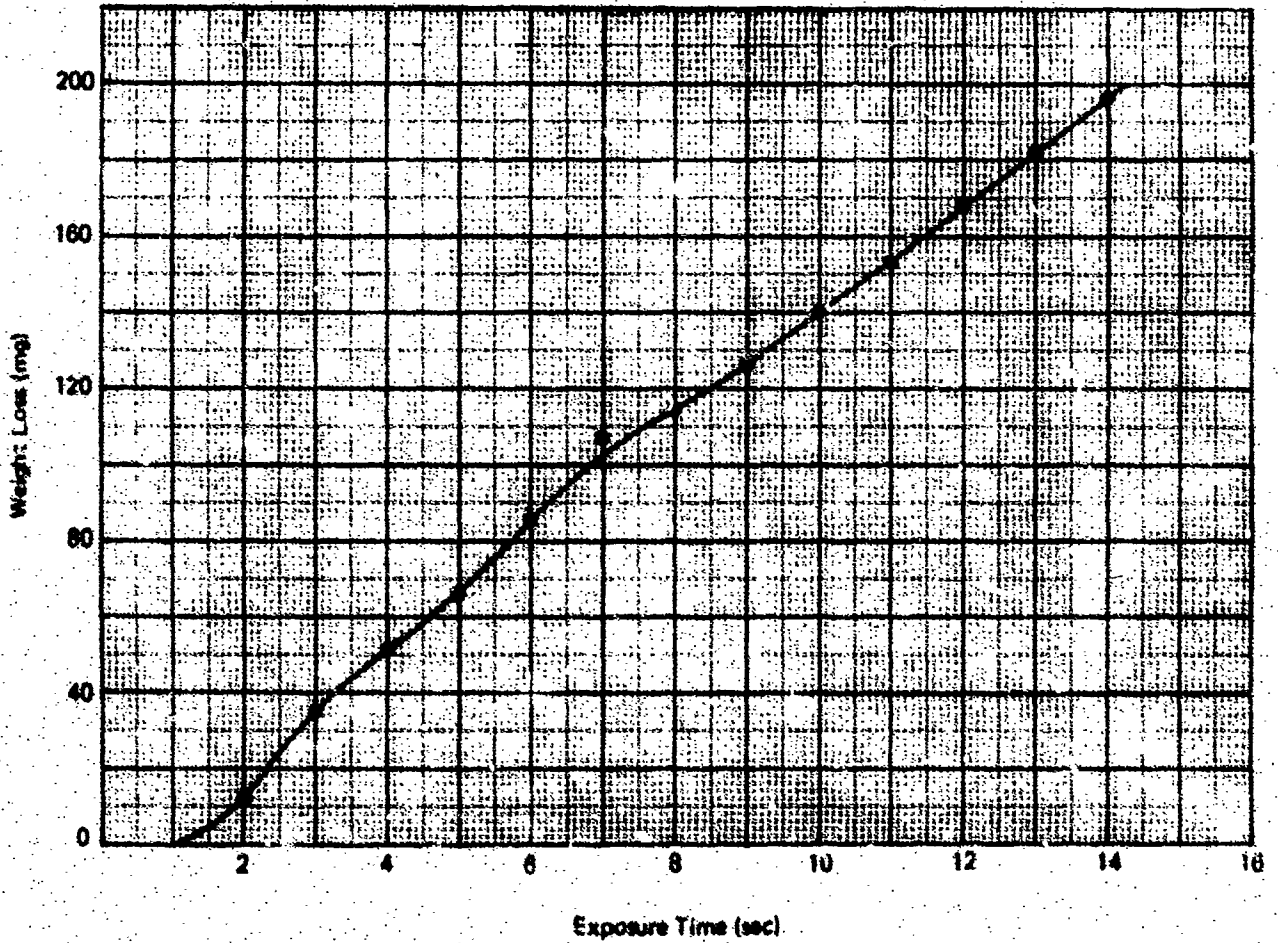
FIGURE 17   Weight-loss data for specimen XY-11 impacted by
290-micron glass beads at 375 fps
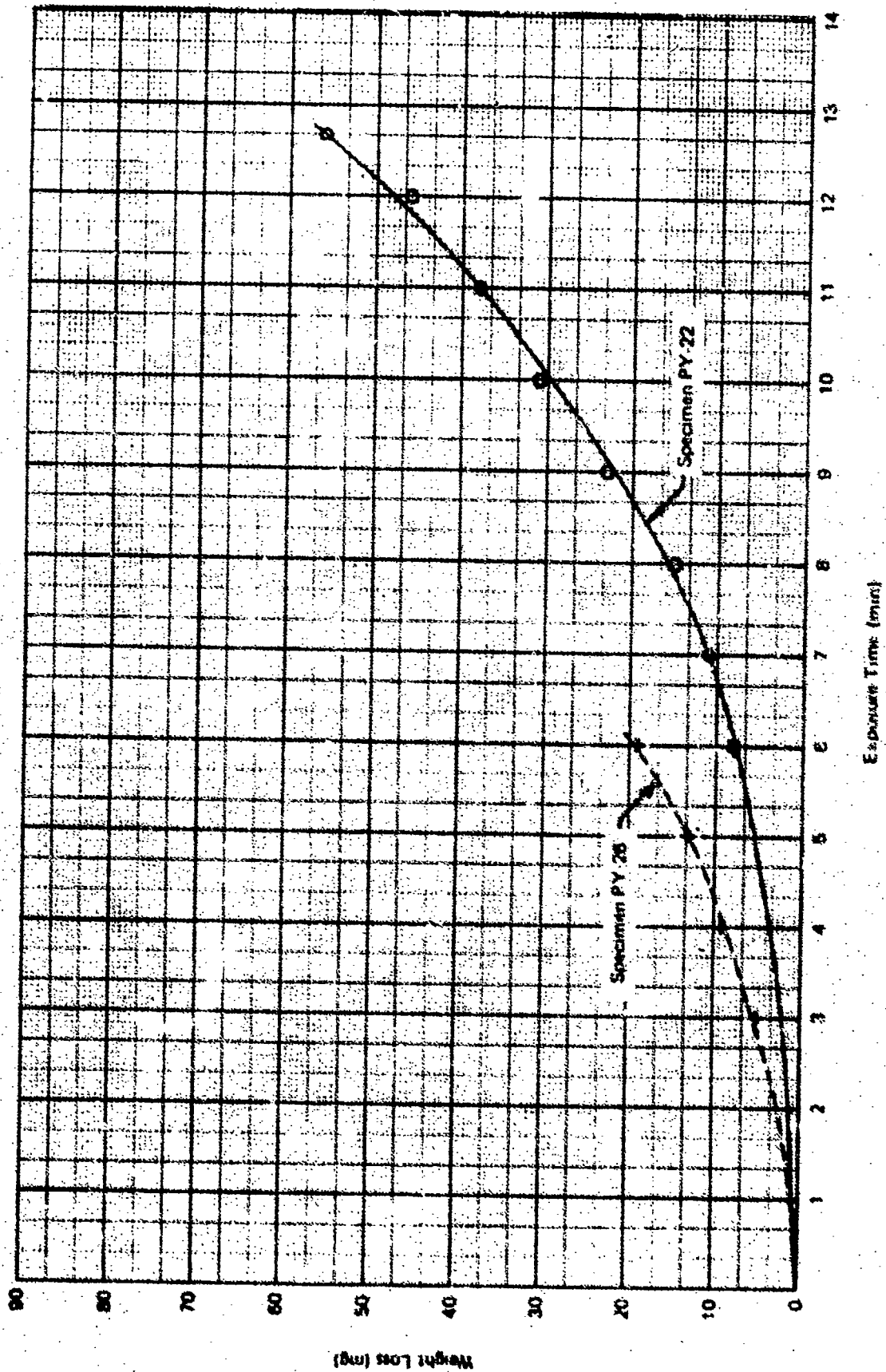
FIGURE 18 Weight loss for direct impacts of 70-micron glass beads on glass at 375 cps.

Figure 17 Weight loss for direct impact of 70-micron glass beads on
glass at 450 fps.

an impact velocity of 450 fps but shows less uniformity at
375 fps. After the initial period depicted in Fig. 4 and 5
the process of material removal is oy fine-scale chipping of
the bulk material.

The conical frustrums formed on the surface
of the glass specimens by 70-micron beads impacting at 375
fps are shown in Fig. 20. The removal of material is in the
immediate vicinity of each ring shortly after the rings
appear on the surface. Fig. 20 can be compared with Fig. 6
where a dense array of ring fractures develops before large-
scale material removal takes place. The condition of the
surface in the latter stages of the erosion process is illus-
trated in Fig. 21. It shows the uniform fine-scale chipping
of the highly fractured surface. The scale of the erosion
particles can be compared with those due to impacts by the
290-micron beads as shown in Fig. 6.

3.3 Oblique Impact by Glass Beads

In order to evaluate the extent of the erosion
damage produced by the 70- and 290-micron glass beads and the
90-micron sand impacting obliquely as compared to direct
impacts, the particle flow rates and the particle velocity
normal to the specimen's surface were maintained at the values
used for direct impacts. Under these conditions the total
number of particle impacts encountered by the specimens in
each case will be the same after equal exposure times if

$$N_I \text{ (oblique)} \times \text{(RPM)} = N_I \text{ (direct)} \times \text{(RPM)} \qquad (25)$$

where N_I is the number of particles per which the specimen experi-
ences per revolution of the rotating arm. Introducing Eq.(1)
into Eq.(24)

Figure 3.   Coolant fracture structure due to
Zr-niobra bonds deposition at 525 fps
(x300)
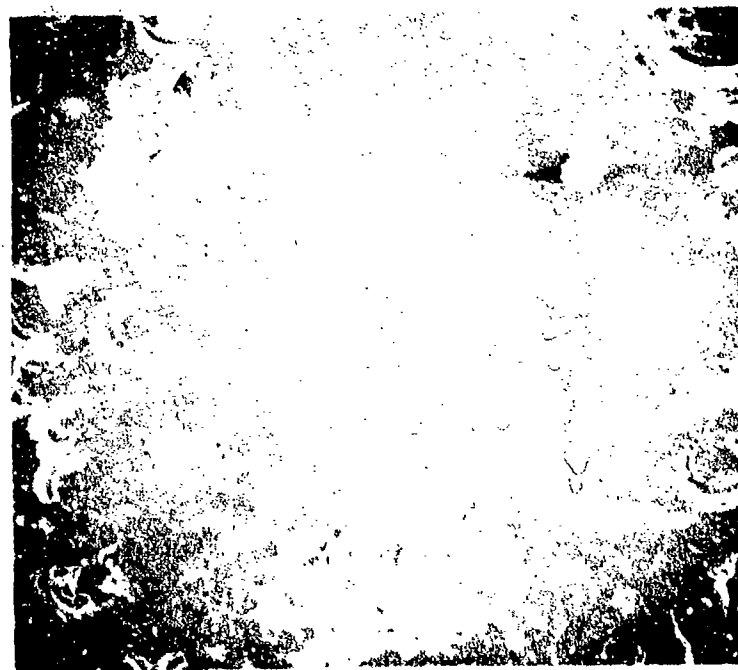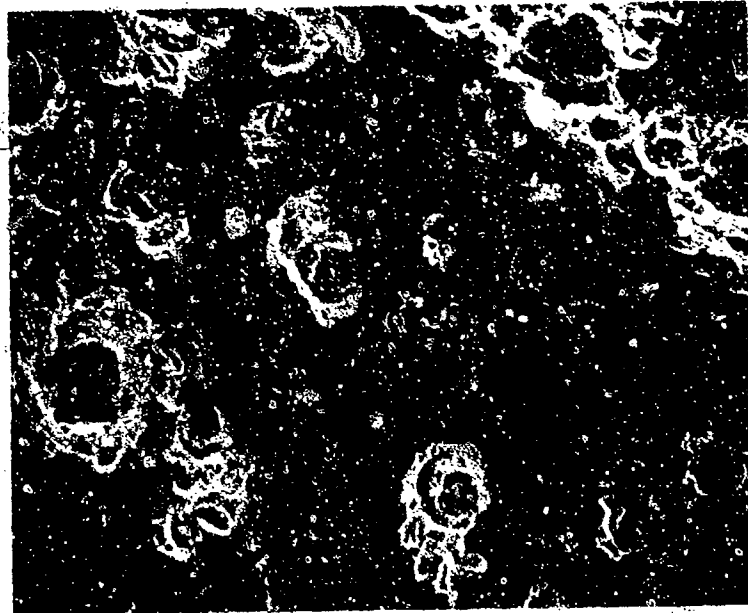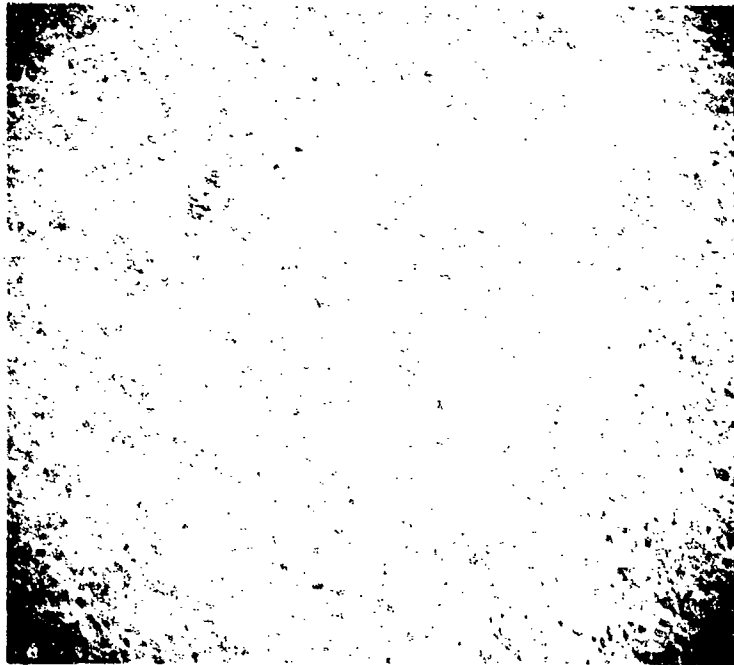
Figure 21   Eroded surface of a glass specimen at
            an advanced stage of the erosion process
            due to 70-micron beads impacting at
            375 fps (116X).

$$\left(\frac{N}{720\sqrt{2gh}}\right)\left(\frac{\ell_2 d_2 \cos\Theta}{\ell}\right)\left(\frac{n}{\cos\Theta}\right) = \left(\frac{N}{720\sqrt{2gh}}\right)\left(\frac{\ell_1 d_1}{\ell}\right) n \qquad (26)$$

where the slight difference in the nozzle dimension, ℓ, for each case has been neglected and n is the number of revolutions per minute for direct impacts. It is seen from Eq. (26) that the weight-loss data for oblique impacts can be compared with that for direct impacts by multiplying the values of the weight loss for the oblique impacts by the ratio of the exposed areas. For the 290 micron beads the exposed area for direct impacts is 2.25 sq.in. while it is 0.82 sq.in. for the 70 micron beads using the experimental arrangement shown in Fig. 1. The exposed area for oblique impacts is 1.81 sq. in. in both cases. It follows from Eq. (26) that

$$\frac{A_1}{A_2} = \frac{\ell_1 d_1}{\ell_2 d_2} \qquad (27)$$

The ratio of the areas for the 290 micron beads is 1.25 and 0.453 for the 70 micron beads. The weight-loss data for oblique impacts are plotted both in terms of the actual measurements and with the adjustment for the difference in the eroding areas.

3.3.1 Oblique Impact by 290-Micron Glass Beads

The weight-loss data for normal impact velocities of 200 and 300 fps and a bead flow rate of 370 g/min. are given in Fig. 22 and 23. It is noted that the convex hump appearing in the weight-loss data for direct impacts (Fig. 16 and 17) after the initiation stage corresponding to the sequence of erosion mechanisms described in Section 3.2.1 is also present for the oblique impacts. Comparison of the curves for a normal impact velocity of 200 fps shows that the weight loss for the oblique impacts is from two to three times higher than that for direct impacts at the same values of the exposure time. The magnitude of the weight loss can be brought

FIGURE 22 Weight loss for oblique impacts of 290-micron glass beads on glass at a normal impact velocity of 200 fps. (Test PY-34).

FIGURE 23 Weight loss for oblique impacts of 290-micron glass beads on glass at a normal impact velocity of 300 fps. (Test PY-35)

-70-

into coincidence with that in Fig. 16 if the time scale in
Fig. 22 is expanded by a factor of two.

Microscopic examination of a series of incre-
mentally eroded specimens revealed that the operative erosion
mechanisms were identical to those already-discovered for
direct impacts of 290 micron beads. At the termination of
test PY-34 material was completely removed from the inter-
stitial regions and chipping of the protruding frustrums was
taking place. Test PY-35 was terminated at a point where the
exposed frustrums were still intact and a small portion of
interstitial material could still be observed on the eroded
surface. These observations correspond to the characteristic
shapes of the weight-loss data reported in Fig. 22 and 23.
The particular phase of the overall erosion process predomin-
ating as the exposure time increased appeared uniformly over
the face of the specimen.

Detailed microscopic examination of the cone
fracture showed that they were circular at the surface of the
specimen. Histograms of the diameter of the surface ring
fracture are given in Fig. 24 for specimen PY-38 and PY-39
and in Fig. 25 for specimen PY-36. The mean diameter of the
ring fracture is 3.28 mils at 200 fps and 3.80 mils at 375 fps.
These values are based on a sampling of more than 125 ring
fractures. The mean cone penetration depth below the surface
of the specimen is 1 mil (25μ) at 200 fps and 1.6 mil (40μ)
at 375 fps. These depths are somewhat below those computed
in Table VIII. The corresponding cone fracture data for direct
impacts are a mean ring diameter of 3.17 mils and cone depth
of $25-30\mu$ at 200 fps and a mean ring diameter of 3.72 mils
and cone depth of 65μ at 375 fps.
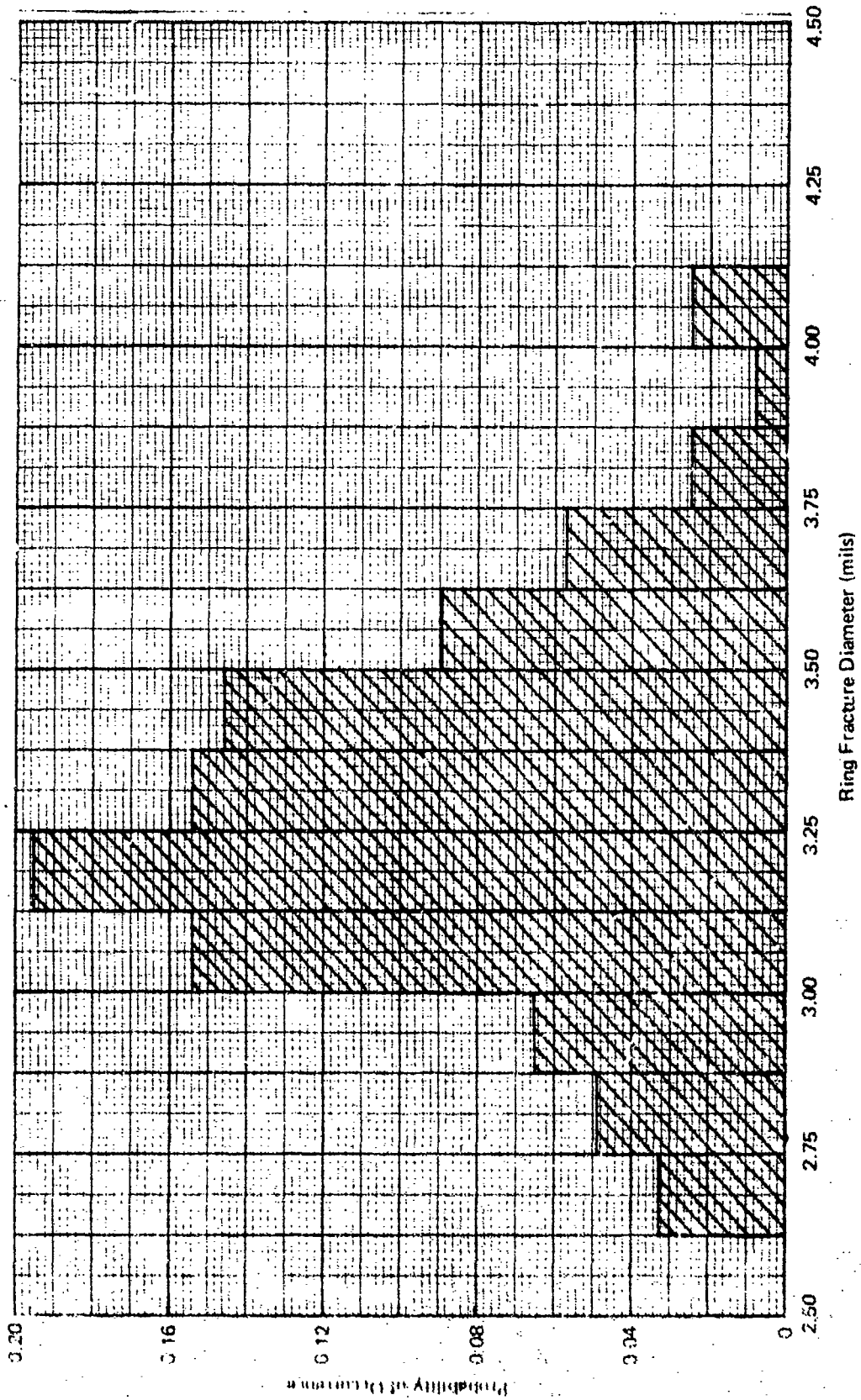
Figure 24 Distribution of ring fracture diameters on the surface of specimen PY-38.
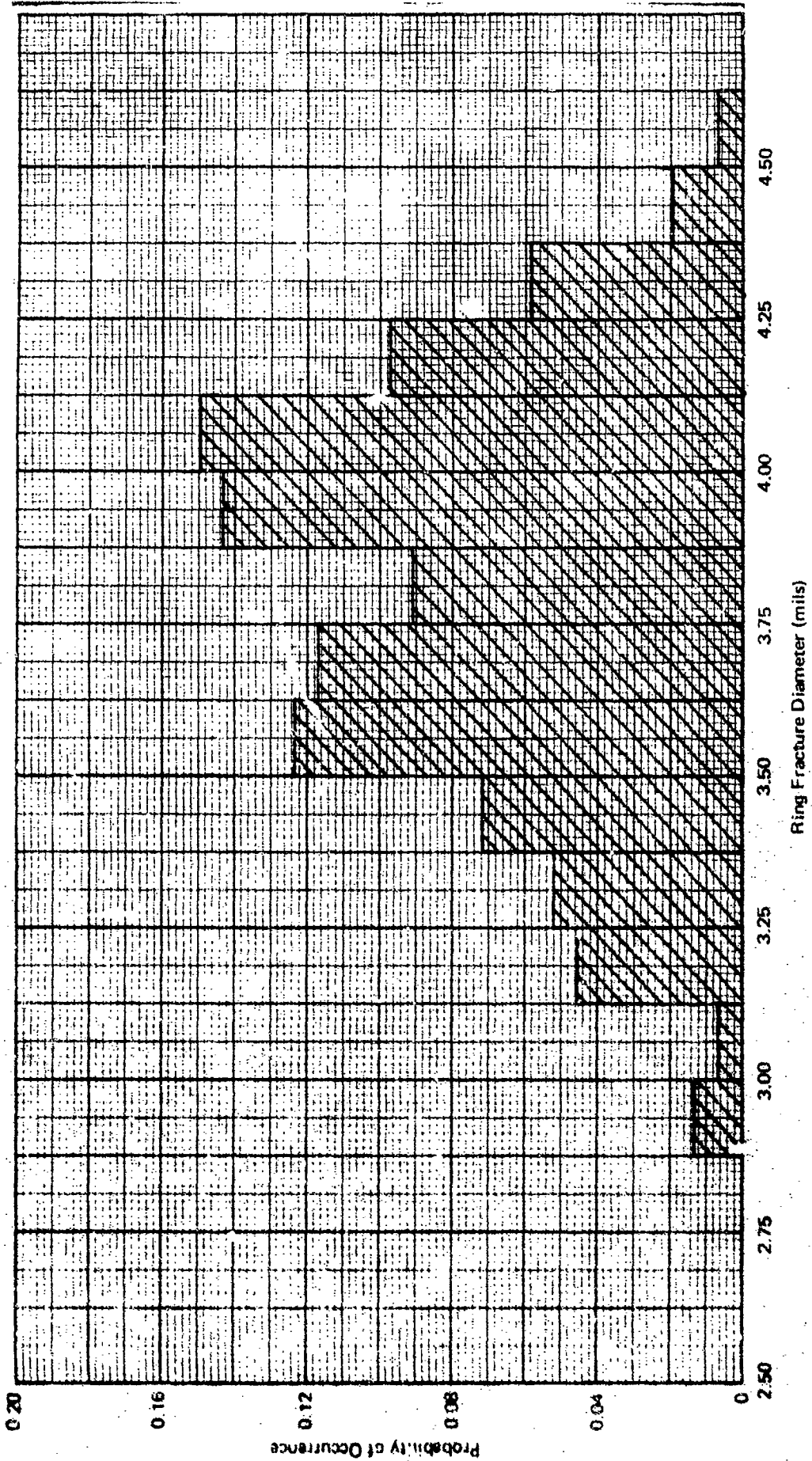
Figure 25   Distribution of ring fracture diameters on the surface
of specimen FV-3C.

3.3.2 Oblique Impact by 70-Micron Glass Beads

Weight-loss data were obtained at normal impact velocities of 300 and 375 fps at the same bead flow rate of 950 g/min. used in the direct impact tests. Fig. 26 and 27 indicate that a steady-state erosion rate has not been achieved even at exposure times which are well in excess of those required to remove the surface layer of material from the specimen. Comparison of the weight-loss data obtained for oblique and direct impacts at a normal velocity of 375 fps (Fig. 18 and 27) indicates that the values of the weight loss for glass plate at an impact angle of 50° are from two to four times greater than the direct impact case. Again, as in the case of the 290-micron beads, closer agreement can be achieved if the time axis in Fig. 27 is expanded by a factor of two. From the limited data available it appears that the erosion rates are comparable at the same exposure times, however the probability for ring fracture formation is greatly enhanced for the oblique impacts.

3.4 Direct and Oblique Impact of Irregularly-Shaped Particles

Most of the work on solid particle erosion has been involved with the long-time, steady-state erosion rates. Models describing the steady-state erosion by solid particles have been developed on the basis of laboratory erosion tests employing sandblast testers. The basic premise employed in these semi-empirical models is that a certain amount of energy is required to remove material from the surface of a target material and that each material has a characteristic erosion resistance. Two different modes of particulate erosion are distinguished empirically corresponding to ductile and brittle erosion behavior of the target material. In sandblast experiments uniformly-graded sand particles carried by a high-velocity airstream impact the target material. The
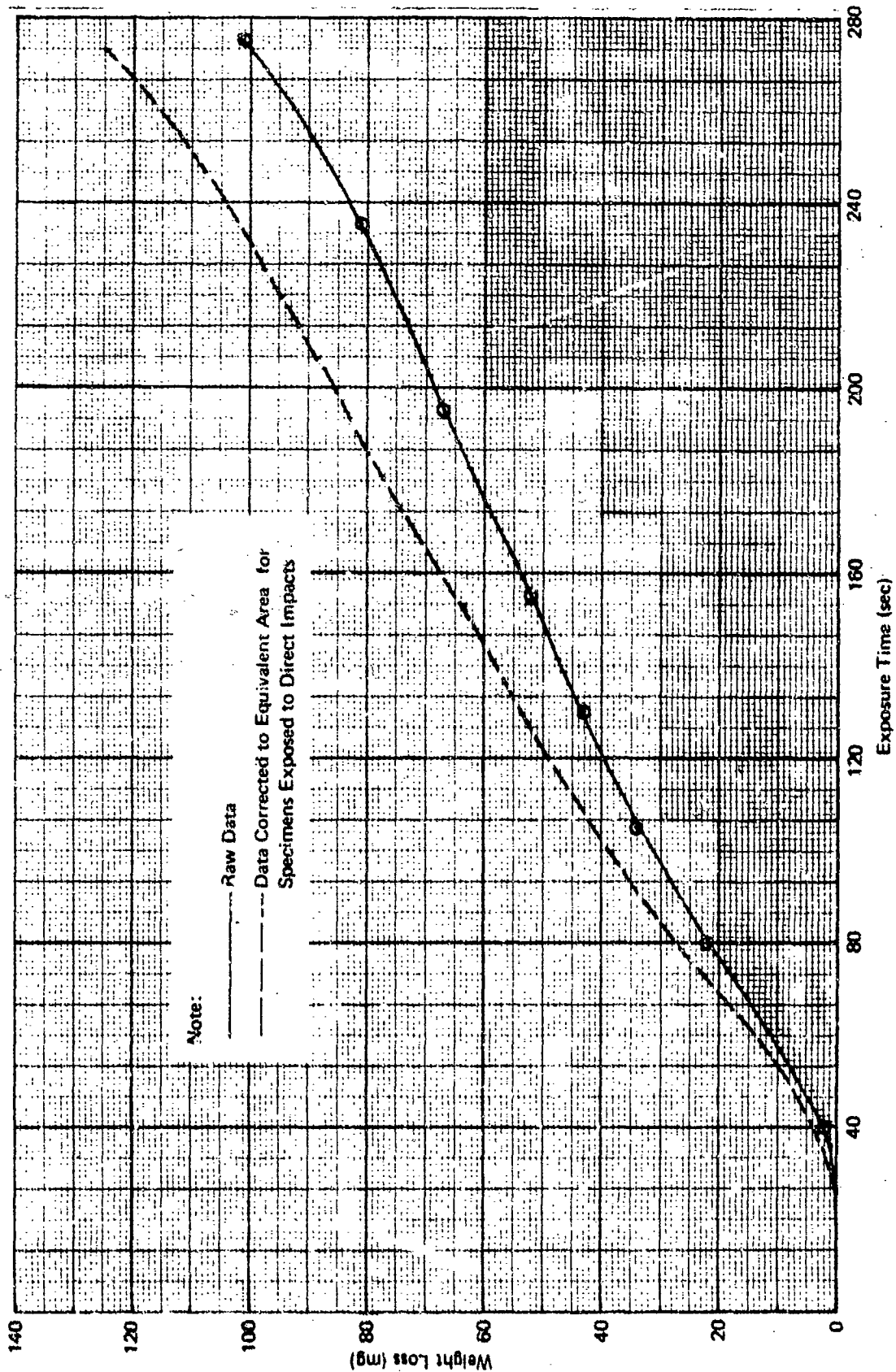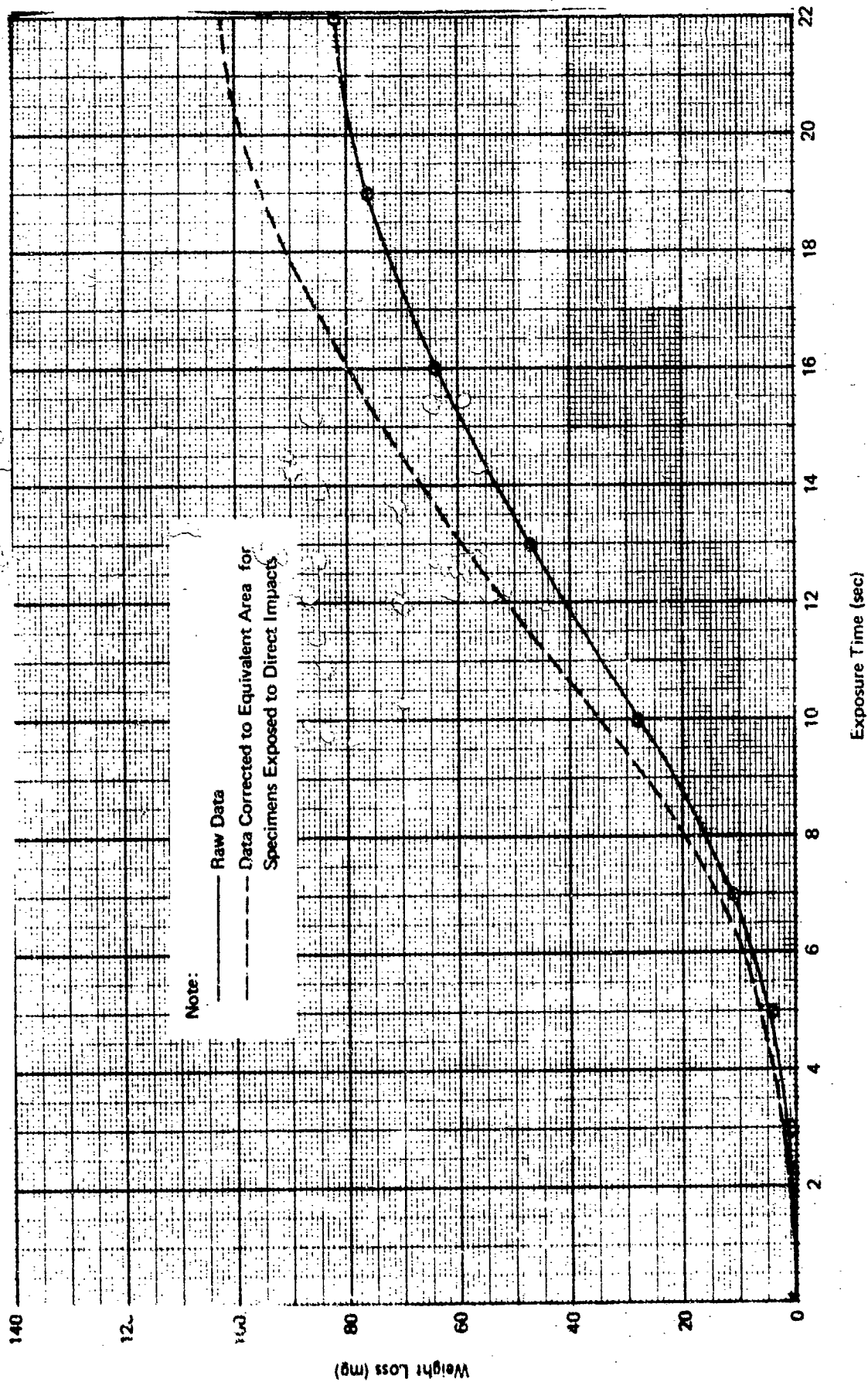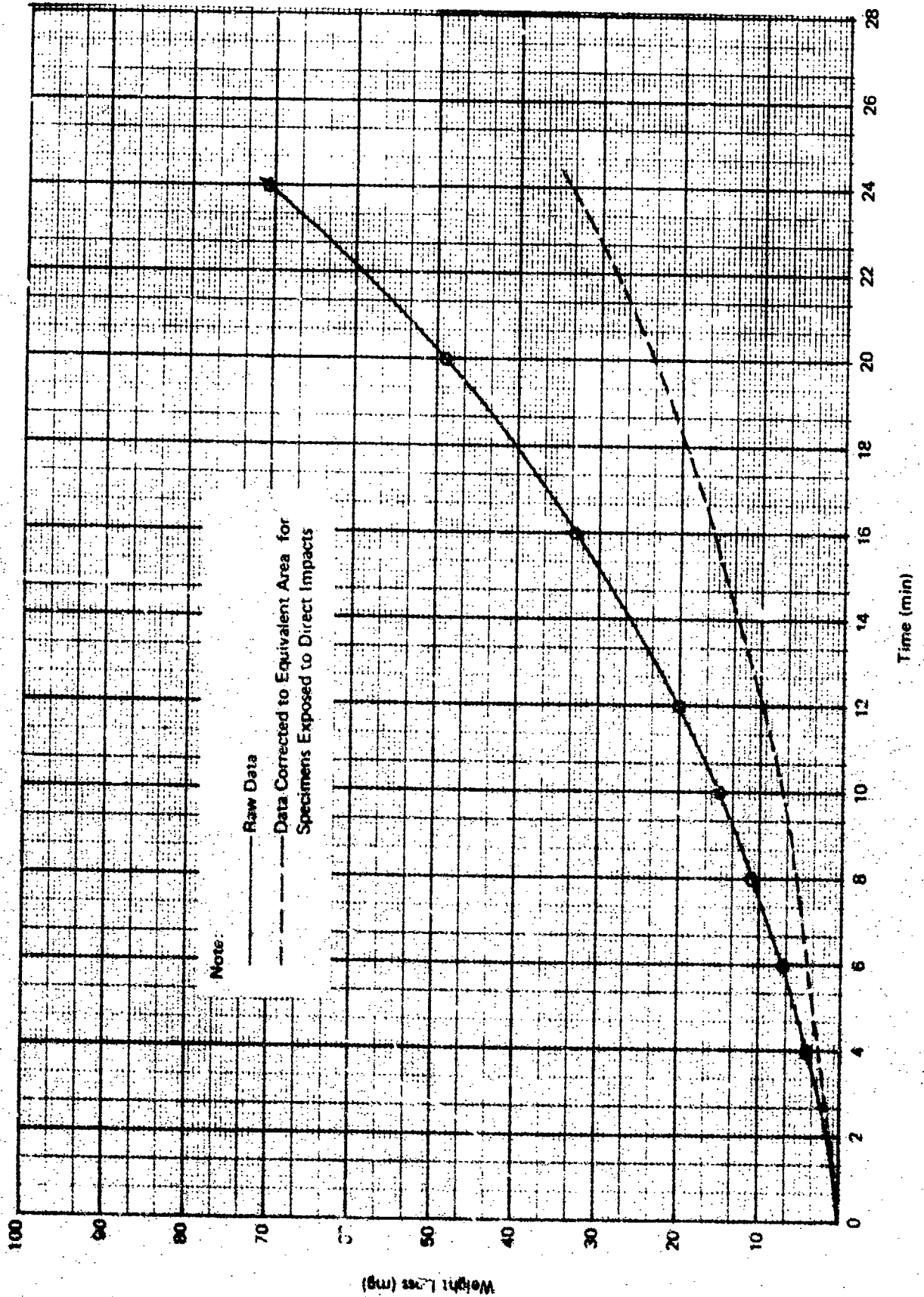
FIGURE 26. Weight loss for oblique impacts of 70-micron glass beads on glass at a normal impact velocity of 300 fps. (Test PY-30)
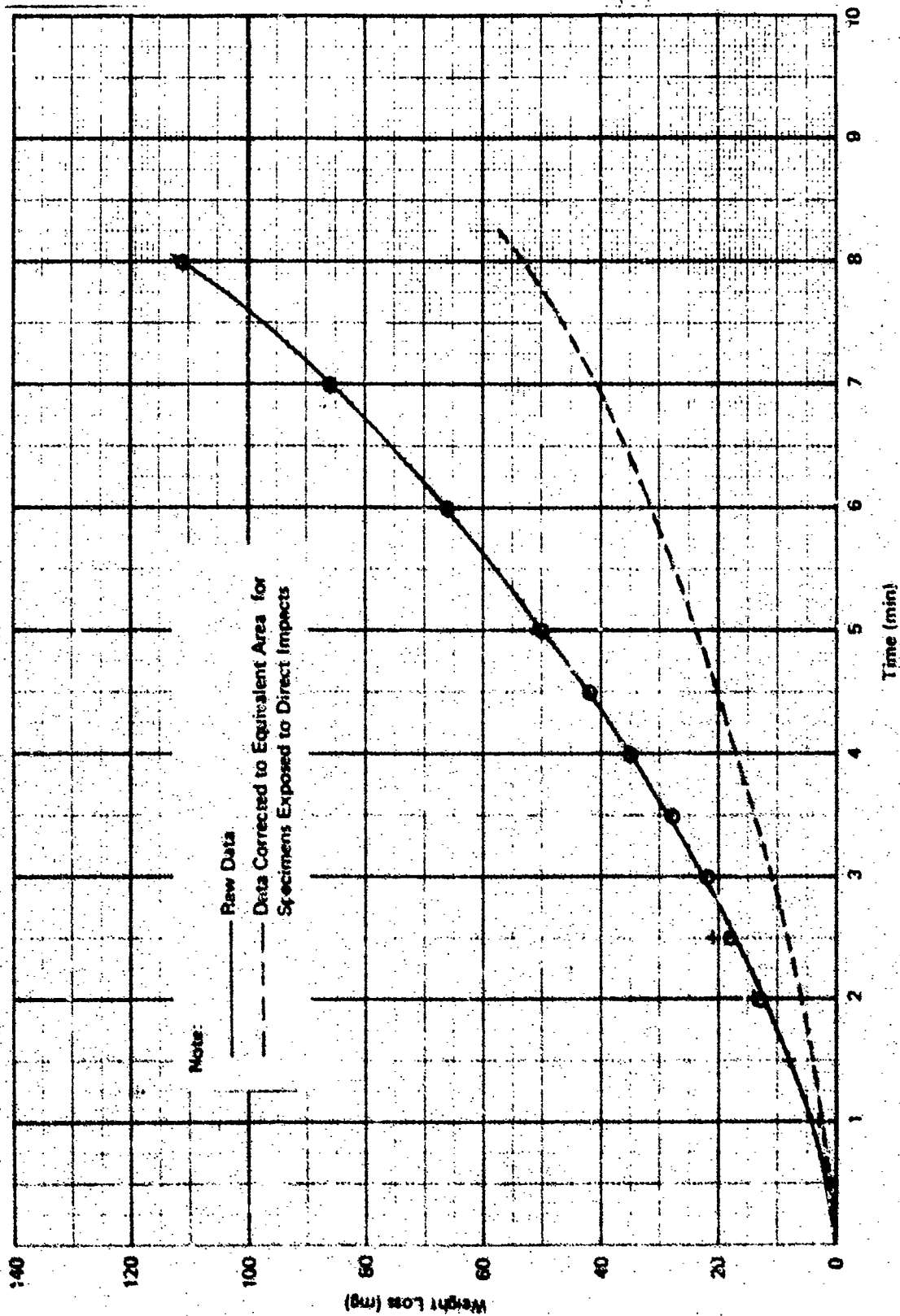
FIGURE 27 Weight loss for oblique impacts of 70-micron glass beads on glass at a normal impact velocity of 375 fps. (Test PY-31)

-76-

results of the test are reported in terms of the mass of
material removed per mass of impacting particles.

The research reported here is an initial effort in
extending the concepts and experimental correlations esta-
blished for spherical particles to irregularly-shaped quartz
sand particles. The experimental procedure employing the AFML-
Bell rotating arm differs from the solid particle erosion
tests conducted in the sandblast apparatus in that the com-
ponent of the impact velocity normal to the specimen surface
was held constant in the direct and oblique impact tests.
These conditions afforded an opportunity to evaluate the
influence of the velocity component tangent to the surface of
the specimen on the erosion behavior of the glass plate.
Only a slight increase in erosion rate was found and no real
distinction could be observed microscopically in the damage
due to obliquely impacting irregularly-shaped particles
compared with direct impacts.

3.4.1   Erosion of Materials by Irregularly-Shaped Solid Particles

Finnie[8,9] developed a mathematical model
for describing the erosion of ductile materials as a func-
tion of impingement angle based on an erosion mechanism whereby
material removal is entirely due to the displacing or cutting
action of an abrasive particle impacting a perfectly plastic
material surface. The equation derived by Finnie was moder-
ately successful in describing the angular dependence of the
steady-state erosion rate for a given set of particle and
regime parameters on the basis of a single erosion test. The
model predicted that there would be no erosion of ductile
metals at normal impingement angles, however this result does
not agree with the experimental findings. More general models
were proposed by Bitter[10] and Neilson and Gilchrist[11]
which included both cutting wear (proposed by Finnie) and
erosion due to repeated deformation. Repeated deformation is

responsible for cracking the surface of a brittle material
with subsequent intersection of cracks and material removal.
These equations provide better curve fitting of the experi-
mental data. These formulas include the idea of a particle
energy threshold below which deformation erosion ceases and
a minimum effective angle of impingement below which ductile
erosion ceases. Implementation of Bitter's model requires
knowledge of the energies required to remove a unit volume
of a material by cutting wear and deformation wear, respec-
tively. These parameters are determined by performing at
least two tests and back-calculating to determine the neces-
sary values. Neilson and Gilchrist[11] provided simpler
equations for deformation wear than those of Bitter[10] which
were able to account for the angular dependence of the erosion
process and included another parameter to be evaluated experi-
mentally which is the normal velocity component below which
no erosion takes place. These models have no predictive capa-
city to describe the steady-state erosion of brittle and
ductile materials eroded by natural contaminants composed of
a distribution of particle sizes and shapes.

In general, the erosion rate is a function
of a number of parameters associated with the impact regime,
the impacting particles, the target, and the particle/target
interaction. The accumulation of experimental data has shown
the relative importance of some of the impact regime para-
meters which include the distribution of the particle impact
velocities, impingement angle, and concentration. The par-
ticle parameters are the distribution of particle sizes,
shapes, and quantitative measures of physical and mechanical
properties. The target parameters include quantitative mea-
sures of its physical and mechanical properties and the
condition of the surface before exposure to the eroding envi-
ronment.

The experimental data obtained for glass bead impacts on glass plates have successfully defined the operative erosion mechanisms associated with a set of conditions which could be used to gain understanding for modeling the general erosion process for arbitrarily-shaped quartz sand particles. The use of glass beads and glass plates made possible the introduction of mathematical analysis to provide a rational basis for the inclusion of particular particle, target, and regime parameters. This includes the influence of particle size and velocity; however further extension of the model to sand erosion of brittle materials requires detailed information on the quantitative characterization of irregularly-shaped particles, the contribution of a particular size particle in a distribution of particle sizes to the overall erosion rate, and the influence of the angle of attack on erosion behavior.

The approximate particle size distributions used to establish some correspondence between the quartz sand and spherical glass beads used in the controlled erosion tests is not adequate to provide a quantitative measure of the geometry of irregularly-shaped solid particles. In order to evaluate the relative erosiveness of a given solid particle environment it is important to be able to characterize a given sample of particulate matter by means of simple parameters which define the shape of the individual particles. A survey of the literature on classification of particulate matter which is of general interest in erosion research revealed that there is no adequate set of parameters to provide a quantitative description of particle shape.

Hausner[12] has enumerated several requirements for a suitable method for describing the shape of a particle. These requirements and assumptions are listed below as amended by Heywood[13] and further modified here.

(1) The quantification of particle shape
is a three-dimensional problem, however
from the standpoint of practicality it
is treated as a two-dimensional problem.

(2) The diameter, or any other quantity
related to the actual size of the par-
ticle, should not be used in the
characterization of particle shape.
Shape is a geometrical property distinct
from size.

(3) A characterization of particle shape
must consist of a series of factors,
the knowledge of which should permit
drawing an approximate sketch of the
particle.

An additional observation by Hausner is that even the best
characterization of particle shape will be an approximation.
He then proceeds to define three parameters which are descrip-
tors of particle shape: the elongation, bulkiness, and surface
factors. These factors are not independent of those proposed
by other investigations.

The lack of uniqueness in specifying the size
of an irregularly-shaped particle is discussed in detail by
Kaye[14] especially for particle with re-entrant particle pro-
files. Statistically-evaluated Feret's and Martin's diameters
are compared for this case. Feret's diameter is the projected
length of the particle profile with respect to a fixed direc-
tion. Martin's diameter is the length of the line through
the particle profile parallel to a fixed direction which
divides the particle profile into two equal areas. He states
that Feret's diameter, which is consistent with the shape fac-
tors proposed by Hausner and others, is identified as the
diameter of a circle with a perimeter equivalent to that of

the particles, whereas Martin's diameter does not appear to have a simple relationship to any obvious particle physical parameter.

A small portion of the quartz sand particles shown in Fig. 3 exhibit re-entrant particle profiles. Kaye[14] defines a convex hull which does not include convex portions of the particle profile and shows how Feret's diameter is still meaningful based on the concept of a convex hull. The involution of the particle profile would be the difference between the actual particle perimeter and the perimeter of the convex hull. In general, the majority of the quartz sand particles used in this study are angular with a small percentage of acicular particles: the percentage of acicular particles increases as the particle size decreases.

The particle characteristics usually reported in the literature on solid particle erosion are the mesh-size of the particles used. Only Head and coworkers[15-17] have included more details pertaining to particle characteristics in their erosion tests and modeling studies.

After completion of an extensive testing program[15], Head and Harr[16] attempted to develop a model applicable to natural soils which includes consideration of the energy transferred from the impinging particles to the target, the nature of the response of the target, and the nature of the erosive agent including pertinent descriptors of composition, angularity, hardness, and size distribution. The result of this effort was the development of a weighted regression analysis program (WRAP model) in which

$$A = f \left(\frac{V^2}{E}, R, \sin\alpha, \cos\alpha, \frac{H}{E}, \frac{B}{E} \right) \tag{28}$$

where A is the erosion rate measured in volume removed per unit mass of dust, V is the effective velocity of the mix, R

is the effective roundness derived from a quantitative evaluation of the particle shapes, H is the effective hardness of the dust particles, α is the particle impingement angle, B is the hardness of the target, and E is the erosion resistance per unit volume of target. Head and Harr use the effective parameters which they define as the sum of the parameters associated with the individual size components of the dust weighted on the basis of the grain-size distribution of the dust. A different form of interaction between the dependent variables was found for brittle and ductile materials.

The WRAP model includes the influence of particle size as a weighting function for other parameters and a single factor, Wadell's roundness parameter[18], is employed to characterize the shape of the particles. On the basis of the earlier discussion, this mode of particles characterization is probably not adequate to provide good predictions of the erosiveness of a range of particle geometries and size distributions. An alternative statistical formulation will be considered.

The predictive ability of the WRAP model for brittle materials was not determined by Head and Harr[16], however the predictive capability of the WRAP model was subsequently evaluated for two ductile metals (type 302 stainless steel and 6061-T6 aluminum) eroded by 220 mesh alumina particles and 220 mesh fluorite particles[17]. When the model was adjusted for a higher maximum particle velocity, 300 m/sec. as opposed to 185 m/sec in the earlier work imparted by the carrier gas and changes in the dimensions of the blast tube, agreement between the model predictions and the experimental data for alumina particles is claimed for impingement angles between 20° and 60° with good estimates of the maximum erosion rate; however, the general trend of the model prediction and the experimental data as a function of impingement angle show little resemblance to each other. The

comparison is less encouraging for the fluorite particles
where the predicted maximum erosion rates underestimate the
actual values by a factor of two for the stainless steel and
a factor of four for the aluminum alloy. It is interesting
to note that the fluorite particles with a Moh hardness of
4.0 and higher particle roundness than the alumina were sig-
nificantly more erosive than the alumina particles with a
Moh hardness of 9.0. In the case of 6061-T6 aluminum there
is nearly an order of magnitude difference in the measured
erosion rates for these two particles. The WRAP model predicts
that the erosion rate increases with particle hardness and
roundness. Evidently, there are other factors which must be
taken into account with regard to particle characterization
and testing procedures.

3.4.2 Weight-loss Data

The weight-loss data for oblique impacts
were acquired under conditions which differ from those
reported for sandblast experiments. In the sandblast tests
the velocity of the airstream is held constant and the inclin-
ation of the specimen with the airstream is changed. Under
these conditions the velocity component normal to the surface
of the plate varies as the cosine of the angle between the
normal to the plane face of the specimen and the direction
of the airflow. The experiments conducted in the AFML-Bell
rotating arm facility were designed so that the particle
impact velocity normal to the plane face of the glass speci-
men was held constant. This approach would allow a better
evaluation of the change in the effective erosiveness of the
particles with angle of attack without introducing additional
nonlinear effects associated with a variable impact velocity.
Due to experimental difficulties encountered in obtaining
data in the runs for glass bead impacts, a comparable set of
data is not available for both direct and oblique impacts.
It is found on the basis of the runs which can be compared

that the steady-state erosion rates are the same to within experimental error for the glass beads impacting at an angle of 50° and normal to the plane surface of the specimen. Data are more complete for the 90-micron quartz sand. To within the degree of variability found for the erosion behavior of glass specimens, the steady-state erosion rates can be considered equivalent with the oblique impacts tending to be just slightly more erosive than the direct impacts.

3.4.2.1 Direct Impact by 90-Micron Sand

From the sieve analysis reported in Fig. 2 the average lateral dimension of the quartz sand was found to be roughly 90 microns. The flow rate for the sand particles had to be reduced to 260 g/min. from the 950 g/min. used with the glass beads, since the weight loss for sand was greatly accelerated over that observed for the 70-micron glass beads. The weight-loss data at impact velocities of 200, 300, and 375 fps are provided in Fig. 28 to 30.

In comparing the weight-loss data for the sand particles with that obtained using glass beads, it is necessary to take the different bead flow rates into account. In the present context the number of impacts per revolution recorded in Table V would provide a better basis for comparison. Even after accounting for these differences the experimental conditions, the sand particles are found to be considerably more erosive than the glass beads.

The general character of the weight-loss curves shows that after an initial stage of unsteady erosion rate, due in part to the fact that the weight measurements are only accurate to 1 mg and a probability for measuring errors exists, a uniform rate of material removal is established at each velocity. The values for the uniform erosion rates
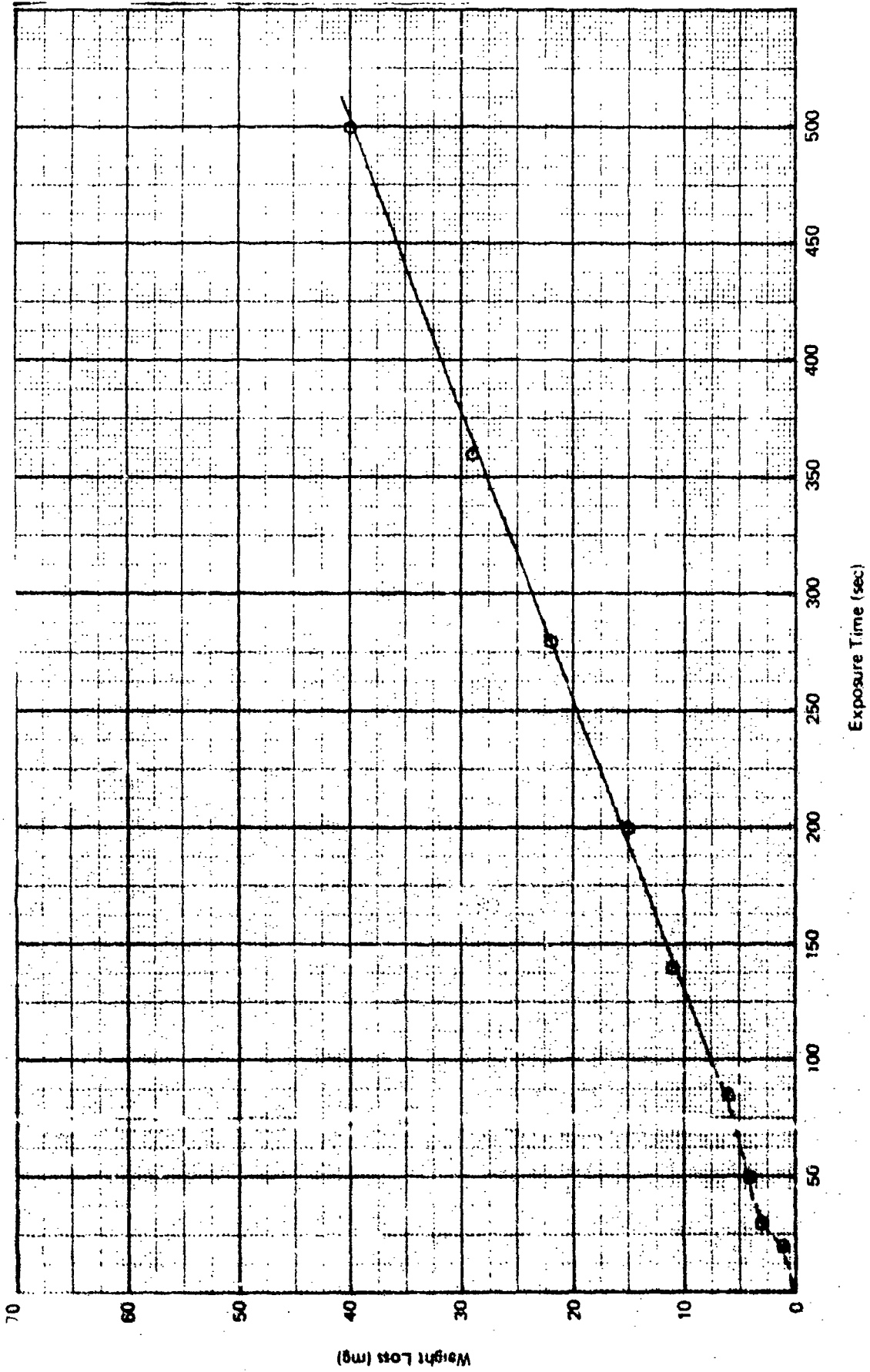
-84-

FIGURE 28 Weight loss for direct impacts of 90-micron sand on glass at 200 fps. (Test PY-40).
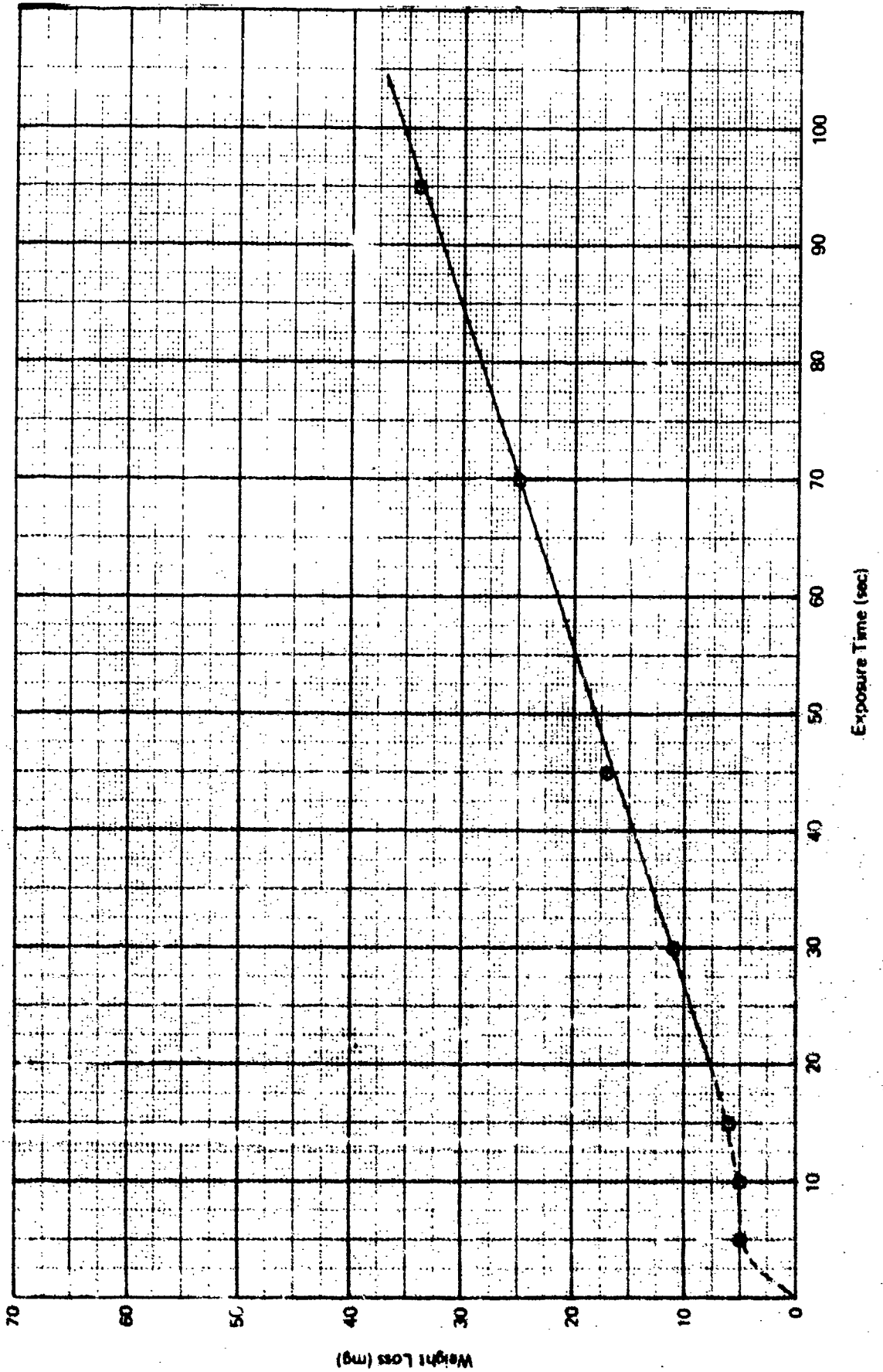
FIGURE 27 Weight loss for direct impacts of 90-micron sand on glass at 300 fps. (Test FY-41)
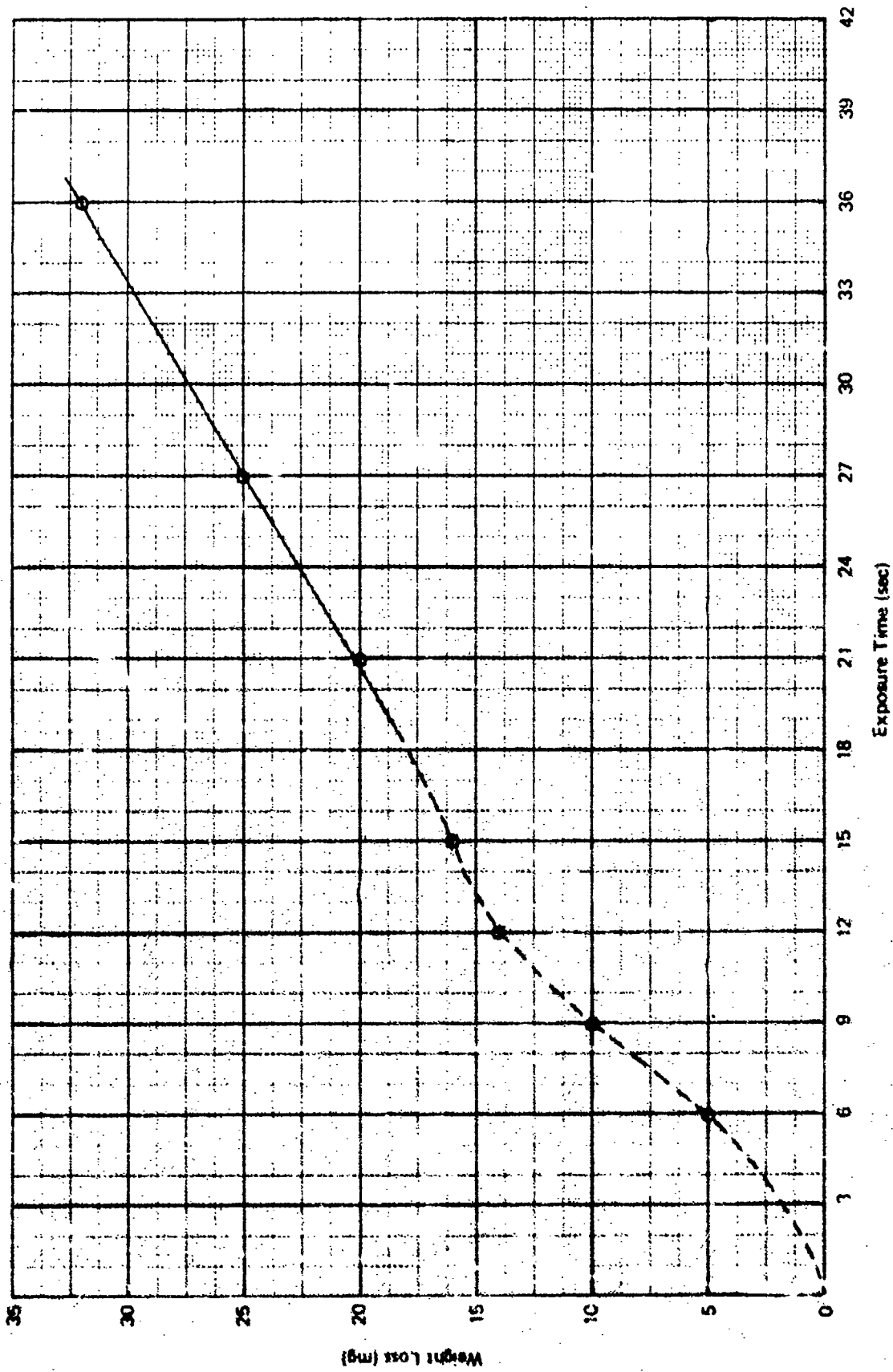
FIGURE 32 Weight loss for direct impacts of 90-micron sand on glass at 375 ips. (Test EY-42)

are plotted as a function of velocity in Fig. 31. The raw
data can be described by the following relation,

$$I_E = (3.35 \times 10^{-10})V^{3.65} \qquad (29)$$

where I_E is the erosion rate expressed in mg/sec and V is the
impact velocity in fps.

3.4.2.2 Oblique Impact by 90-Micron Sand

The sand flow rate was maintained at the
same rate that was used for the direct impacts which was
260 g/min. Microscopic examination of the eroded surfaces did
not reveal any differences between the damage due to oblique
impacts and that associated with direct impacts.

The weight-loss data at normal impact
velocities of 200, 300 and 375 fps are shown in Fig. 32 to
34. After a relatively brief initial period of unsteady mate-
rial removal a steady rate of material removal is established.
The steady-state erosion rates at each velocity are recorded
in Table IX. The data at 300 fps appears to be somewhat
anomalous, however the data at the other two velocities are
consistent indicating that the erosion rates are slightly
higher for oblique impacts at an angle of attack of 50° to
the surface of the specimens than direct impacts when the
normal impact velocity is held constant.

3.4.3 Microscopic Examination

Microscopic examination of specimens PY-43
to 46 and PY-53 to 55 for the direct and oblique impact of
the 90-micron sand particles under the conditions listed in
Table I indicated that there was very little difference in
the form of the erosion damage in each case. A series of
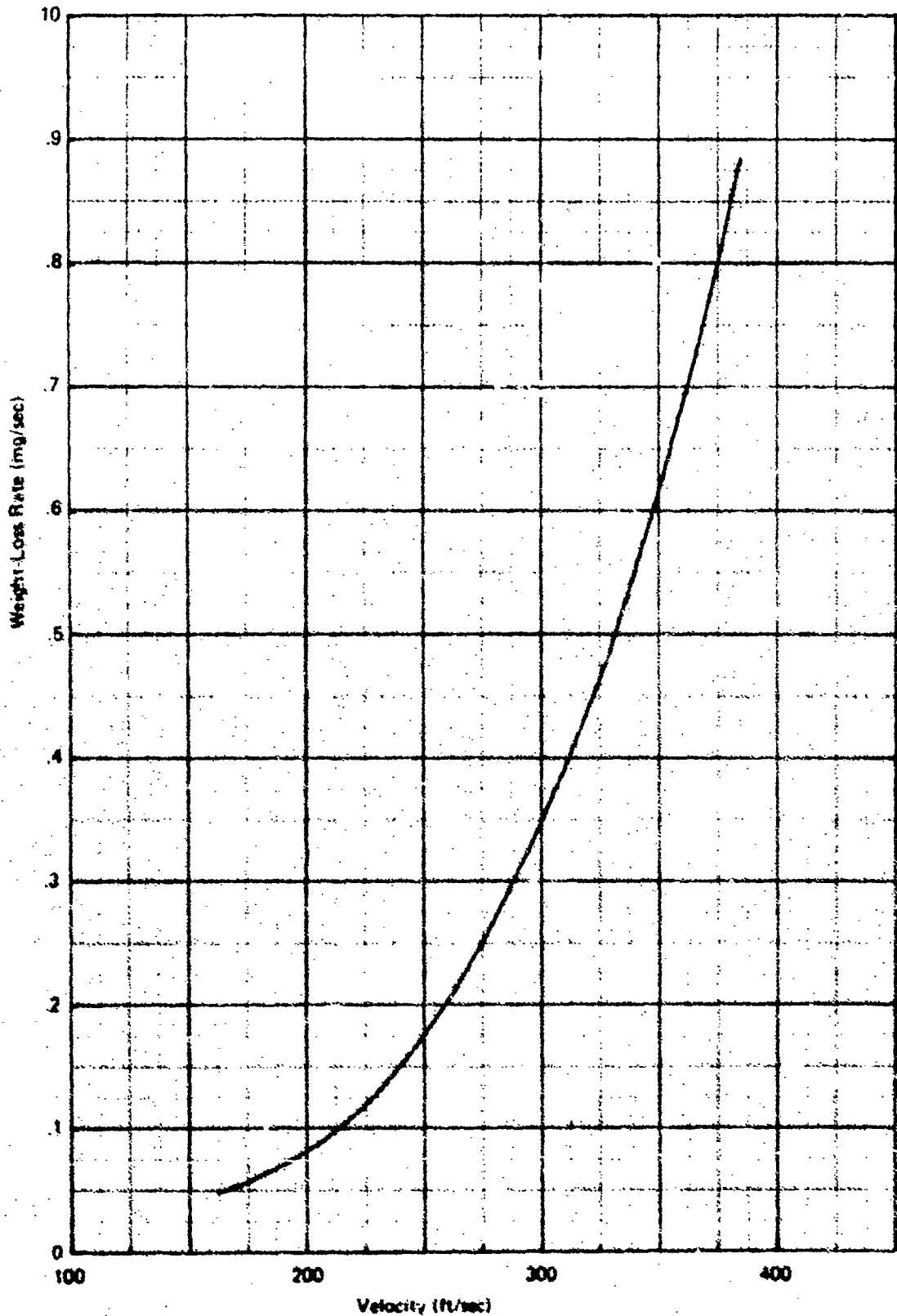
FIGURE 31   Steady rate of weight loss as a function of
             impact velocity for direct impacts of
             90-micron sand on glass.
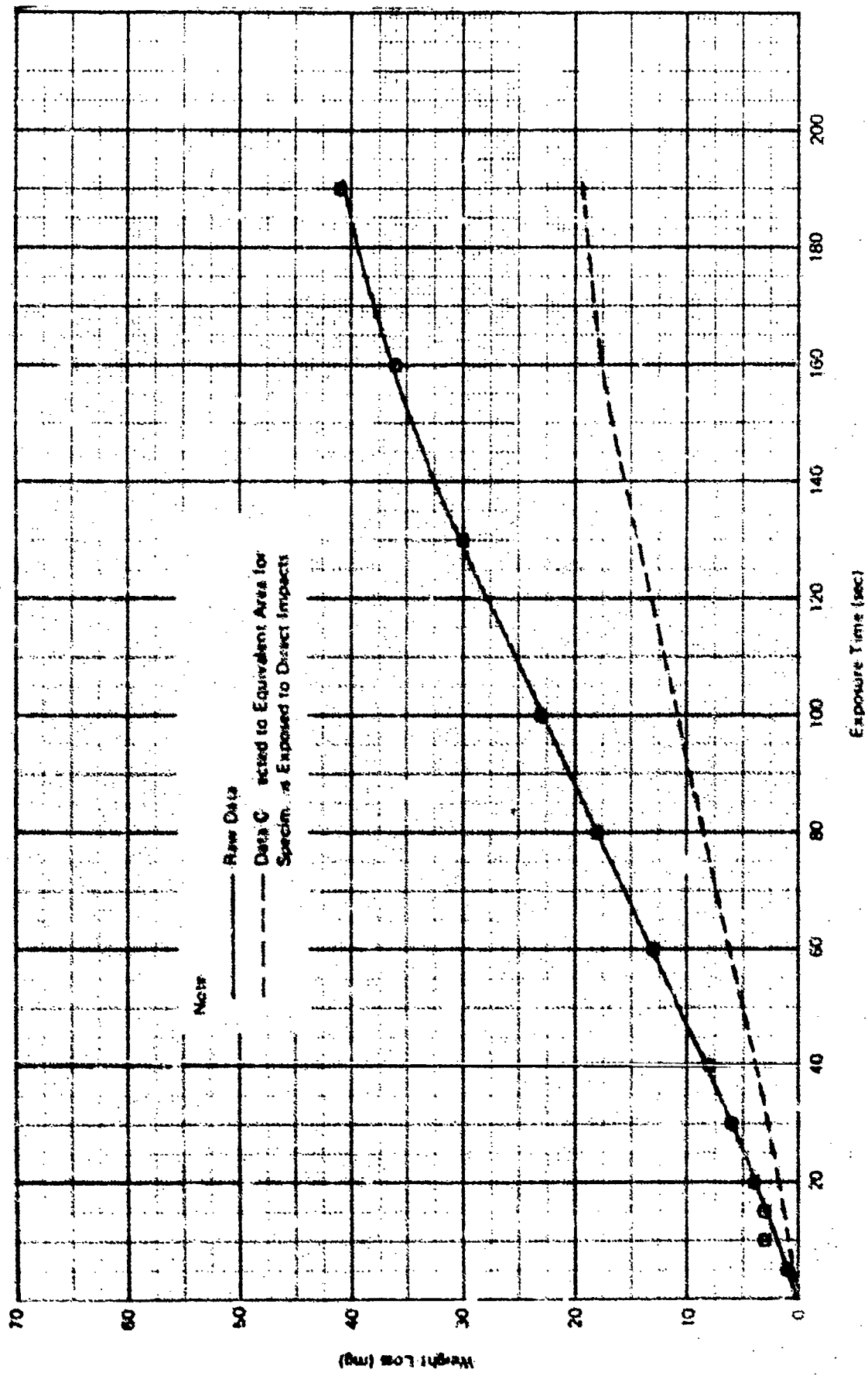
Figure 38. Weight loss for oblique impacts of 30-micron sand or glass at a normal velocity of 80 fps. (Test IV-50)
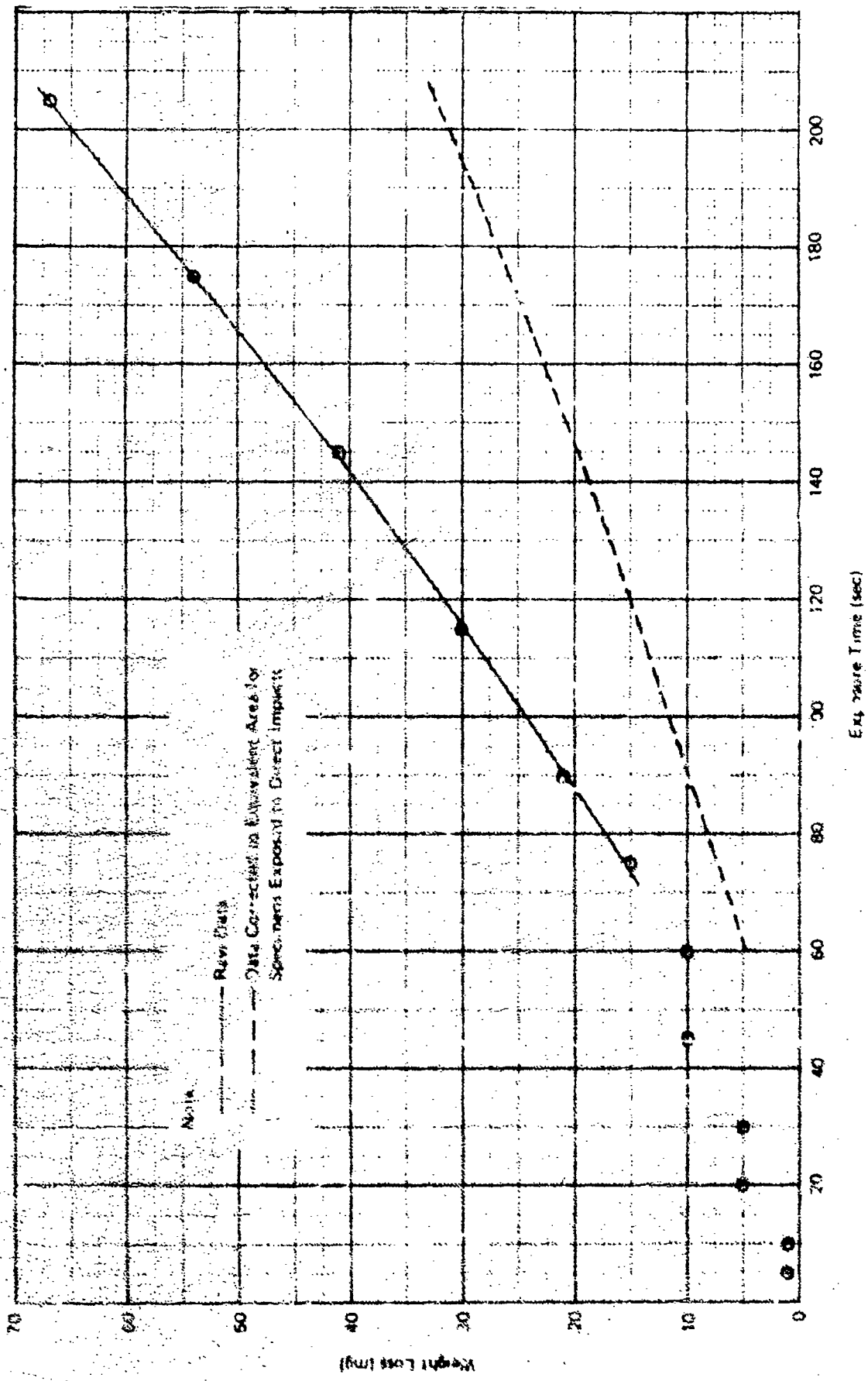
Figure 23 Weight loss for oblique impacts of 90-micron sand on glass at a normal velocity of 300 fps. (Test FY-51)
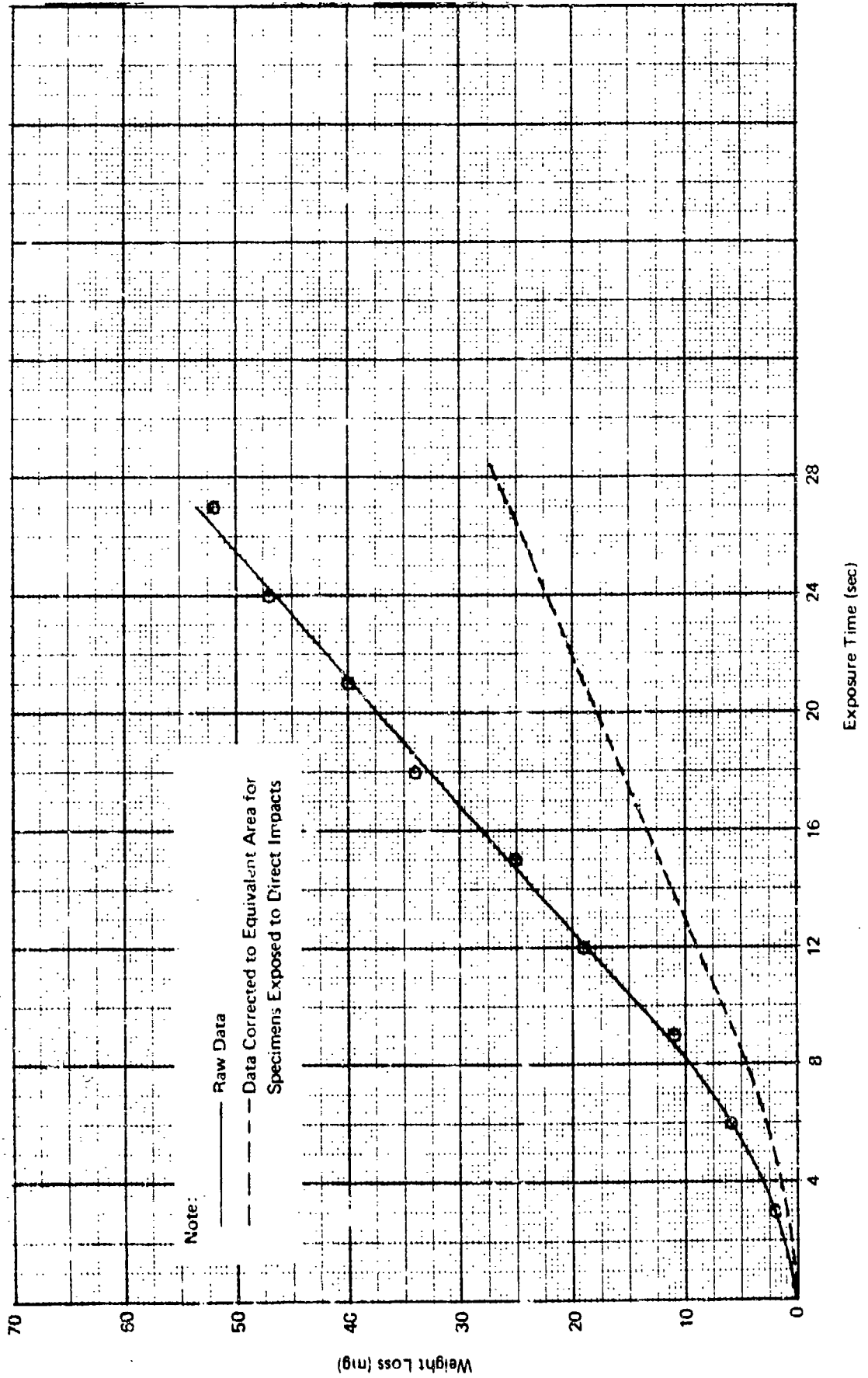
FIGURE 34   Weight loss for oblique impacts of 90-micron sand on glass at a normal velocity of 375 fps. (Test PY-52)

-92-

TABLE IX

STEADY RATE OF MATERIAL REMOVAL FROM GLASS
SPECIMENS FOR DIRECT AND OBLIQUE IMPACT OF
90-MICRON SAND AT VARIOUS PARTICLE IMPACT VELOCITIES

Normal Impact Velocity (fps)	Erosion Rate (mg/sec/unit area)	
	Impact Angle 0°	Impact Angle 50°
200	0.100	0.105
300	0.425	0.224
375	1.00	1.26

micrographs is provided in Fig. 35 and 36 which shows representative damage areas on the surface of each specimen and comparisons between equivalent impact conditions for direct and oblique impacts. These areas were selected in a random manner, however a qualitative evaluation of the resulting damage in each instance shows minor differences in the impact indentations for direct and oblique impacts. The impacts at 375 fps are the most damaging, and this effect appears in the larger indentations which are formed at this velocity. Quantitative evaluation of the damage is required in the modeling studies in terms of specific characteristics of the particle indentation: the distribution of size, shape and penetration as a function of impact velocity and exposure time. This effort parallels that of characterizing the sand particles comprising the erosive medium and will be investigated in the near future.

The progression of damage on the eroded surface of specimen PY-50 can be seen over a limited range of the exposure time in Fig. 37. The same area is monitored for each time increment. Once a localized pit develops it does tend to grow; however the nucleation rate is high for the sand particles, so numerous additional pits will be formed in the vicinity of the first one before it has grown appreciably. However, there is still abundant evidence that pit growth is preferential.

3.5 Liquid Droplet Impacts

A number of mathematical analyses applicable to the quantitative evaluation of the transient stress conditions which prevail within a material body when it is impacted by a spherical liquid drop are considered in this section. While the complete mathematical problem for a drop striking a deformable material surface at moderate velocities is beyond
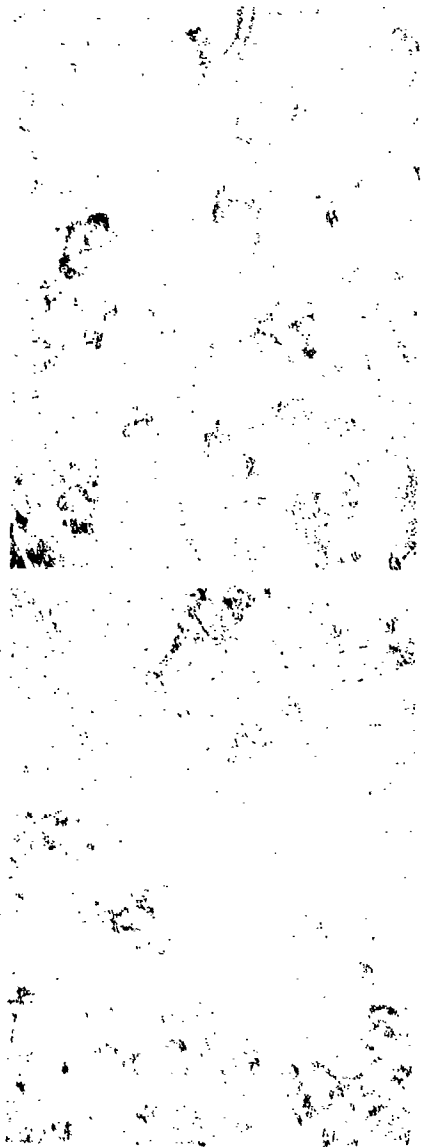
(a) Direct Impact at 200 fps for 5 sec. Exposure Time   (b) Direct Impact at 300 fps for 2 sec. Exposure Time   (c) Direct Impact at 375 fps for 1 sec. Exposure Time

(d) Oblique Impact at 200 fps for 5 sec. Exposure Time   (e) Oblique Impact at 300 fps for 2 sec. Exposure Time   (f) Oblique Impact at 375 fps for 1 sec. Exposure Time

Figure 35   Typical pit configuration on glass specimens impacted by 90-micron sand (320X)

(a) Direct Impact at 200 fps for 5 sec. Exposure Time

(b) Direct Impact at 300 fps for 2 sec. Exposure Time

(c) Direct Impact at 375 fps for 1 sec. Exposure Time

(d) Oblique Impact at 200 fps for 5 sec. Exposure Time

(e) Oblique Impact at 300 fps for 2 sec. Exposure Time

(f) Oblique Impact at 375 fps for 1 sec. Exposure Time

Figure 36 Comparative erosion damage on glass specimens impacted
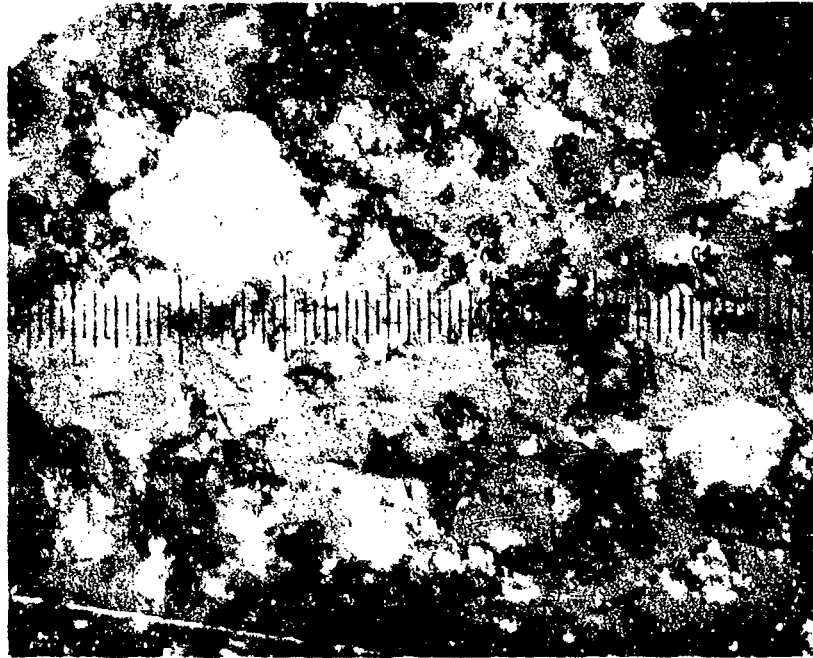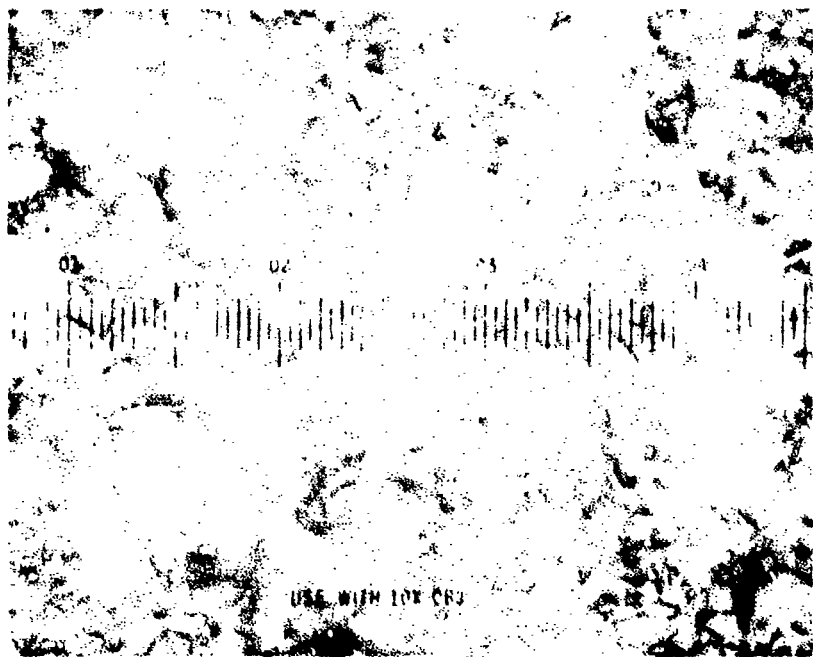by 90-micron sand (110X)

a. 15 sec.

b. 30 sec.

Figure 27   Progression of pitting on glass specimens
due to oblique impacts by 90-micron sand
at a normal impact velocity of 200 fps
(44X)

the existing state-of-the-art, a number of reasonable approximations to the general problem are presented here. Only a limited amount of numerical results are provided due to the complex nature of the mathematical solutions which are available. This research is only an interim report on the advances in computer modeling which offer considerable potential for evaluation and development of material systems with greatly enhanced erosion resistance. The required computer codes will be compiled and developed further to achieve this objective in future work on this program.

The erosion damage mechanism has to be established for different types of material response. For brittle materials the magnitude and duration of the critical radial surface stress component may be the most important factor. In a ductile material the critical shear stress trajectories would be more significant. The availability of data on transient stress distributions within the interior of the solid body provides a means for quantitative evaluation of the critical conditions under which failure of a particular material system is likely to occur and to evaluate the erosion resistance potential for materials from computer modeling studies.

Table I lists the tests conducted on glass specimens exposed to a standard rainfall of 1 in/hr. of 1.8 mm drops on the AFML-Bell rotating arm. Although the glass specimens impacted by glass beads could sustain velocities around 500 fps without fracturing, this was not the case in the rain erosion tests. It was found that rain erosion damage on glass was inconsequential below 400 fps. In order to relieve the stress applied to the specimen in the specimen holder at the end of the rotating arm at velocities above 400 fps, the glass specimen was shortened and the specimen then bonded to an aluminum backing plate to reduce problems with fracturing of the ends of the glass specimens. This arrangement was

adequate to achieve the velocities required to produce erosion damage by water particle impacts on the glass specimens but not for the exposure times required for the acquisition of weight-loss data.

The number of impacts that the specimen receives in the rain fields produced in the AFML-Bell erosion facility can be calculated in a manner similar to that developed for solid particle impacts. The rainfield is constant over the complete area described by the specimen in one revolution. This area is

$$A = \pi (r_2^2 - r_1^2) \qquad (30)$$

where $r_1 \approx 108$ in., $r_2 \approx 111$ in., are the distances from the center of rotation to the inboard and outboard ends of the specimen on the rotating arm. The number of drops per hour, N, is given by

$$N = \frac{jA}{\frac{4}{3}\pi r^3} \qquad (31)$$

where j is the magnitude of the rainfield in in./hr. and r is the radius of a raindrop. According to Eq.(22) (Reference 1) the density of a given flow rate of particles in a gravitational field at a distance below the point from which they were released with zero initial velocity is

$$\rho(X) = \frac{N}{43,200} \frac{1}{\sqrt{2gX}\, A} \qquad (32)$$

where $g = 32.2$ ft./sec.^{2} and X is measured in feet. The plane of the rotating specimen in the erosion facility is about 6 ft. below the apex of the trajectory of the spray of fluid droplets. To obtain the number of droplets the specimen encounters per revolution, the density from Eq.(32) is multiplied by the volume the specimen passes through per revolution.

$$N_I = \frac{Nd}{43,200\sqrt{2gx}} = \frac{j(r_2^2 - r_1^2)d}{57,600r^3\sqrt{2gx}} \qquad (33)$$

where d is the height of the exposed area of the specimen's surface in inches.

For the aerodynamically-shaped specimens usually employed in erosion tests on the rotating arm and exposed to 1 in./hr. rainfall of 1.8 mm drops, d = 0.5 in., so

$$N_I = 6.5 \text{ impacts/revolution}$$

The flat-faced glass specimens exposed to the same rainfall encounter 9.75 drops/revolution. These estimates of the impacts the specimen receives will be used in evaluating the erosion behavior of the materials investigated in this program.

3.5.1 Mechanics of Liquid Drop Collisions With Deformable Surfaces

The damage produced on solid surfaces due to liquid particle impingement arises from two sources: the high pressure which is generated over the expanding impact area in order to bring the drop to a sudden stop and the high-velocity lateral flow of the liquid subsequently escaping from the high-pressure zone. Detailed knowledge of the flow patterns and impact pressures developed during the collision of a liquid drop and a deformable plane surface is still unavailable. In this case the governing field equations and boundary conditions are coupled and pose a very difficult mathematical problem. While it is a formidable task to solve the coupled mathematical problem, approximations to the general physical conditions can be made. These alternative approaches fall into three major categories:

Evaluation of the magnitude of the pressure
developed at the interface between the drop
and the solid surface using a one-dimensional
shock wave analysis which accounts for the
compressibility of both the liquid and the
solid.

Evaluation of the pressures and deformations
associated with the drop assuming the solid
surface is rigid.

Evaluation of the stresses and deformations
within the solid after prescribing a pres-
sure distribution which is assumed repre-
sentative of that developed at the interface
between the drop and the surface of the
solid at some stage of the collision process.

A number of high-speed photographic studies[4,19-23]
provide qualitative insight into the phenomena associated with
the single impact of a liquid droplet on a deformable surface.
Liquid jets striking a solid surface at 2400 fps exhibited a
rise time of 1μs for the peak pressure to be obtained which
then decayed to a much lower value within 2 to 3μs which is
the time it took release waves to propagate into the interior
of the jet.[20] The jet continues to impact the surface for
another 20μs, however the liquid/solid interfacial pressure is
at a greatly reduced level assumed to be equal to the stagna-
tion pressure along the axis of symmetry. The experimental data
on spherical drops striking a solid surface still cannot pro-
vide a quantitative picture of the temporal magnitude and dis-
tribution of the liquid/solid interfacial pressure.

Detailed analytical studies have only been
provided for the pressure distribution due to a liquid drop
striking smooth, rigid surfaces.[24-30] Huang[29] in parti-
cular has presented the most complete mechanics analysis with

computer solutions to indicate that time-evolution of the impact pressures and lateral outflow at impact velocities of 980 and 2450 fps. Huang's calculations support Engel's contention[24] that the pressure buildup and lateral outflow occur simultaneously after the initial contact is made, although the jetting is not appreciable during the early stage of impact. This contradicts the more widely held opinion of Morris[28], Heymann[27], and Bowden and Field[4] that lateral flow cannot begin before the compression wave in the fluid moves ahead of the circular boundary between the drop and the solid surface. At approximately 300 fps, these calculations indicate that the critical edge angle is on the order of a few degrees. Brunton and Camus[23], however, provide photographic evidence that under these conditions the critical angle falls in the range of from 13° to 19°, or the radius of the contact area at this point is from 0.23 to 0.33 times the radius of the drop. These results are consistent with the time-dependent drop configurations computed by Huang and supported by the computer analysis of Tyler[31].

Huang's results[29-30] also indicate that the ratio of the lateral jetting velocity to the impact velocity decreases as the impact velocity increases. This same effect is evident in the photographic study of Jenkins and Booker[19] where 2 to 2-1/2-mm drops were impacted on a steel surface over a velocity range of 300 to 3750 fps. A plot of lateral velocity as a function of the impact velocity shows that the ratio of the velocity of lateral outflow to the velocity of impact is approximately 6 at an impact velocity of 300 fps while it is only 2.4 at 2500 fps. Fyall's[22] measurement of radial outflow for a 2 mm drop striking a plate of polymethylmethacrylate at approximately 1000 fps resulted in roughly the same ratio between the radial outflow and the normal impact velocity as found by Jenkins and Booker.

Brunton and Camus[23] have also provided photographic evidence of cavitation bubbles within an impacting drop. Cavitation bubbles were found at the liquid/solid interface during the early stage of impact due to a negative pressure which results from the expansion of the compressed liquid when sideways flow begins. Brunton and Camus explain that the expanding liquid overshoots and a negative pressure forms at the surface propagating into the liquid as a tension tail to the main compression wave. Cavitation bubbles were also found to form near the rear face of the impacting drop due to the reflection of the impact pressure wave from the rear surface of the drop. The occurrence of cavitation bubbles in this region was originally suggested by Engel[24] and subsequently supported by the numerical calculations of Huang[?]. On the other hand, the photographic studies conducted by Pyall[?] for a 2 mm water drop impacting a plate of polymethyl methacrylate at 900 fps did not exhibit this effect. Pyall hypothesized that the pressure wave may be attenuated within the drop.

Thus, Huang's calculations compare favorably with the available photographic studies of raindrop collisions. In general we are inclined to believe that Huang's analysis is a reasonably accurate representation of the dynamics of a raindrop striking a rigid surface. The pressure distributions which he provides as a function of time and spatial coordinates will be used in the analyses we would like to develop.

Very little unanimity can be found in the literature concerning the nature of the pressure distribution which develops at a solid surface impacted by a liquid droplet. The magnitude of the pressure pulse transmitted to a deformable material by a liquid drop has been evaluated in terms of the acoustic impedance of the liquid and the solid material.

$$p = \frac{\rho_0 C_0 V_0}{1 + (\rho_0 C_0 / \rho_1 C_1)}$$

(34)

where ρ_0 and ρ_1 are the respective densities of the liquid
and the solid and C_0 and C_1 are the acoustic velocities in
the liquid and solid, respectively. V_0 is the impact velocity
of the liquid droplet. This approach assumes that a uniform
pressure is impulsively applied over the entire plane surface
of a semi-infinite half-space. It is found that the local
impact pressures in raindrop impacts at moderate velocities
are of a magnitude that the liquid is compressed before lateral
outflow is initiated. The velocity of sound, C, will be
increased due to the change in density. Elementary shock wave
theory was employed by Morris[28] to estimate the magnitude
of the initial pressure transmitted to a solid under these
conditions.

Huang's numerical approach devised for
obtaining quantitative estimates for the pressure distribution
associated with a compressible liquid drop striking a rigid
surface indicates that a hemispherical pressure distribution
predominates during the very early stages of the collision.
The maximum value of the pressure is reached under these con-
ditions. As compression of the drop continues, the distribu-
tion becomes more uniform with a very slight increase
in the magnitude of the pressure at the periphery of the con-
tact area. The magnitude of the maximum value in the pressure
distribution decreases as lateral outflow becomes more
dominant.

Considering impact velocities which are less
than 1000 fps, it is found that Heyman's analysis[27] predicts a
maximum pressure of approximately 3 $\rho_0 C_0 V_0$, while Huang's
numerical results[29] indicate that the maximum pressure does not
exceed 0.8 $\rho_0 C_0 V_0$. These estimates have been obtained for a
rigid surface and therefore represent the maximum values that
are likely to occur. As the pressure increases on a deformable

surface, the localized contact zone will be depressed; hence, the relative velocity of approach of the liquid is less than what it would be for a rigid surface.

Blowers[32] investigated the propagation of stress waves in an elastic half-space subjected to a uniform pressure P distributed over an expanding circular region on its surface whose time-dependent radius is deduced from the idealized model of a compressible drop striking a rigid surface depicted in Fig. 36. If the impact velocity is V_o, then the radius of the contact area, $a(t)$, increases with time according to the relation

$$a(t) = \sqrt{2RV_o t - (V_o t)^2} \tag{35}$$

where R is the radius of the spherical drop. The radial velocity of the expanding contact area is

$$\dot{a}(t) = \frac{(R-V_c t)V_o}{\sqrt{2RV_o t - (V_o t)^2}} \tag{36}$$

For small values of t compared to the duration of the impact

$$a(t) = \sqrt{2RV_o} t^{\frac{1}{2}} = kt^{\frac{1}{2}} \tag{37}$$

The pressure distribution on the surface of the solid (z=0) adopted by Blowers in his analysis is of the form

$$P(r,t) = P \quad \text{for} \quad r \leq kt^{\frac{1}{2}}$$
$$= 0 \quad \text{for} \quad r > kt^{\frac{1}{2}} \tag{38}$$

The magnitude of P has to be prescribed and is taken to be a known quantity.

The velocity of the expanding circular boundary is initially supersonic but decreases as $t^{-\frac{1}{2}}$. The disturbance
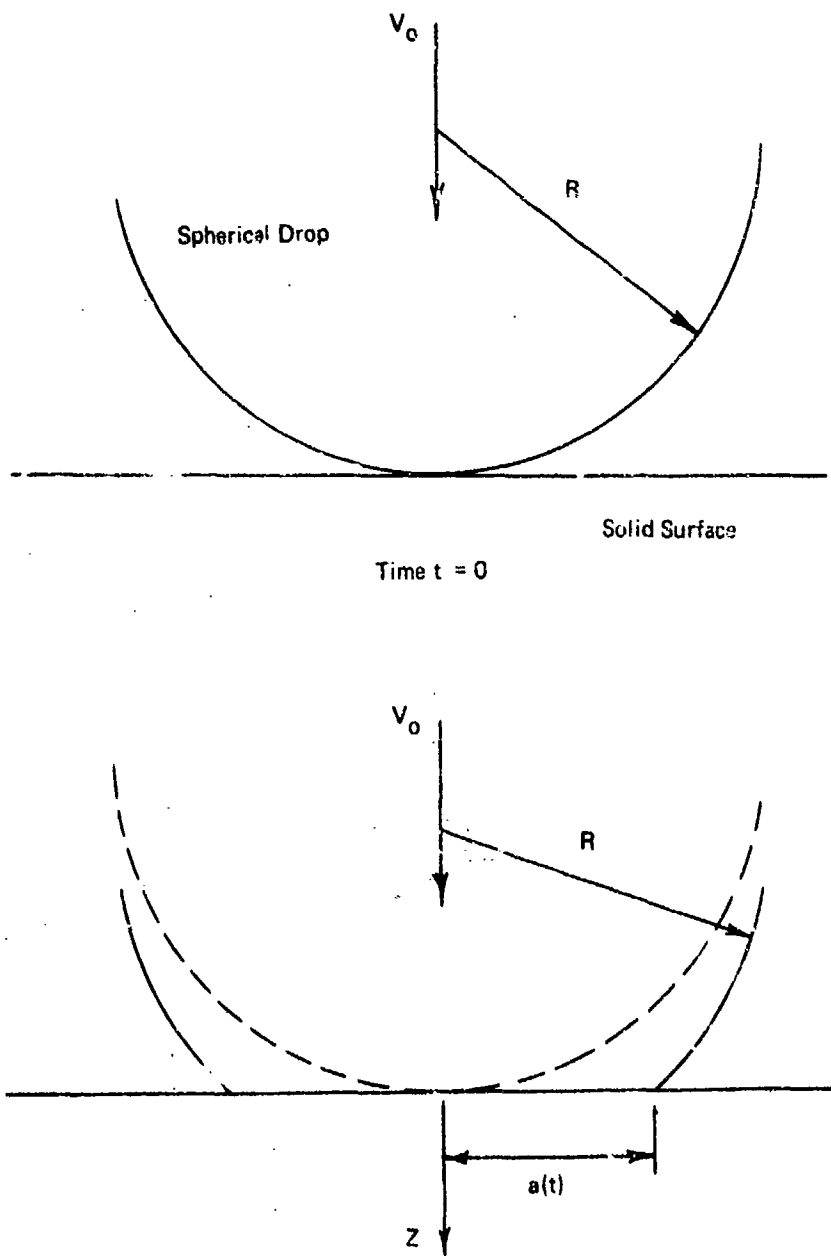
Figure 38. Idealized Model for Evaluation of Time-dependent Radius of Expanding Contact Area for a Spherical Drop Striking a Solid Surface

experienced by the solid medium will then be due to the propagation of a dilatation wave traveling at a velocity c_1, the propagation of a distortional, or shear, wave traveling at a velocity c_2, and a Rayleigh wave propagating along the surface at a velocity c_R which is slightly less than c_2.

$$c_1 = \sqrt{\frac{E(1-\nu)}{\rho(1+\nu)(1-2\nu)}} \qquad (39)$$

$$c_2 = \sqrt{\frac{E}{2\rho(1+\nu)}}$$

where E is Young's modulus, ν is Poisson's ratio, and ρ is the density of the medium.

As long as the boundary of the loaded region is moving at a velocity $\dot{a}(t) \geq c_1$ the radius of the disturbance will be the same as that of the loaded area. When $\dot{a}(t) < c_1$, the disturbance will move ahead of the load and will continue to travel at the sonic velocity of the medium. The time at which $\dot{a}(t) = c_1$ can be determined from Eq.(37).

$$\tau_1 = \left(\frac{k}{2c_1}\right)^2 \qquad (40)$$

For times greater than τ_1. Blowers displayed the solutions for the development of the dilatational, distortional, and Rayleigh waves as they propagate ahead of the loaded area along the plane surface of the elastic half-space. Limited numerical results are provided for the case when $(c_2/c_1)^2 = 2/7$ or $\nu = 0.3$. This value of Poisson's ratio is approximately equal to that of steel for which $c_1 = 19,500$ fps. Blowers shows that the transient radial and azimuthal surface stresses at time $t = 8\tau_1$ are primarily compressive with extremely high tensile stresses found only in a narrow band immediately behind the Rayleigh wave front. Blowers comments that although extreme radial tensions arise, the extent of the radial dimensions in which they occur is always quite small. Thus each

-107-

point experiences the critical tension for an extremely short duration. Blowers conjectures that this result of the analysis tends to raise doubt in the effectiveness of the Rayleigh wave as the cause of liquid impact erosion damage.

Blowers' analysis assumes that the magnitude of the applied pressure is constant over an expanding circular area. In actuality the magnitude of the maximum value in the pressure distribution and the form of the distribution is changing with time. As indicated earlier a fluid mechanics analysis of a spherical drop striking a rigid surface has been provided by Huang[29] using a numerical scheme. The results from these computations agree favorably with the existing experimental data. The pressure distributions at the liquid-solid interface, the isobaric distribution within the drop, and the radial velocity of the contact zone have been computed as a function of a non-dimensional time unit and the spatial coordinates. Computed results are available in Huang's thesis[29] for a 2mm water drop impacting at 980 fps. Under these conditions one dimensionless time unit, $T_H = 1$, is equal to $1 \mu s$. For these impact conditions and taking the solid medium to be steel in conformance with Blowers computations, Eq. (40) yields

$$\tau_1 = 4.24 \times 10^{-9} \text{ sec.}$$

for $k = 2.54 \text{ ft/(sec)}^{\frac{1}{2}}$

The time-dependent radius of the loaded area computed by Huang for the non-slip boundary condition agrees exactly with the radius obtained from the simple model used by Blowers and given by the relation in Eq. (37). The radii corresponding to the full-slip boundary condition also employed by Huang differ by less than a few percent from the values based on the simple model. This agreement is found to hold for values of the contact area radius approaching the radius of the drop.

The computer models of a compressible liquid drop striking a rigid surface provide a reasonably accurate approximation to the pressure distribution applied to a rigid surface, while Blowers' results provide a quantitative evaluation of the transient stress distribution within an elastic solid subjected to a known uniform pressure distribution. Although the exact conditions prevailing at the interface between the drop and deformable solid cannot be analyzed directly, the two approaches above can be combined in a way which provides at least a reasonable approximation to the coupled problem. For extremely low impact velocities the pressure distributions obtained from the droplet models can be used directly to ascertain the response of the solid medium. However, at impact velocities which are sufficient to compress the solid by a significant amount, an elementary shock wave analysis of the interfacial region can be employed to estimate the magnitude of the pressure transmitted to the solid.

In reviewing Huang's results it is seen that the pressure distribution is hemispherical up to the point at which the maximum pressure is reached and then it assumes a more uniform distribution as the magnitude of the pressure subsides with the onset of substantial lateral outflow. In order to employ Blowers' analysis, the applied pressure distribution during both periods will be assumed to be uniform and have a magnitude equal to the average value of the actual distribution. The fluid particle velocities corresponding to this pressure can be determined from the Hugoniot relation for water at each instant of time. The procedure is illustrated in Fig. 39. A family of curves, reflection Hugoniots for water, are generated and plotted as shown in Fig. 39(b) with time as a parameter. This approach allows the pressure pulse to have a finite rise time in conformity with the two-dimensional analysis for a spherical drop. The conditions prevailing at the interface between the drop and the solid
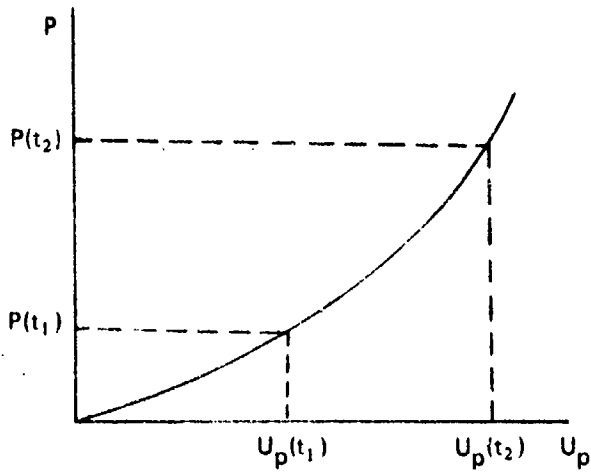
(a) Hugoniot for Water
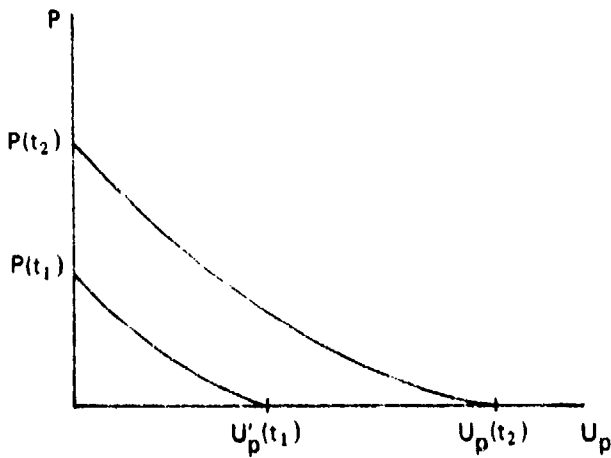
(b) Time-dependent Reflection Hugoniots for Water with Average Time-dependent Pressures Computed from Huang's Analysis
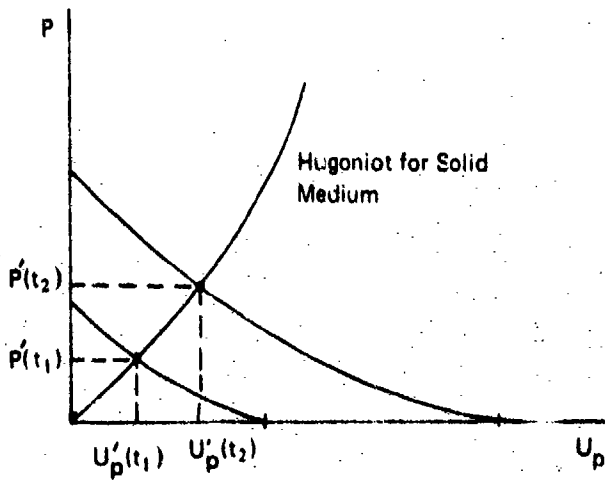
(c) Time-dependent Pressure Applied to Solid Surface Corresponds to Intersection Points between Hugoniot for the Solid and the Reflection Hugonicts for Water

Figure 39. Evaluation of Pressure Transmitted to a Solid Medium by Liquid Droplet Impacts

medium are approximated by plotting the pressure-particle velocity relations for the impacted solid on Fig. 39(b) as shown in Fig. 39(c). Assuming the pressure and particle velocities are continuous across the interface, the points of interaction of the reflection Hugoniots for water and the Hugoniot for the solid provide the instantaneous magnitude of the pressure applied to the solid surface accounting for the compressibility of the solid medium.

A fair approximation to the spatial- and time-dependence of the localized pressure imparted to a deformable solid by a spherical liquid drop impacting at low to moderate velocities has now been achieved. The magnitude of the pressure distribution can be used with Blowers' analysis to evaluate the transient stresses which arise in response to the disturbances propagating into the interior of an elastic half-space. As the magnitude of the pressure increases it is possible that finite amplitude waves will propagate into the solid medium.[33-35]

Recently, Peterson[36] advocated the reduction of the transient liquid droplet problem to a quasistatic analysis based on the Hertzian theory of impact in order to evaluate the response of the target material. On the basis of Huang's computer analyses, he assumed a hemispherical distribution of pressure as representative of the loading conditions during the period of pressure build-up. Peterson's approach would be valid if it could be established that the quasistatic stress states are attained quite rapidly after the passage of the Rayleigh surface waves.

Once again we refer to the published results of Blowers applicable to a uniform load applied to an expanding contact area representative of a spherical droplet collision. For a very short time interval after the Rayleigh wave propagates ahead of the moving periphery of the loaded area,

both the radial and circumferential stress components are tensile and of unequal magnitude in the region between the Rayleigh wave front and the boundary of the contact area on the surface of the half space. The static solution for a uniform load acting over a circular region on the surface of an elastic half-space shows that the magnitude of the radial stress and circumferential stress components are equal but the circumferential stress is compressive while the radial stress is tensile in the region exterior to the loaded area.[37] In principle it is possible to evaluate the form of the stress components at larger time intervals using Blowers' results, however access to his computer program has not been established at the present time. The validity of Peterson's hypothesis that the static stress distributions can be used after the passage of the Rayleigh wave to estimate the response of the target materials to droplet impacts can therefore be tested directly. Both Blowers[32] and Eason[38] point out that the static values of the displacements are approached quite rapidly along the axis of symmetry of the loaded area.

A significant amount of additional work is required to obtain an operational computer code which will provide meaningful quantitative results. However, such a program would properly delineate the conditions under which a static analysis is acceptable and those for which a transient stress wave problem must be considered. The three-dimensional elastic analysis also provides more accurate evaluations of the magnitude of the stress components within the solid medium than the elementary one-dimensional approaches that have been prevalent in erosion studies. Having more accurate approximations to the maximum stress state the solid must endure and their duration will lead more effectively to the development of realistic connections with a material's mechanical and physical properties, fracture behavior and microstructure.

3.5.2 Experimental Erosion Data

When the same specimen holder used for the solid particle impacts was used in the rain erosion tests without additional modification, the glass specimens exhibited a strong tendency for cracking in the early stage of each test. A number of changes were made, however only a limited amount of experimental data pertaining to liquid drop impacts were obtained within the present program. In subsequent testing smaller specimens will be employed set in a thick polyurethane support which is inserted into the existing specimen holder at the end of the rotating arm. No weight-loss data were obtained, since the specimen fractured before more than a few weight measurements could be made.

The cumulative damage on the surface of specimen PY-1 was negligible after an exposure time of 40 min. An occasional microscopic crack could be found on the surface, but it appears that the impact velocity of 300 fps is not sufficient to produce extensive surface cracking. The fine cracks which did appear did not show any particular characteristic which could be related to the pressure distribution generally assumed to be associated with water droplet collisions. A small number of flaws must be present on the surface which are of sufficient size to extend to low-power microscopically observable cracks at th pressures developed by a drop impacting at 300 fps.

Specimen PY-2 showed a sparse distribution of microscopically visible cracks penetrating the interior of the specimen. There was some tendency toward a concentric ring configuration with at least a portion of the cracks centered around an identifiable origin. The slope of the fracture surfaces extending into the specimen provided some idea of the direction of the transient stress pulses generated by droplet collisions. Closed curves where the internal

crack intersects the surface were found on the surfaces of specimens PY-2, PY-3 and PY-5. The curves were quite irregular and did not have the circular form observed by Bowden and Field[4] for jets striking glass surfaces at considerably higher impact velocities. The lateral dimensions of the closed regions ranged from a few mils up to 13 mils. Some areas did show a slight tendency toward concentric ring formation within pie-shaped regions with an included angle in the range of 45 to 60 degrees. Several cracked regions on specimen PY-3 originated at semi-circular cracks with radii around 2 to 6 mils. The cracks penetrated 60 to 80 microns into the bulk material. It is estimated that the fracture surfaces are inclined at angles from 29 to 38 degrees to the surface of the specimen.

The majority of the subsurface fractures had a characteristic form. The fracture surface extending from the surface of the specimen into the bulk material was very smooth for a short distance below the surface and then exhibited a hackled appearance for the remainder of its extent.

Fine-scale chipping initiates through the intersection of the random crack formations on the surface. Specimen PY-5 gave some indication of the longer-term erosion behavior. Four large pits which were 0.1 to 0.2 in. wide were present on the surface before the specimen fractured. At 500 fps the material removal mechanisms are quite preferential and the erosion process conforms to the fundamental hypothesis of the erosion model.

4.0 GENERAL EROSION MECHANISMS

Table X lists the erosion tests conducted on ultra-high molecular-weight polyethylene, a nickel-coated epoxy composite and a graphite-fiber reinforced epoxy. The specimens were exposed to a standard rainfield of 1 in/hr of 1.8 mm drops in the AFML-Bell erosion facility. The 90-micron sand described in Section 3.1 was used for the solid particle erosive mdeium. In all of the tests the flow rate was 260 g/min.

## 4.1 Erosion of Ultra-High Molecular-Weight Polyethylene

A series of flat-faced and standard aerodynamically-shaped polyethylene specimens were subjected to the standard rainfield (1 in/hr. of 1.8 mm droplets) and the 90-micron sand characterized in Fig. 2 and 3. The ultra-high molecular weight (UHMW) polyethylene is Hostalgen GUR supplied by the American Hoechst Corporation. The flat-faced polyethylene specimens were rectangular parallelepipeds 3.25 in. x 0.5 in.

The magnitude of the eroding area is different on the surface of each specimen configuration. The eroding area for the flat-faced specimens is 2.25 sq. in. (3.0 in. x 0.75 in.) and for the aerodynamic shape it is 1.25 sq. in. However there is an angular effect due to the curvature of the aerodynamic shape which makes a direct comparison between each specimen configuration somewhat difficult. The flat-faced specimens were used in an attempt to eliminate the influence of this curvature on the erosion rates and to facilitate the microscopic examination of the erosion damage.

The surfaces of the polyethylene specimens were polished before testing. The condition of the initial surfaces before testing is shown in Fig. 40. A point was reached in the polishing operation beyond which additional polishing of the surface did not produce any refinement in the surface condition on a microscopic level.

TABLE X

EROSION TEST SCHEDULE - GENERAL EROSION MECHANISM STUDIES

Specimen No.	Material	Velocity (fps)	Erosive Medium	Exposure Time	Remarks
E1	Polyethylene	500	rain	1 min.	Microscopic examination
E2		730	rain	1 min.	Microscopic examination
E3		1120	rain	30 sec.	Microscopic examination
E4		730	rain	30 sec.	Microscopic examination
E5		500	rain	30 min.	Negligible weight loss
E6		500	rain	60 min.	Negligible weight loss - flat-faced specimen
E7		730	rain	42 min.	Weight loss data
E8		730	rain	40 min.	Weight loss data - flat-faced specimen
E9		730	rain	50 min.	Weight loss data - flat-faced specimen
E10		730	90µ sand	5 sec.	Microscopic examination - flat-faced specimen
E11		840	90µ sand	5 sec.	Microscopic examination
E12		880	90µ sand	30 sec.	Microscopic examination
E13		880	90µ sand	100 sec.	Weight loss data
D-1-3	Nickel-coated Epoxy Composite	730	rain	19 min.	Microscopic examination of erosion process
D-2-3		730	90µ sand	45 sec.	Weight loss data/microscopic examination
D-3-3		730	90µ sand	75 sec.	Weight loss data
D-4-6		730	rain	105 min.	Microscopic examination of erosion process
D-5-6		730	90µ sand	205 sec.	Weight loss data
D-6-6		730	90µ sand	70 sec.	Weight loss data/microscopic examination
G1	Graphite-fiber Reinforced Epoxy	730	rain	30 sec.	Weight loss data
G4		730	90µ sand	110 sec.	Weight loss data
G5		730	90µ sand	5 sec.	Microscopic examination
G6		730	90µ sand	20 sec.	Microscopic examination

(a) 110X

(b) 35X
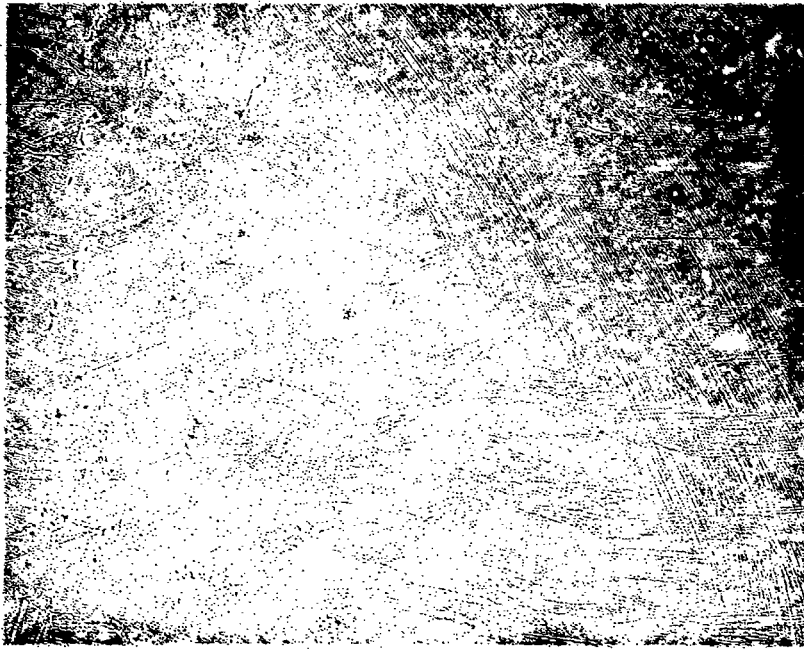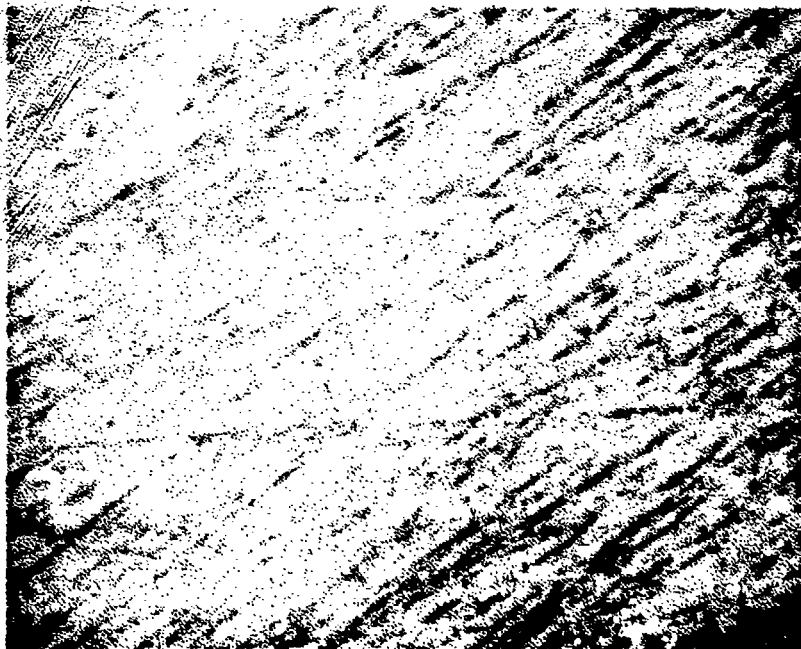
Figure 42 Initial surface conditions of UHMW polyethylene specimens.

4.1.1 Rain Erosion

Rain erosion tests on three specimens of
polyethylene at 500, 730, and 1120 fps indicated that the
time scale for which a particular erosion mechanism is opera-
tive in these specimens is only contracted or expanded as the
impact velocity is increased or decreased but no change is
evident in the sequence f operative erosion mechanisms. It
was therefore decided to conduct the remaining controlled
erosion tests at a single velocity instead of a range of velo-
cities in order to concentrate on describing the erosive
behavior in more detail than would be possible if each speci-
men was run at a different velocity. This approach is adopted
in all of the investigations of erosion mechanisms for the
material systems considered in this research. As long as the
form of the erosion mechanisms (operative in these material
systems) are not dependent on the particle impact velocities,
the velocity-dependence of the erosion rates can be easily
prescribed after the sequence of erosion mechanisms in a
particular material system have been identified and described
analytically.

For the aerodynamically-shaped specimens
exposed to the standard rainfield at impact velocities of 500,
730, and 1120 fps it was found that at 500 fps no weight loss
was recorded after an exposure time of 30 minutes (specimen
25) and at 1120 fps the weight loss was too large after 30
seconds for detailed investigations of the evolving erosion
mechanisms. Therefore 730 fps was selected as the most suit-
able velocity for obtaining weight-loss data and for investi-
gating the erosion mechanisms responsible for material removal.
At 500 fps no weight loss was recorded for the flat-faced
specimen, 5K, after a 60-minute exposure time, however a low
density of small pits, less than 5 mils in diameter, were
beginning to develop on the surface at this time.

Weight-loss curves were obtained for both specimen configurations at 730 fps as shown in Fig. 41. The data are not corrected for differences in the areas exposed to the erosive environments.

At 730 fps a uniform distribution of fibers were raised from the surface of specimens E8 to E10 after a very short exposure to the rain environment. After an exposure of three minutes small pits began to appear on the surface of specimens E8 and E9. The average size of the pits is five mils. The mechanism by which the pits are formed appears to be the raising of portions of the material surrounding a small crack in the material. Several pits are devoid of this raised portion, but it has apparently been torn away during subsequent impacts. The interior of the small pits show a fibrous composition along the walls but the base of the pit is generally smooth. The pit density on the surface of the specimen is not very great. A strong tendency for the pits which were formed to grow was clearly recognized in the subsequent micrographs. Sequences of growth in these specimens can be seen in Fig. 42 to 44. Permanent deformations on the surface of the specimens were also observed after an exposure time of ten minutes. Limited weight-loss data have been obtained for these specimens. The surface of the specimens at the end of the tests were very rough, however it did not appear that any new mechanisms were being activated at this time. The preferential growth of pitted regions was still prevalent. Prior to this time it was observed that the line depressions in the surface did provide sites for the additional removal of material by tearing pieces from the surface. This erosion process occurs after the formation of discrete pits and can be seen in Fig. 44(e).

4.1.2 Sand Erosion

The sand erosion of the aerodynamic-shaped specimens of polyethylene was investigated using the 30-micron
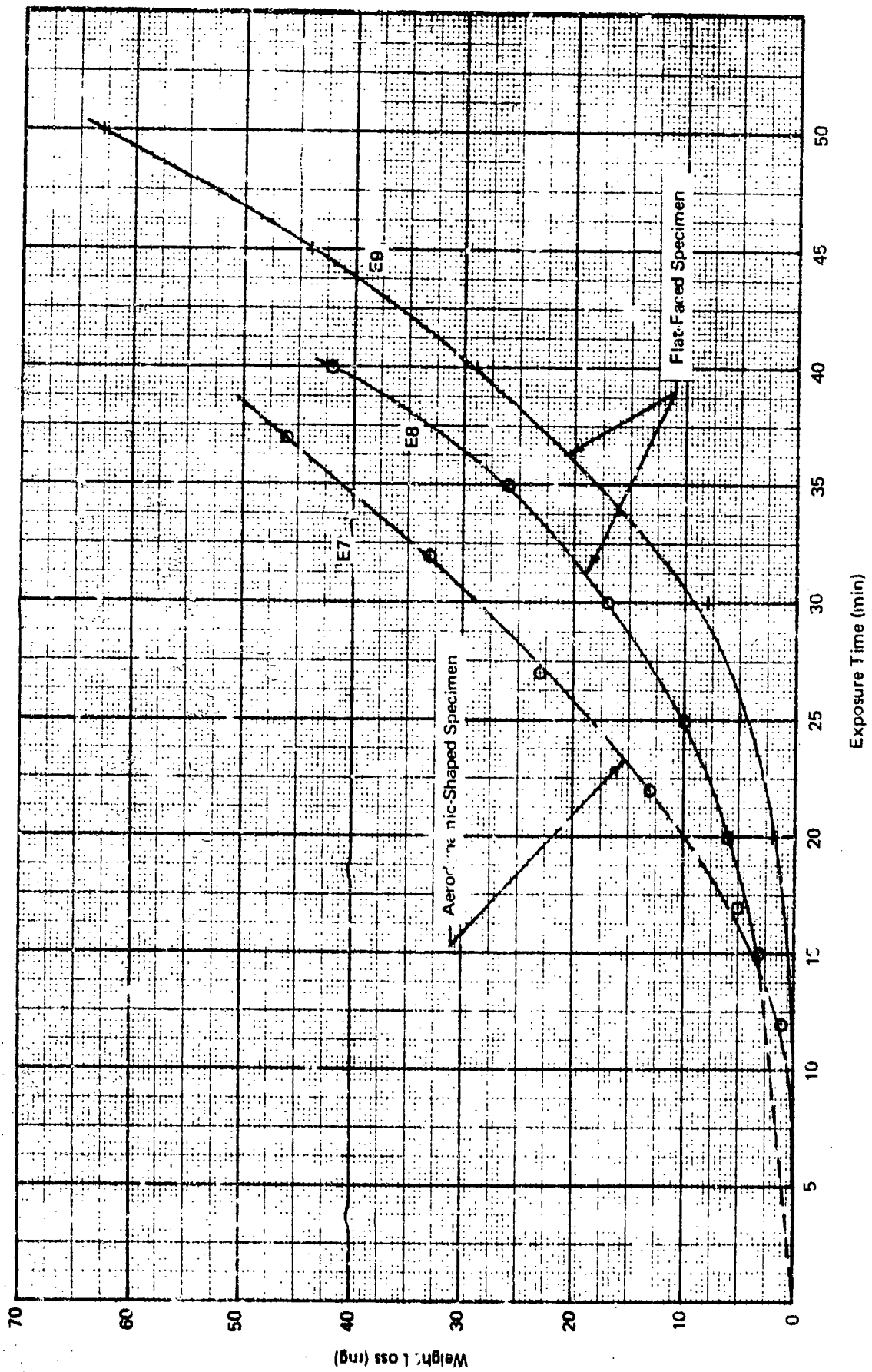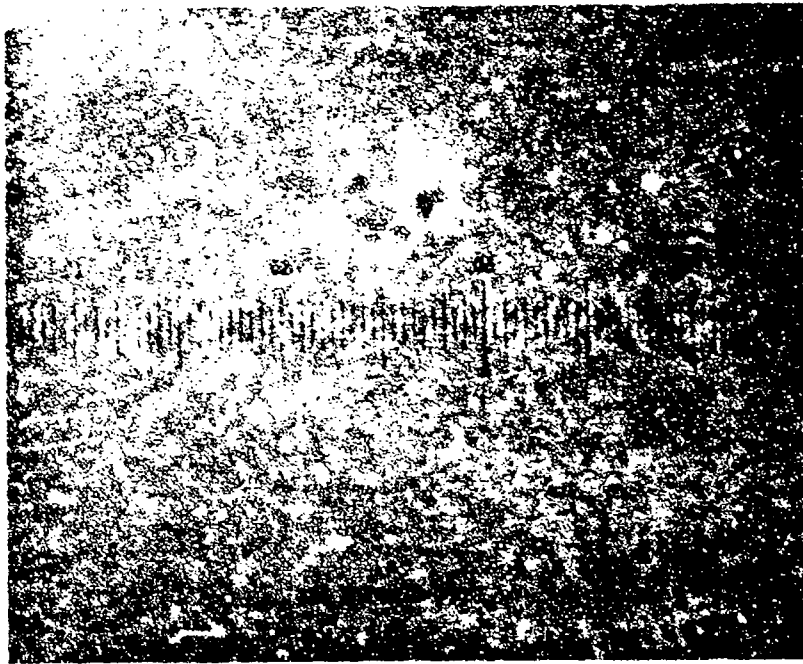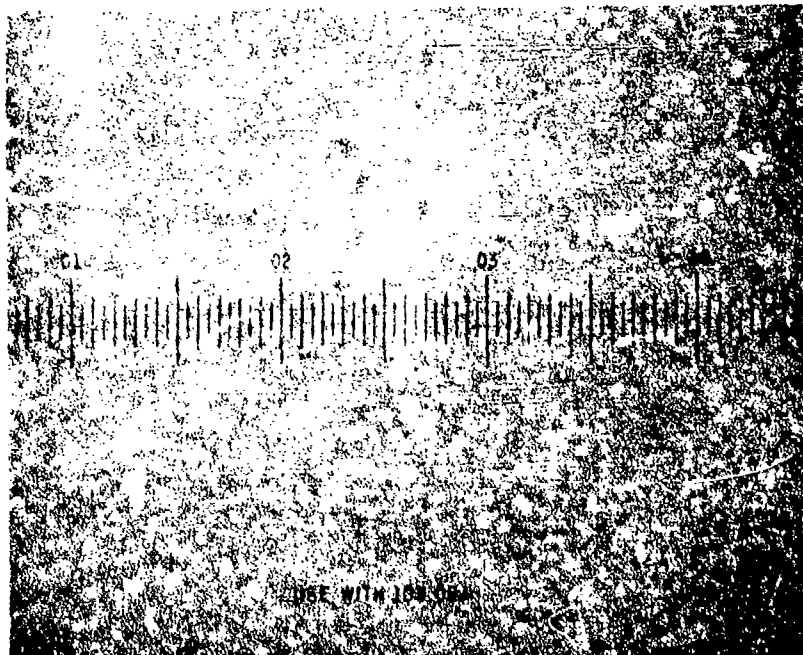
FIGURE 41 Weight loss of UHMW polyethylene in standard rainfield at 375 fps.
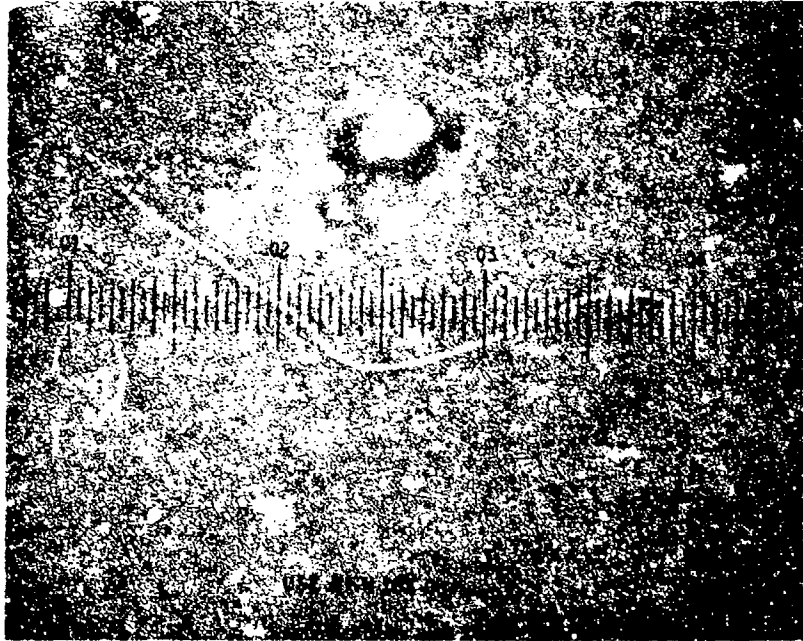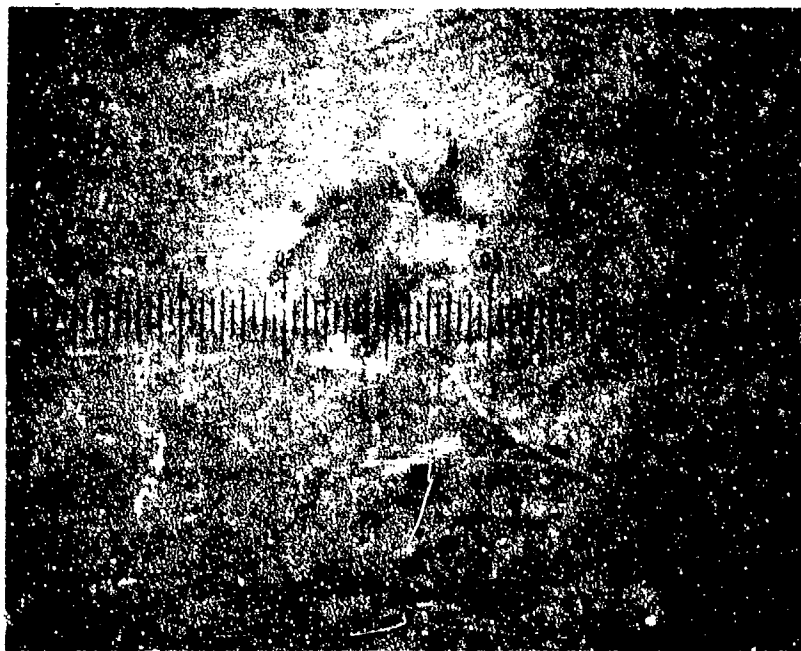
(a) Exposure time 1 min. (110X)

(b) Exposure time 3 min. (110X)

Figure 42 Pit growth on the surface of polyethylene specimen E9 (730 fps in standard rainfield).
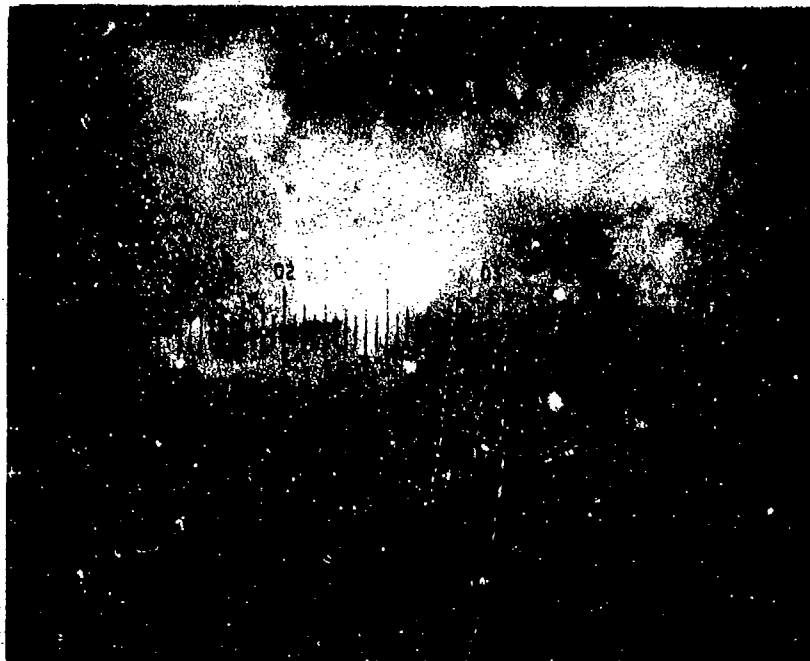
(c)   Exposure Time 7 min.   (110X)

(d)   Exposure time 15 min.   (110X)

Figure 42   Pit growth on the surface of polyethylene
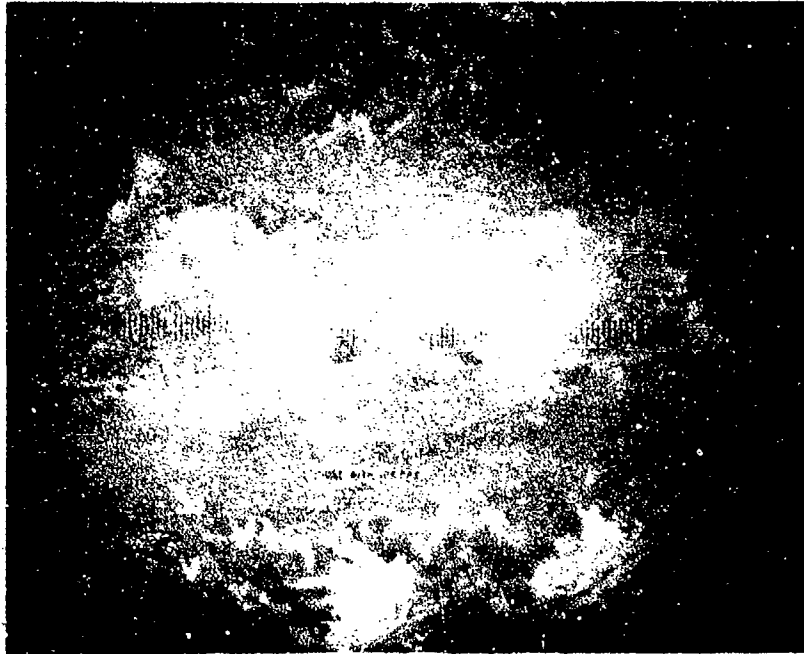specimen E9 (730 fps in standard rainfield).

(a)   Exposure time 3 min.   (110X)
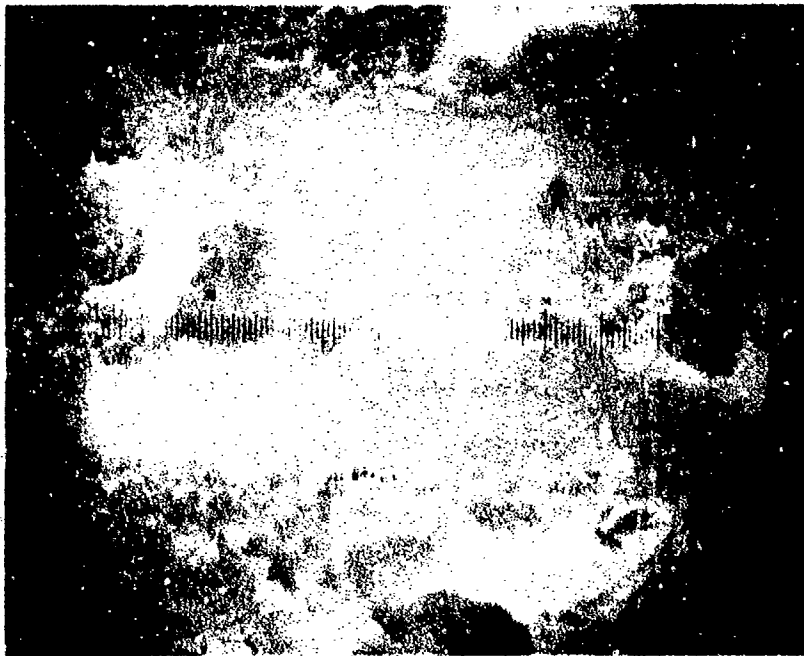

(b)   Exposure time 15 min.   (110X)

Figure 43   Long-time pit growth on the surface of polyethylene
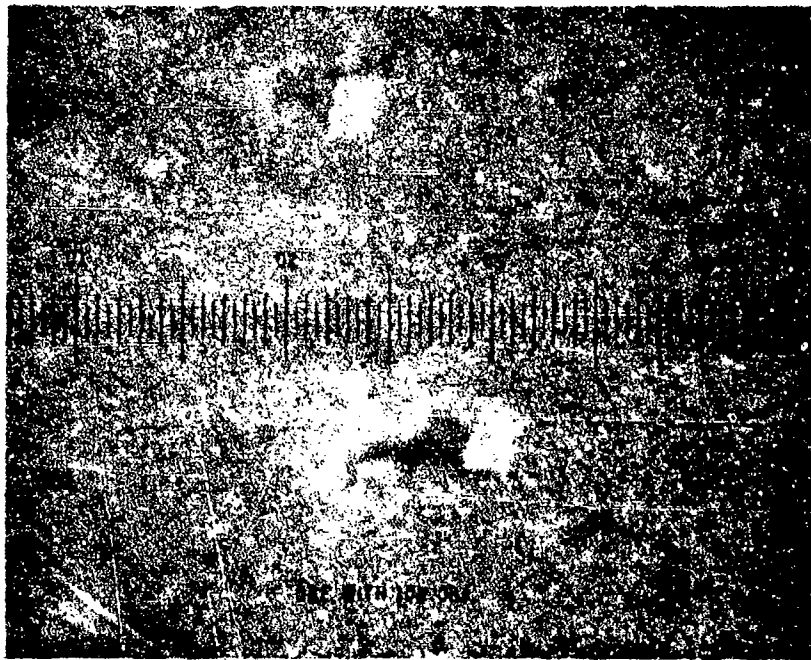specimen E9 (730 fps in standard rainfield).
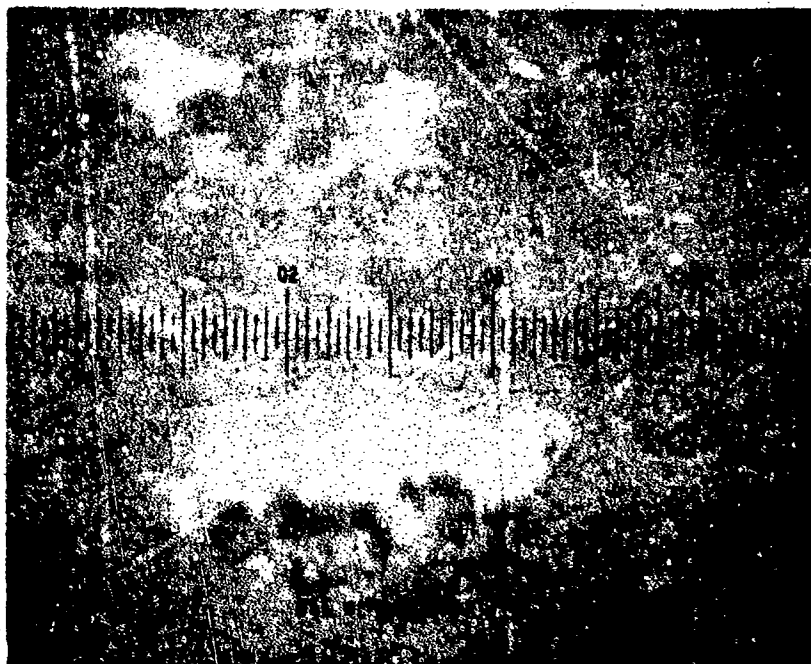
(c)   Exposure time 30 min.   (60X)

(d)   Exposure time 40 min.   (60X)

Figure 43 Long-time pit growth on the surface of polyethylene
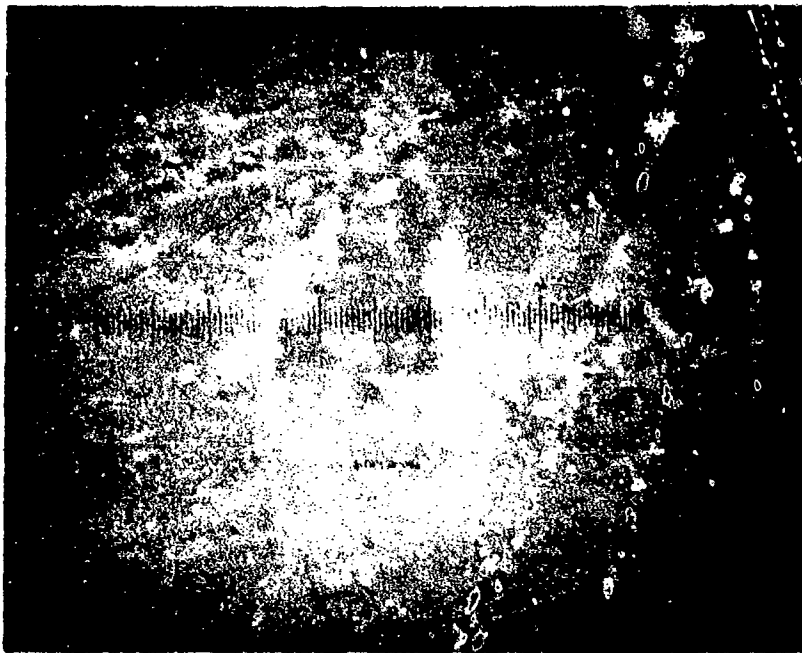specimen F9 (730 fps in standard rainfield).

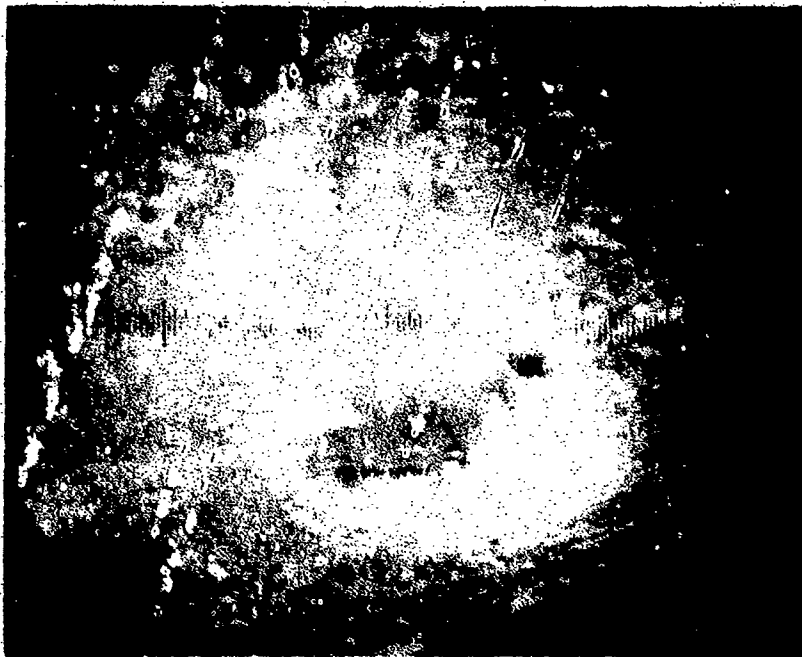(a)   Exposure time 7 min.   (110X)

(b)   Exposure time 15 min.   (110X)

Figure 44   Pit growth and coalescence on the surface of
polyethylene specimen E9 (730 fps in standard
rainfield).

(c) Exposure time 30 min. (110X)

(d) Exposure time 40 min. (110X)

Figure 44 Pit growth and coalescence on the surface of
polyethylene specimen E9 (730 fps in standard
rainfield).

sand at a flow rate of 260 g/min. and an impact velocity of 880 fps. The weight-loss data are plotted in Fig. 45. It is seen that a steady rate of erosion is quickly established. This data can be compared with that previously reported.[39]

The sand erosion mechanism is quite distinct from that associated with rain droplets. The permanent indentations of the sand particles are readily identified along the leading edge of the specimen and the cutting action of the particles can be seen along the curved sides of the specimen. Most of the material removed from the specimen occurs along the sides of the specimen between the angles of 20° and 50° as measured from a plane passing through the longitudinal axis and leading edge of the specimen.

4.2 Erosion of Nickel-Coated, Glass-Fiber Reinforced Epoxy

A series of six specimens of a nickel-coated, glass-fiber reinforced epoxy with coating thicknesses of 3 and 6 mils were exposed to rain and sand erosion environments. The preparation of the specimens is described by Weaver[40]. The specimens tested, as recorded in Table X, are the soft-nickel coatings.

The initial condition of the surface of these specimens is indicated in Fig. 46. The surfaces are moderately rough with the 6 mil coatings being coarser than the 3 mil coatings. Two types of initial surface features are observed: small clyindrical protrusions and extended pits.

4.2.1 Rain Erosion

Two specimens, D-1-3 with a 3-mil coating and D-4-6 with a 6-mil coating, were eroded at 730 fps in the standard rainfield. It was evident from optical microsopic

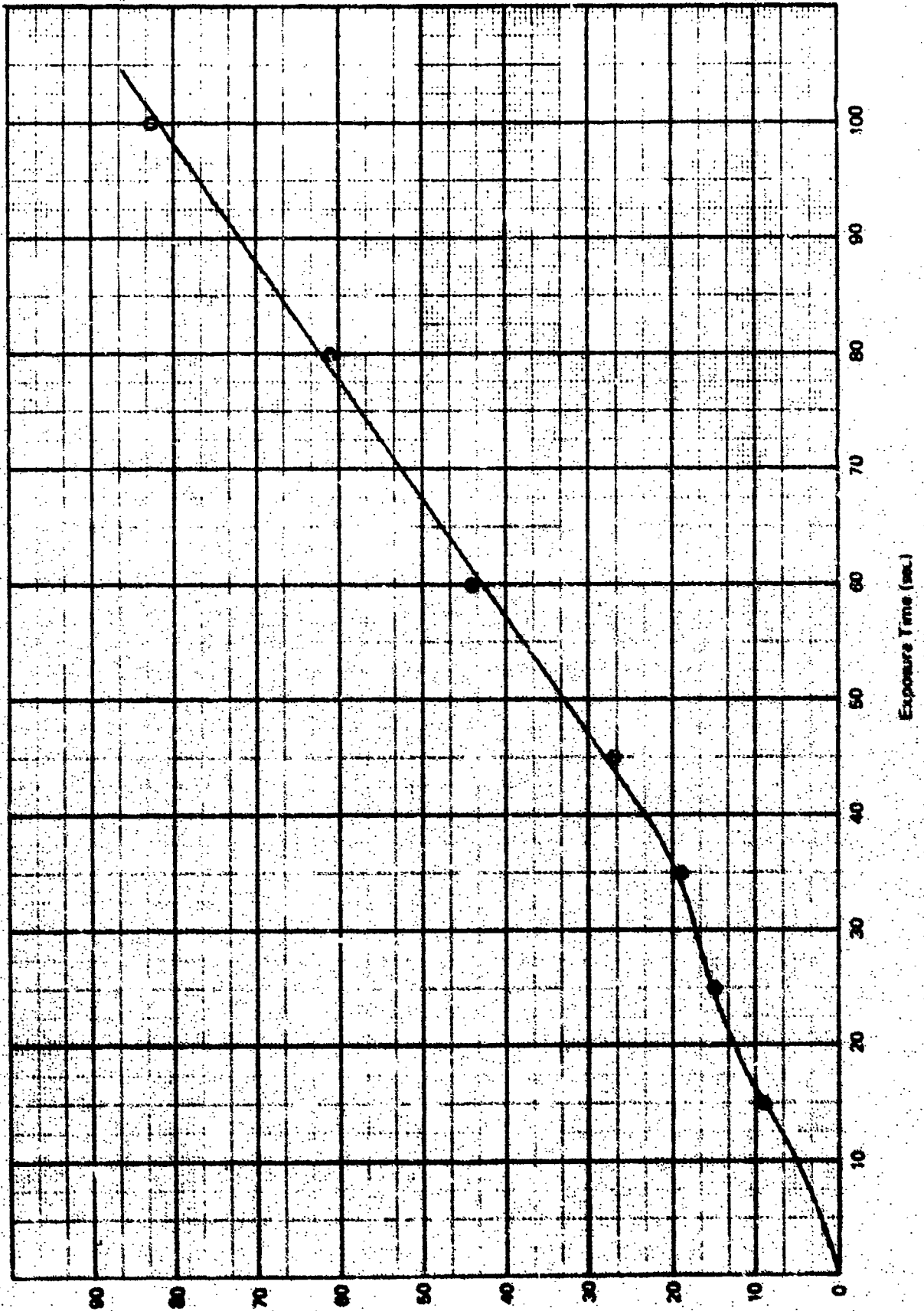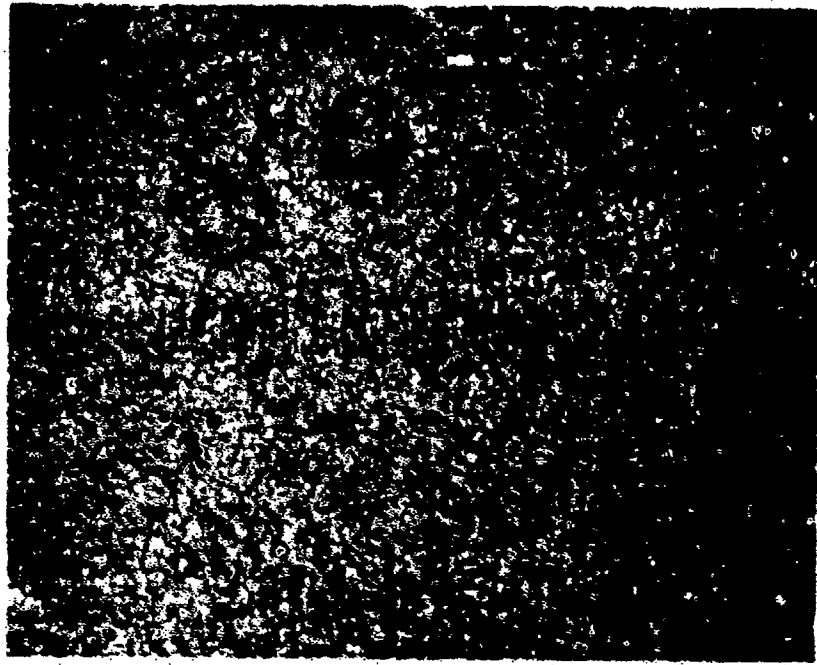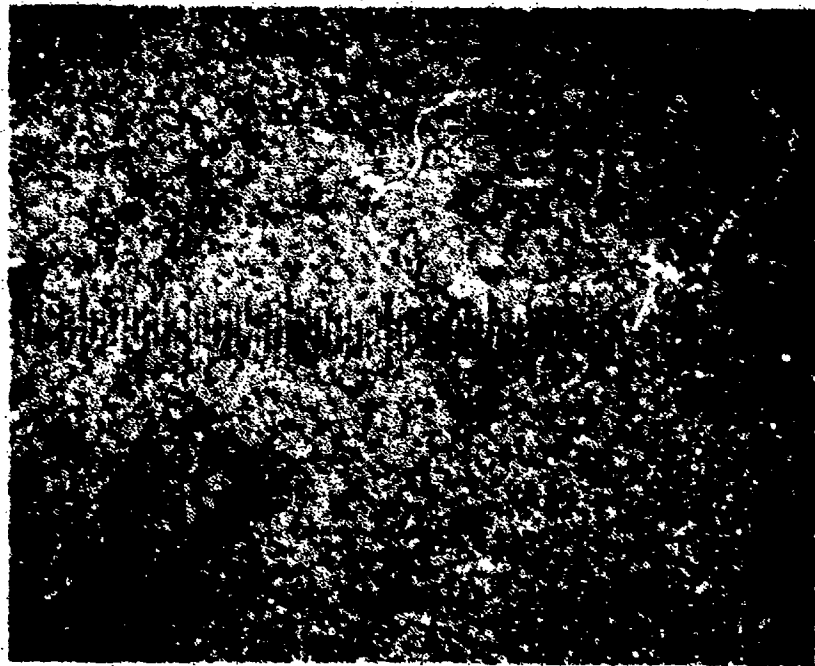FIGURE 45 Weight loss for direct impacts of 90-micron sand on UHMW polyethylene at 880 fps.
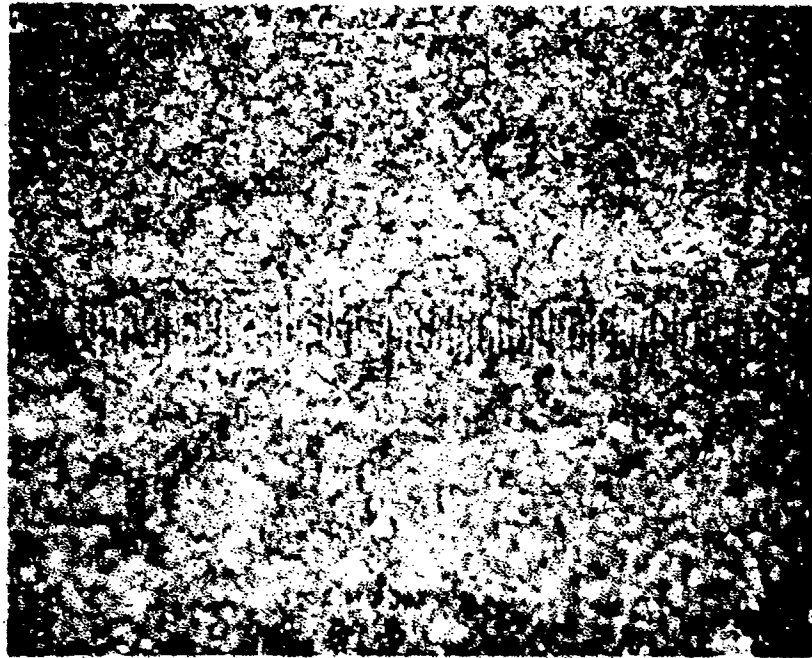
(a) Specimen D-1-3

(b) Specimen D-2-3

Figure 46 Initial surface condition of nickel-coated
glass fiber reinforced epoxy specimens.(110X)

(c) Specimen 1-1-4

(d) Specimen 1-1-6

Figure 46 Initial surface condition of nickel-coated
glass fiber reinforced epoxy specimens. (110Y)

-137-

examination that the surfaces were experiencing very fine-scale plastic deformation without pitting. The initial phase of the erosion process produced a distribution of cracks on the surface which only extend a portion of the way into the thickness of the coating. These fractures generally occur most readily at the base of the protrusions which are initially present on the surface. The cracking becomes more extensive as the exposure time increases. Over the duration of these tests no weight loss was recorded. On a microscopic level there was no evidence of any erosion mechanisms which would contribute to material removal.

Failure occurred in specimen D-1-3 at an exposure time of 15 minutes by localized buckling of the coating at the outboard end of the specimen. The overall configuration of the failure is shown in Fig. 47. The buckled ridges extend 300 to 400 microns above the surface of the coating. Fig. 48 and 49 show the cracked region surrounding the ridges as well as the development of pits which extend well into the coating and in some cases to the surface of the substrate.

In order to see what would happen to the coating now that it had buckled locally, the specimen was placed on the rotating arm and monitored for evidence of gross damage. The test was terminated at 19 minutes when a large portion of the coating surrounding the buckled region was completely removed from the substrate as shown in Fig. 50. At this time some pitting and extensive cracking was observed near the center of the specimen as illustrated in Fig. 51.

Specimen D-4-6 with a 6-mil coating was found to be considerably more resistant to the erosive environment. Negligible damage was observed at a microscopic level until an exposure time of 40 minutes when cracking began to develop on the surface. The severity of the cracking increased
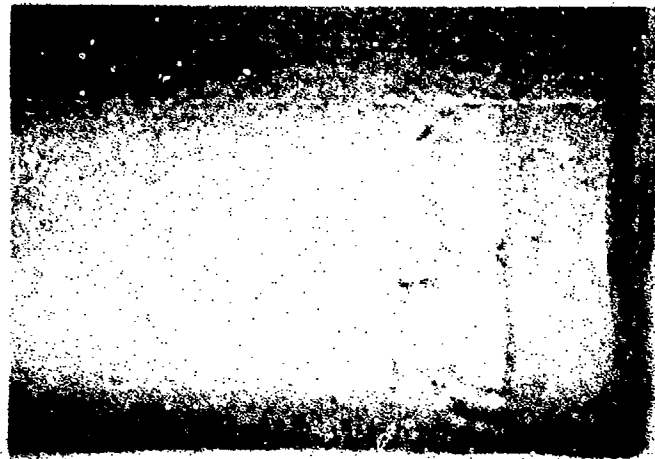
(a) Exposure time 15 min. (7X)

(b) Exposure time 15 min. (15X)

Figure 47 Buckling of nickel coating on specimen D-1-3
in standard rainfield.
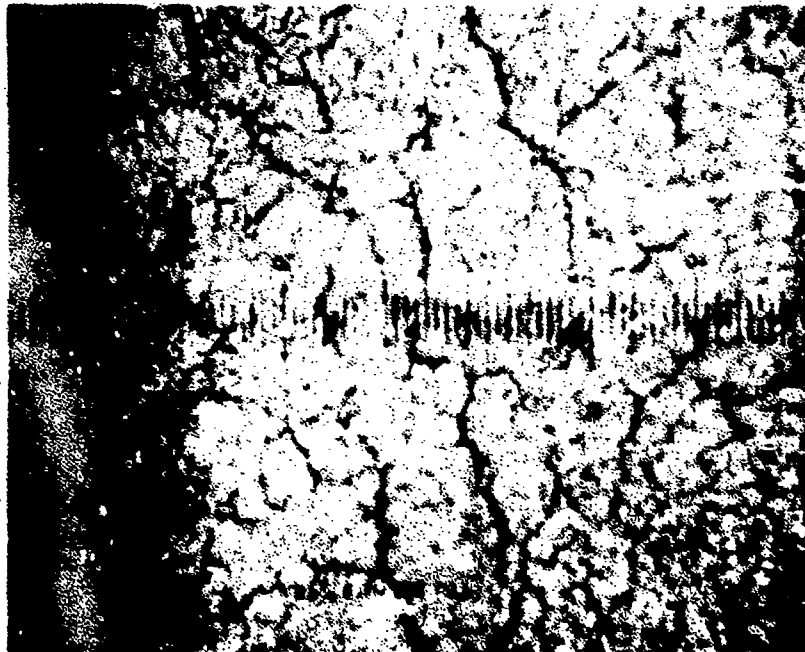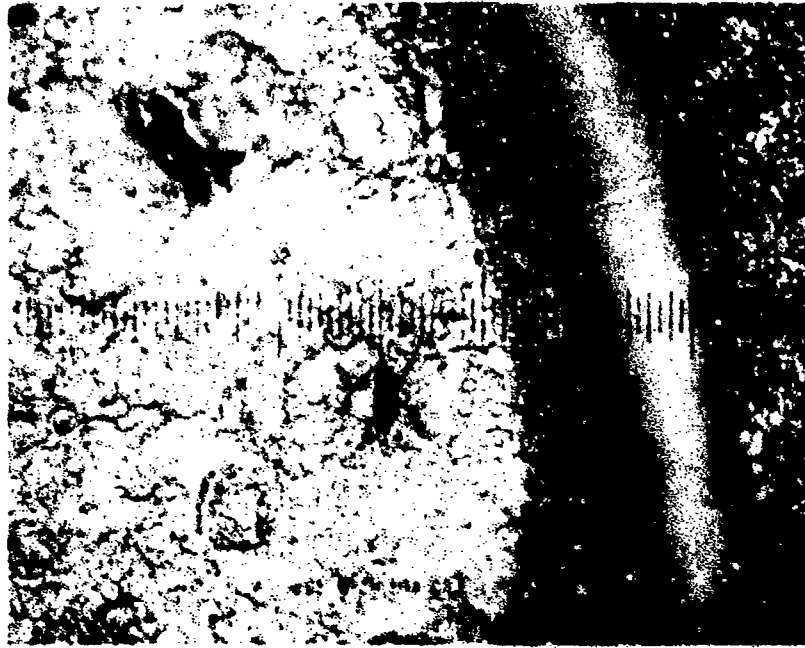
Figure 48   Localized cracking and deep pits in the vicinity
           of the buckled region on specimen D-1-3.   (110X)
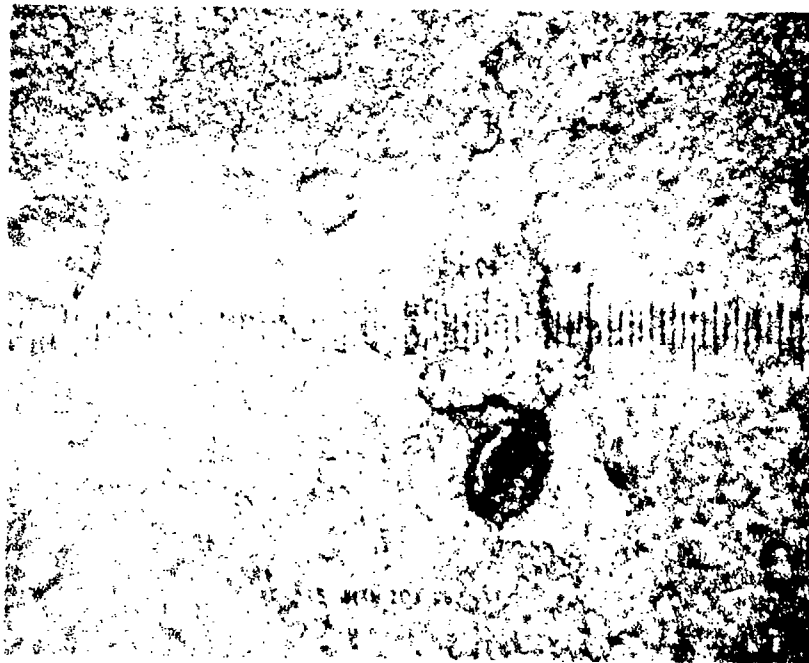
Figure 49 Condition of the surface near the center of
specimen D-1-3 after 15-minute exposure to
the standard rainfield at 730 fps. (110X)
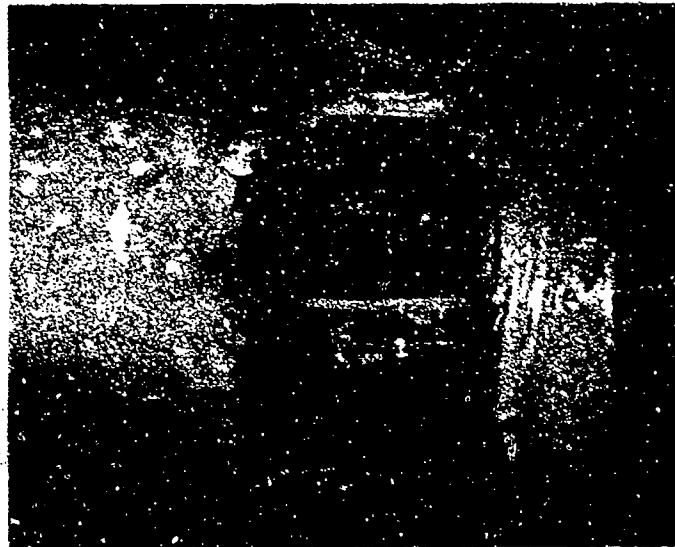
Figure 50 Coating failure at the outboard end of specimen D-1-3 after 19-minute exposure to the standard rainfield at 730 fps. (15X)

Figure 51 Condition of coating near center of specimen D-1-3 after 19-minute exposure to the standard rainfield at 730 fps. (110X)

with exposure time and a low density of deep pits were beginning to evolve. Microscopic examination of the specimen showed that regions with lateral dimensions of 10 to 20 mils were being depressed or raised above the original surface at the inboard end of the specimen at an exposure time of 100 minutes. Some idea of the surface conditions at this time can be obtained from Fig. 52 for the inboard end and from Fig. 53 near the center of the specimen. The specimen was carefully 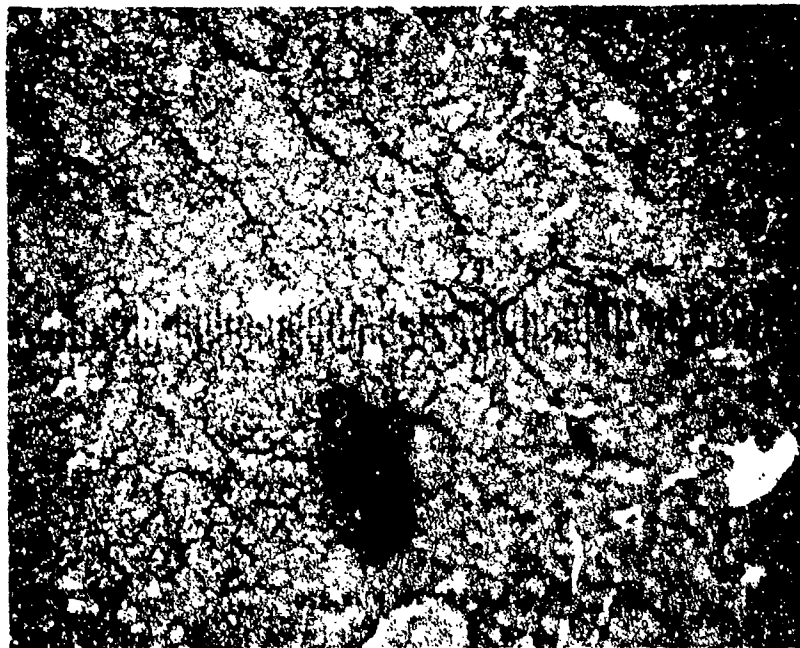monitored as the time of exposure was further increased, until a large hole developed in the coating at an exposure time of 108 minutes as shown in Fig. 54. The test was then terminated.

Although the findings made on the basis of these two specimens will have to be confirmed on the basis of additional tests, it may be conjectured from these tests that the mode of failure depends on the thickness of the coating. The droplet impacts do not appear to produce localized pitting on the surface as is the case of bulk nickel specimens; they tend rather to deform the coating plastically as seen by the shallow depressions formed on the surface and slowly weaken the bond at the interface between the coating and the substrate. The 3-mil coating once freed from the substrate does not possess enough rigidity to resist the centrifugal forces applied to the specimen in the rotating arm appratus and so buckling of the surface coating results. The 6-mil coating fails in a different way, since it is capable of resisting to a greater degree the applied centrifugal loads. The rigidity of the coating and the applied centrifugal forces are not usually a consideration, however the 3-mil coating must not be thick enough to resist the loads imposed by the erosion apparatus even at low velocities.

4.2.2 Sand Erosion

The failure mechanism for the nickel-coated specimens eroded by the 90-micron sand was quite different

Figure 52   Condition of the coating surface at the inboard
end of specimen D-4-6 after 100-minute exposure
to the standard rainfield at 730 fps. (110X)

Figure 53   Condition of the coating surface at the center of
specimen D-4-6 after 100-minute exposure to the
standard rainfield at 730 fps.   (15X)
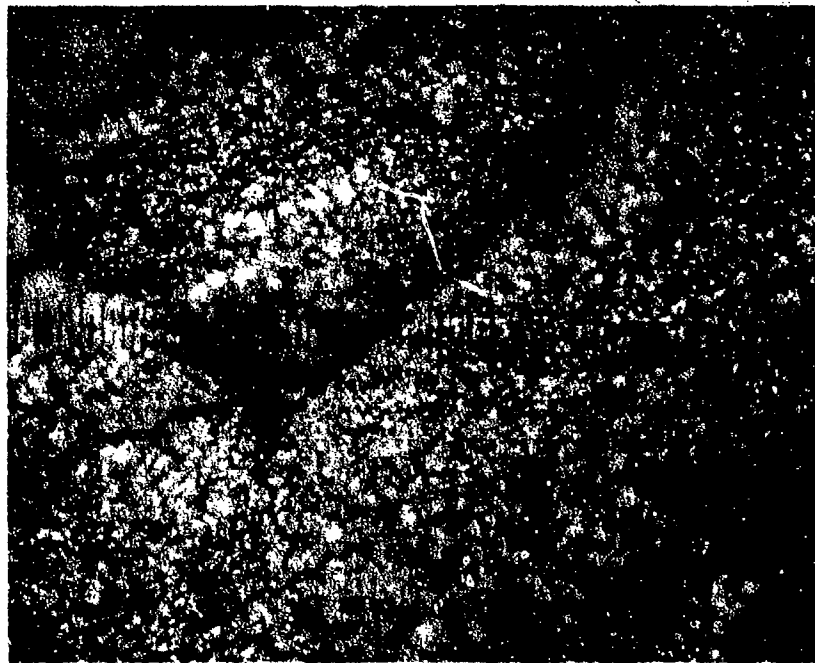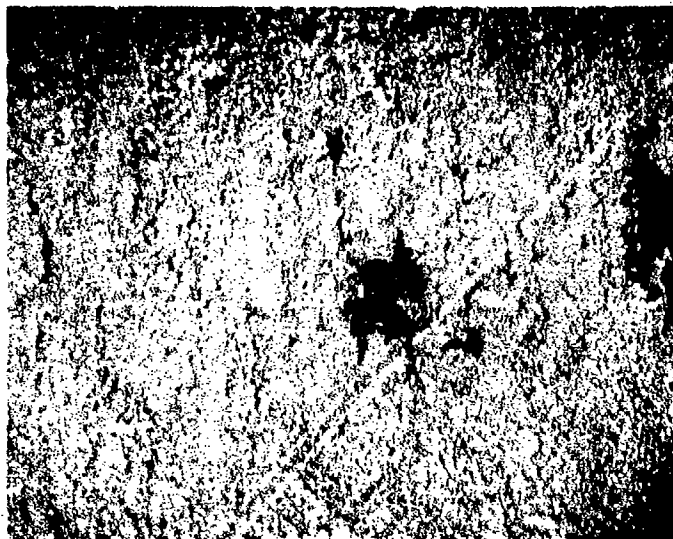

Figure 54   Failure of the coating at the inboard end of
specimen D-4-6 after 108-minute exposure to the
standard rainfield at 730 fps.   (15X)

from that found for the standard rainfield. Two specimens
with a 3-mil coating (D-2-3 and D-3-3) and two specimens with
a 6-mil coating (D-5-6 and D-6-6) were exposed to sand erosion
at 730 fps as indicated in Table X. In this case there was
a measurable weight loss from the coating surfaces as summar-
ized in Fig. 55 and 56. It is seen from these figures that
after a relatively short incubation period a uniform rate of
material removal is established. The sand flow rate was 260g/
min.

For both coating thicknesses failure occurred
by buckling of the coating which was initiated at the out-
board end of the specimen. No cracking of the surface was
observed as in the case of rain erosion; however, initiation
of buckling of the coating took place at an exposure time of
45 seconds for the 3-mil coatings and approximately 85 seconds
for the 6-mil coatings. After the initial buckling the condi-
tion of the surfaces progressively worsened, until they reached
the conditions shown in Fig. 57 and 58 at the end of each test.

It is reasonable to assume that the reduction
in the coating thickness is critical for failure in the case
of sand erosion and that buckling of the coating can only occur
if it is separated locally from the substrate. Specimens
D-2-3 and D-6-6 were eroded by the 90-micron sand for a total
exposure time slightly less than that at which initial buckling
of the coating first occurred in specimens D-3-3 and D-5-6,
respectively. These specimens were cut with a diamond wheel
at a very low rate of penetration, so the bonding between the
coating and substrate would not be disturbed. The sections
were mounted and polished. Microscopic examination of the
interface in all cases revealed that the integrity of the
bond was unaffected by the eroding forces. No evidence for
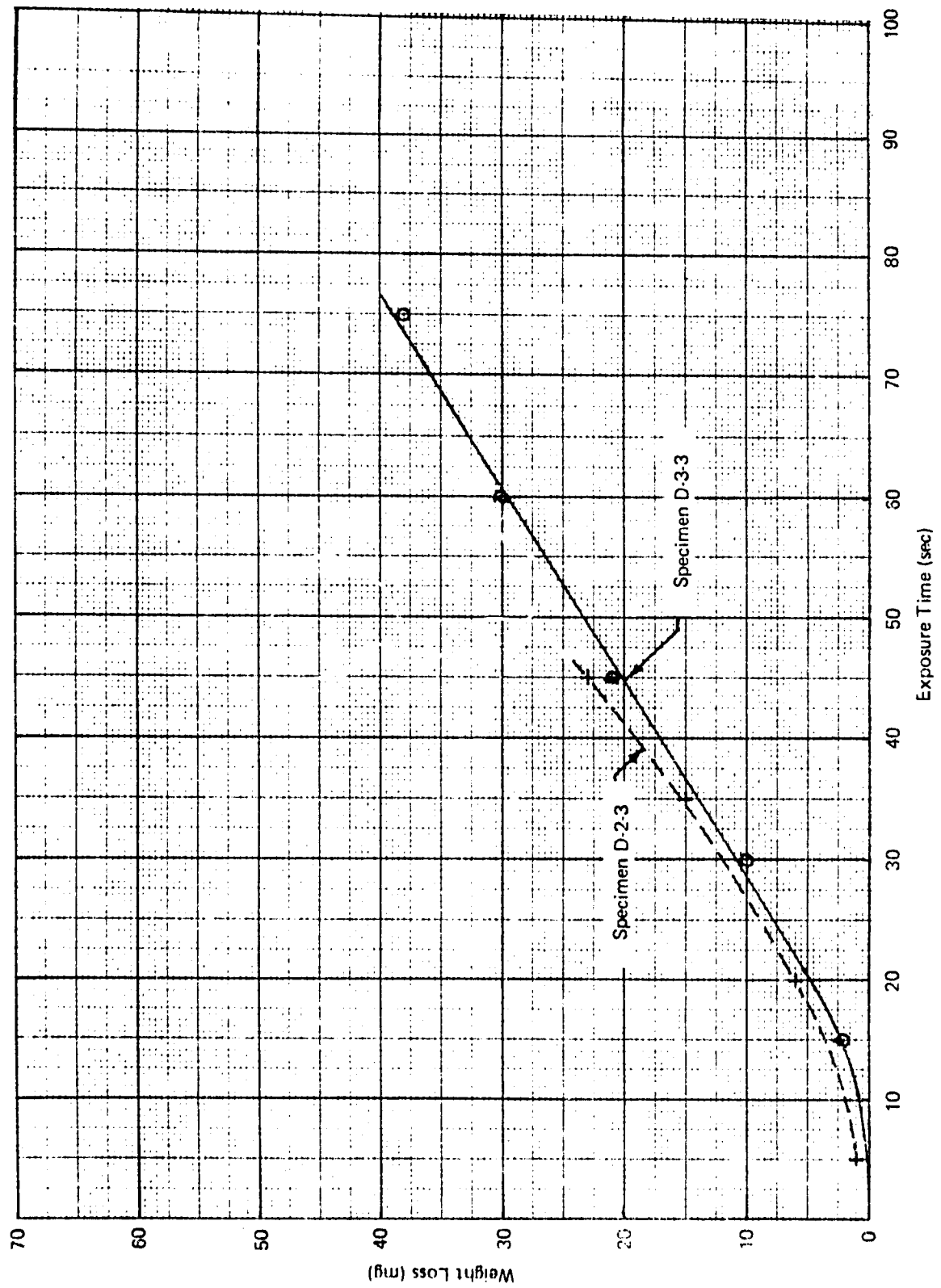the initiation of any kind of failure could be seen.

FIGURE 55   Weight loss for specimen D-3-3 eroded by 90-micron quartz sand at 730 fps.
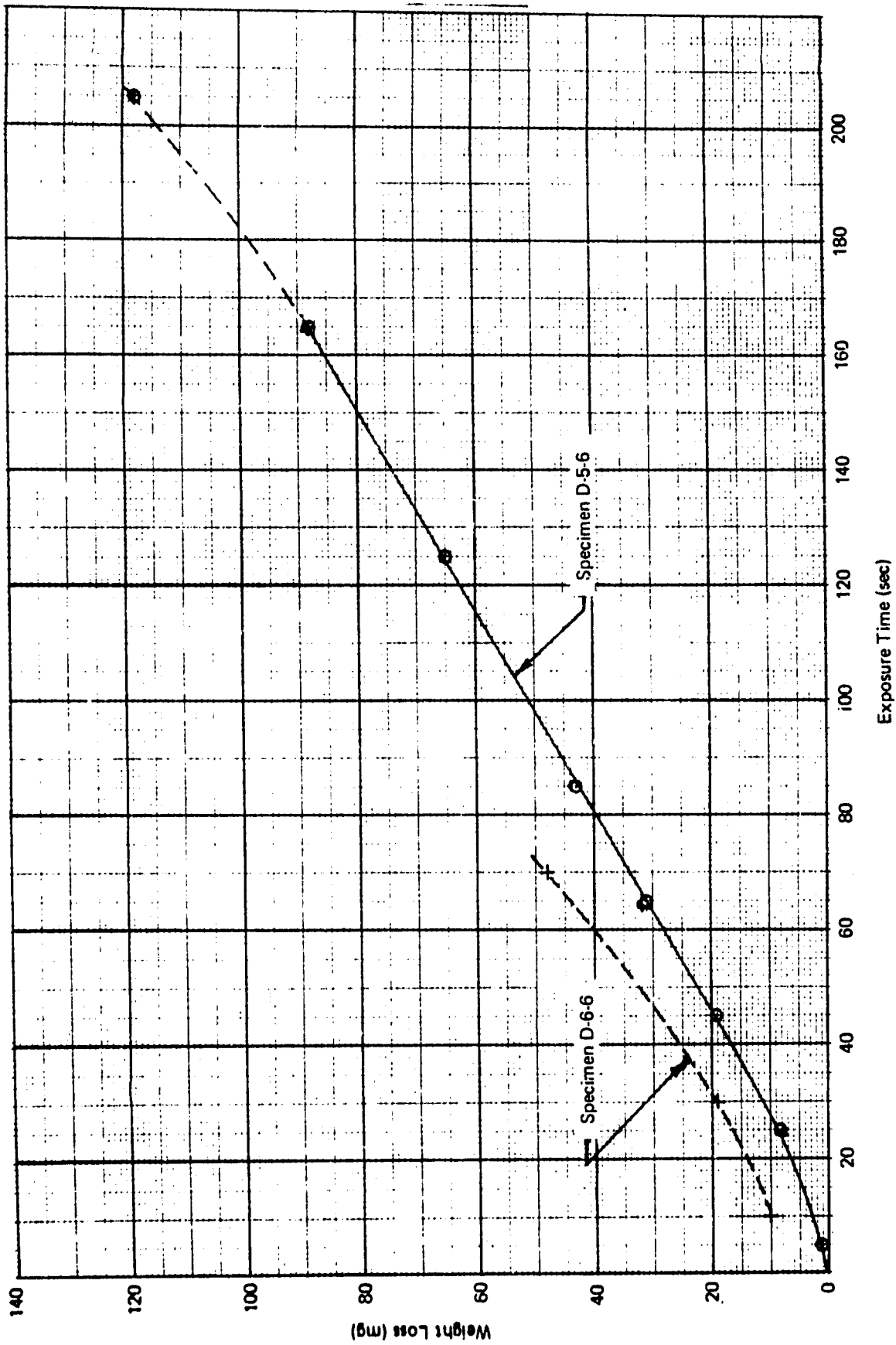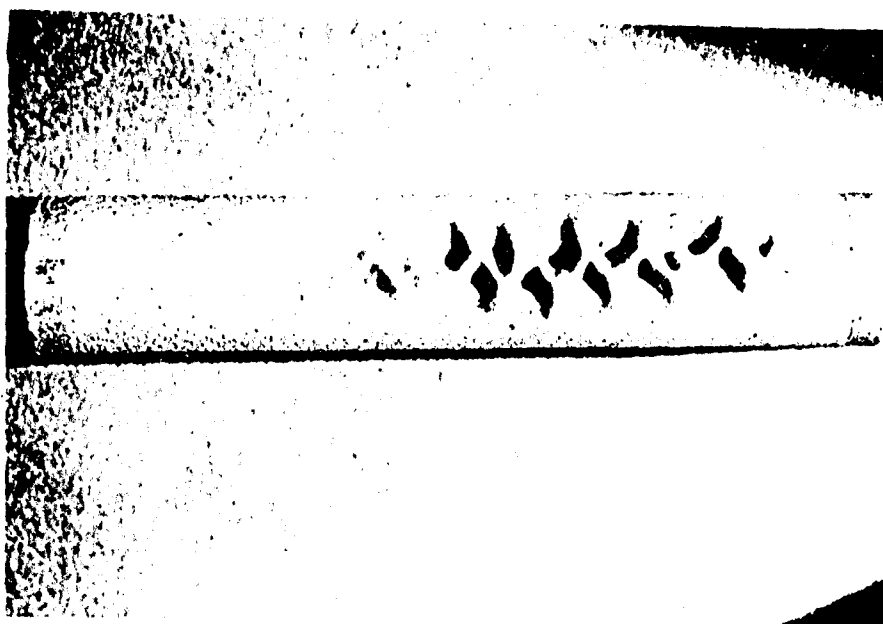
FIGURE 56 Weight loss for specimen D-5-6 eroded by 90-micron quartz sand at 730 fps.

Figure 57 Puckled surface of specimen D-3-3. (1.75X)

(a) 1.75X

(b) 3X

Figure 58 Buckled surface of specimen D-5-6.

The interface for cross sections of segments from specimens D-3-3 and D-5-6 away from the buckled region were also examined microscopically and found to be secure. The mechanism, or critical conditions, for failure of the coated composites has not yet been discovered.

4.3 Erosion of Graphite-Fiber Reinforced Epoxy

Aerodynamic-shaped specimens were exposed to the standard rainfield and the 90-micron sand at a flow rate of 260 g/min. HT-S graphite fibers (manufactured by Hercules Incorporated) were placed in a matrix of ERL 2256 epoxy (Union Carbide Corporation) with ZZLB-0820 hardener. The material properties of these components of the composite are provided in Table XI. The specimens were obtained from the Dayton Research Institute, Composite and Polymeric Materials Laboratory.

The method of preparation was as follows:

The epoxy resin was prepared by mixing 27 parts of ZZLB-0820 hardener per 100 parts of ERL 2256 epoxy. This mixture was diluted with 75 parts of methyl ethyl ketone per 100 parts of epoxy to facilitate impregnating the fiber on a filament winding machine. The epoxy impregnated fiber was cut to the mold size and 48 plies of material were stacked in the mold. Curing of the specimens was accomplished by the following schedule: 2 hr. at 180°F followed by 4 hr. at 300°F in a laminating press. The mold was then cooled to ambient temperature under pressure.

Microscopic examination of the original surfaces of specimens indicated they were smooth except for numerous depressions where an area of the graphite fibers were missing due to fabrication of the composite. The condition of the

TABLE XI

MATERIAL PROPERTIES OF COMPONENTS OF
GRAPHITE-FIBER REINFORCED EPOXY COMPOSITES

	ERL2256/ZZLB 0820 (27 pph)	HT-S Graphite Fibers
Tensile strength (psi)	1.4×10^4	3.71×10^5
Tensile modulus (psi)	4.2×10^5	41.06×10^6
Tensile elongation (%)	6.5	
Heat distortion temp. (°C)	145 - 150	
Density (g/cc)		1.8

original surface is shown in Fig. 59. The appearance of the surface indicates that a moderate porosity may prevail within the interior of these specimens. In order to determine the internal constitution of the graphite-fiber reinforced epoxy specimens, the four specimens were sectioned and examined microscopically. It was found that a high porosity extended throughout the interior of the specimens as can be seen in the typical cross sections in Fig. 60. The porosity was estimated to be on the order of five percent. The fiber content for these composites was determined to be 31 percent by volume. The fibers are distributed nonuniformly throughout the composite as clearly seen in Fig. 60(c) and (d).

The particle impact velocity was held constant at 730 fps in the erosion tests. The duration of each test and its objective are listed in Table X.

4.3.1 Rain Erosion

The erosion characteristics of specimen C-1 exposed to the standard rainfield are quite distinct from those for solid particle erosion. Considerably larger fragments of material are removed in this case due to cracking of the matrix material. The general features of various areas on the eroded surface of specimen C-1 are shown in Fig. 61 to 64. Details of the fractured fibers can be seen in Fig. 61(b) and 62(b). The appearance of the eroded surfaces indicates that bundles of fibers and the surrounding matrix are removed as short longitudinal segments as observed in Fig. 61(a). The missing segment above the deep trough in the center of the micrograph which is about 10 mils long and three fiber diameters thick with the adjacent segments which have also been removed roughly half this length. Cracks in the matrix material are clearly visible in all these micrographs and a broad, deep crack extending under a larger volume of the composite material is shown in Fig. 64. Evidence for the removal of a
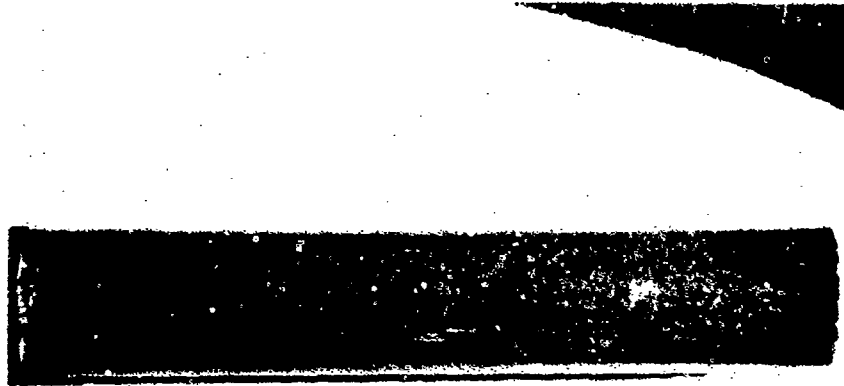
(a) 1.75X
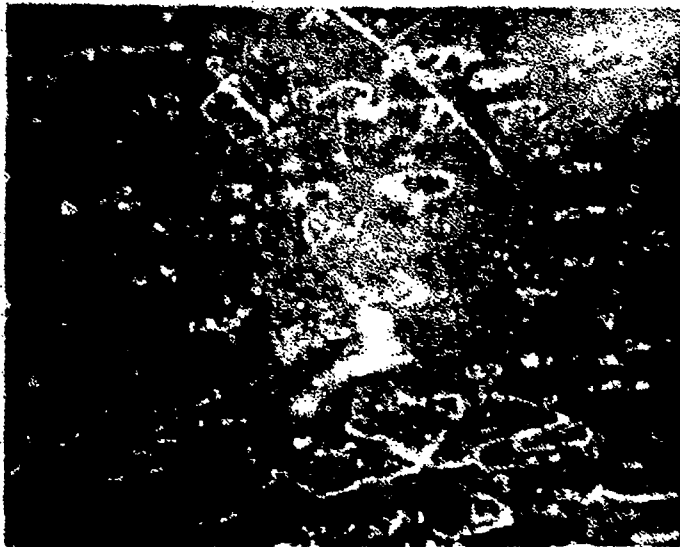
(b) 18X

Figure 59   Original surface condition of graphite-fiber
reinforced epoxy specimens.

a. Specimen C1 (7X)
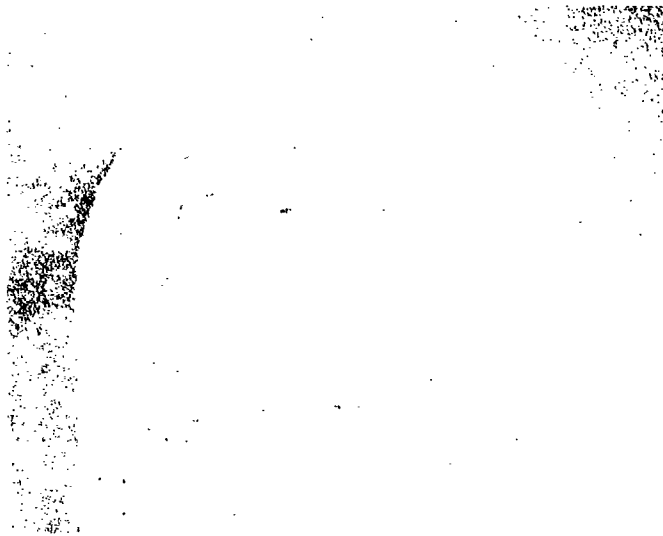
b. Specimen C4 (7X)

Figure 60 Porosity in graphite-fiber reinforced epoxy
specimens (7X).
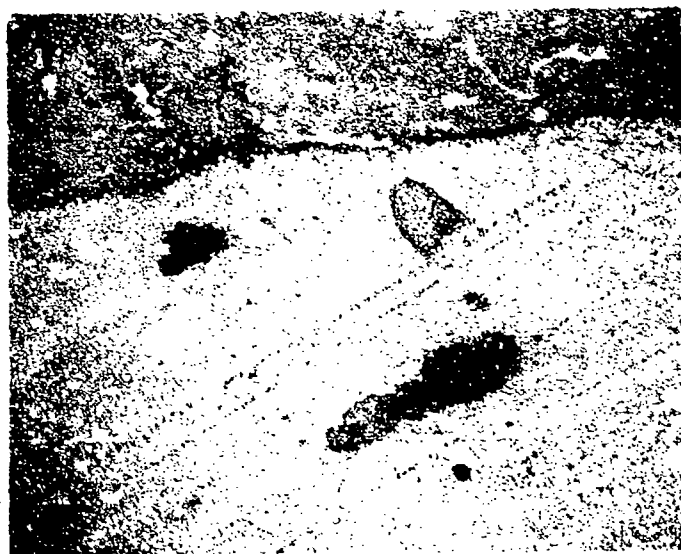
c. Specimen C4 (80X)

d. Specimen C4 (80X)

Figure 60. Porosity in graphite-fiber reinforced epoxy specimens.

a. 163X
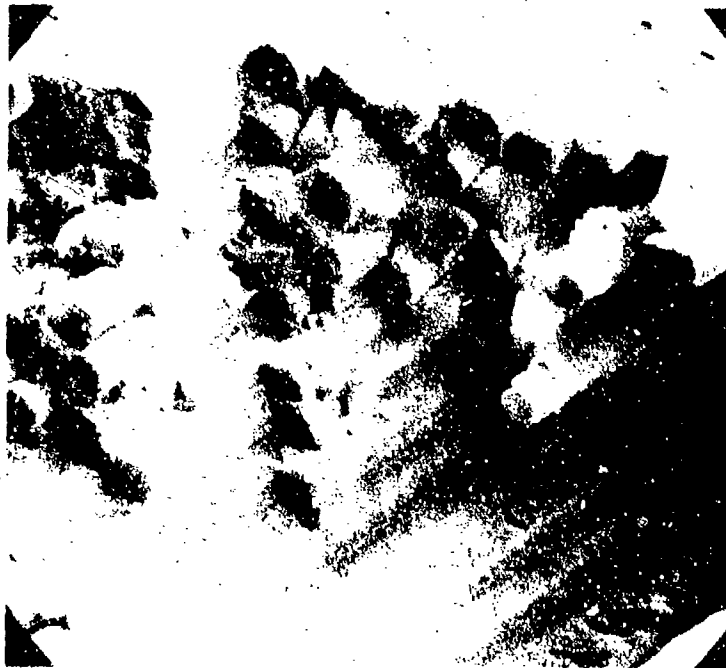
b. 1300X

Figure 61   General features of rain erosion damage
for specimen C-1.

a.   163X
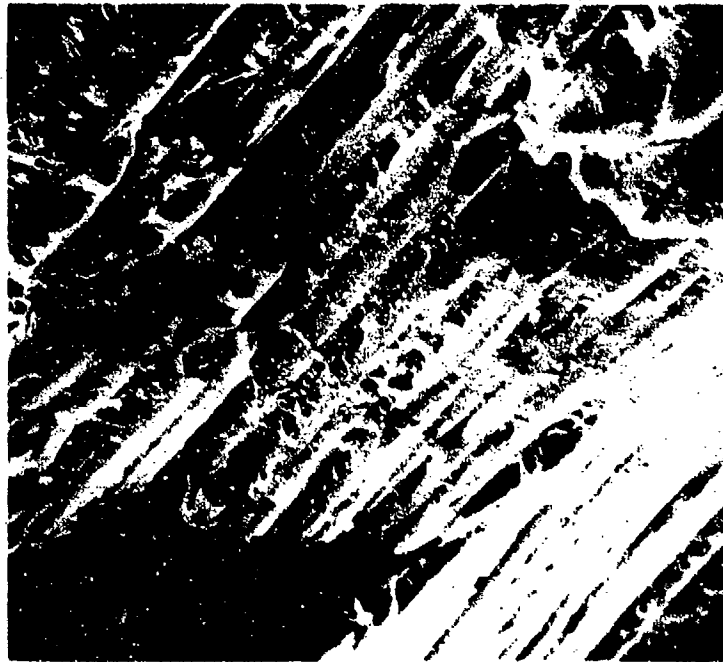
b.   650X

Figure 62   Removal of longitudinal segement of fiber-
bundle for specimen C-1.
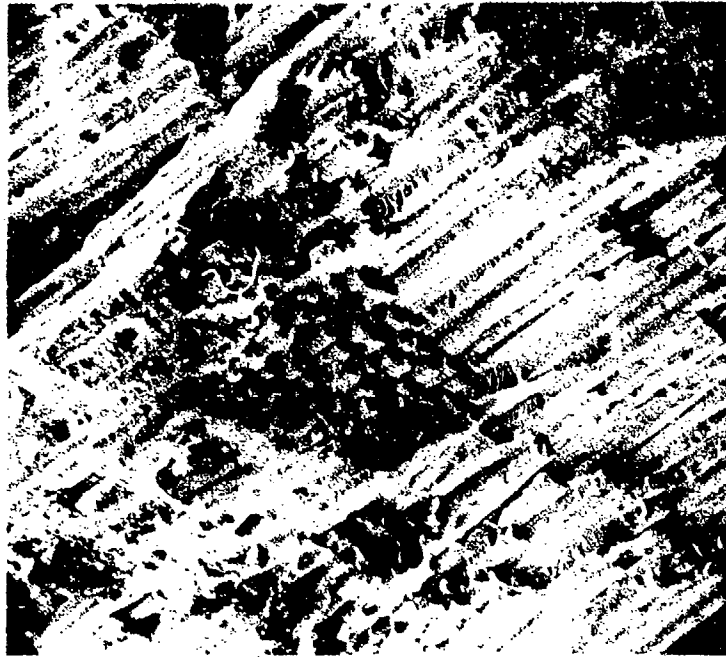
a. 325X

b. 1300X

Figure 63 Detail of broken fibers on surface of
specimen C-1.
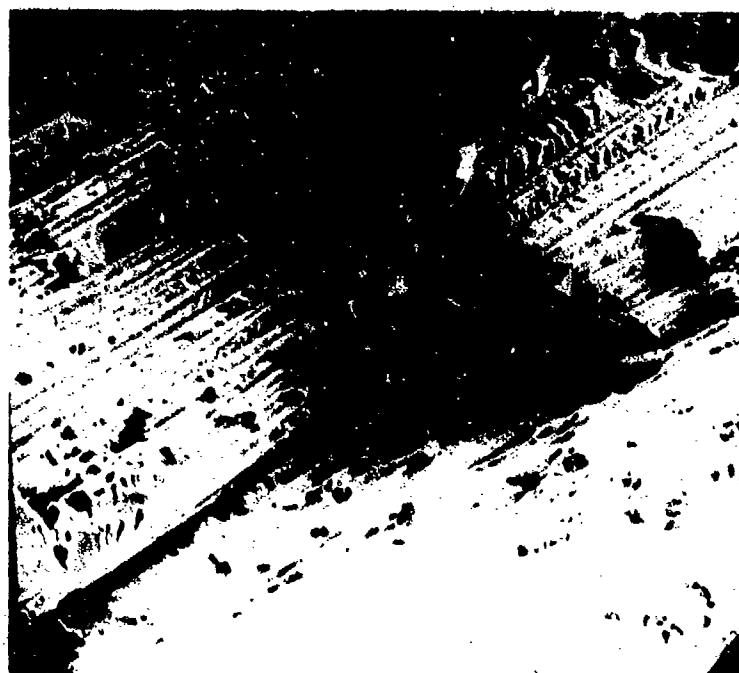
Figure 64   Large crack penetrating the eroded surface
of specimen C-1 (163X).

short segment approximately 6 mils in length is shown in the center of Fig. 62(a) with a detail of the fracture surface provided in Fig. 62(b).

A preliminary hypothesis for the operative erosion mechanism for the intermediate to later stages of the erosion process has been formulated on the basis of these microscopic investigations. The direct impact of the water droplets produce local fractures which penetrate the matrix material but do not crack the graphite fibers. Separation occurs at the fiber/matrix interface which would indicate the bonding between the fiber and matrix is the critical component in the composite structure. Once a longitudinal crack has been nucleated parallel to the direction of the fibers it will grow during subsequent impacts in addition to the formation of other longitudinal cracks in the vicinity of the first one. A longitudinal fracture network will continue to develop until segments of the composite are nearly freed from the bulk of the material. The pressure from a properly oriented droplet applied to the cracks surrounding a material segment will push the segment out from the surface and produce intense localized bending. This condition should be roughly equivalent to a beam rigidly supported at its end and subjected to a transverse distributed load. This observation provides the basis for a simple model which may be developed from elementary concepts from beam theory. The micrographs of the fracture planes at the ends of these segments (Fig. 61(b) and 63(b) show that the fibers behave in a perfectly brittle manner. The fracture network can extend beyond the ends of the initial segment removed making it possible for removal of additional fragments along a longitudinal bundle of fibers. At this point the local conditions can be considered equivalent to a cantilever beam subjected to a distributed load. This process can continue along a group of fibers until conditions become unfavorable to further fragmentation as in the case of the large fiber bundle consisting of seven to eight layers in the center of Fig. 61(a).

The micrographs in Fig. 65 show voids in specimen C-1 which are beginning to be uncovered. The fractures at the ends of these voids are similar to those observed for regions in which no voids are found to exist. The significance of the voids in relation to the overall erosion process is not known at this time, however in the case of rain erosion they should provide favorable conditions for subsurface cracking of the epoxy matrix.

The removal of material from the surface of the specimens by both fluid and solid particle impacts takes place by the removal of pieces of the complete composite in a manner similar to a brittle, homogeneous material. The presence of the fiber reinforcement does not improve the erosion resistance of the composite. In the case of rain erosion, progressively larger pieces of material are removed from the specimen as the exposure time increases. The bonding surfaces of the fibers lying parallel to the longitudinal axis of the specimen become more and more susceptible to penetration and cracking by the rain drop impacts as the erosion pits in the surface deepen with the length of exposure to the erosive environment. This effect is clearly seen in the shape of the weight-loss curve in Fig. 66. The condition of the surface of specimen C-1 at the end of the weight-loss evaluation is shown in Fig. 67.

4.3.2 Sand Erosion

The condition of specimen C-4 when exposed to a sand environment is shown in the micrographs in Fig. 68. Material is removed on a very fine scale by localized cracking of both the fibers and matrix. The exposed fibers are relatively free of the surrounding epoxy (Fig. 69), so the epoxy must be chipped free from the surface of the fibers and then the exposed fibers are pulverized during subsequent impacts. Aerodynamic-shaped specimens were used, so the

a. 153X

b. 325X

Figure 65 Exposed voids on the eroded surface of
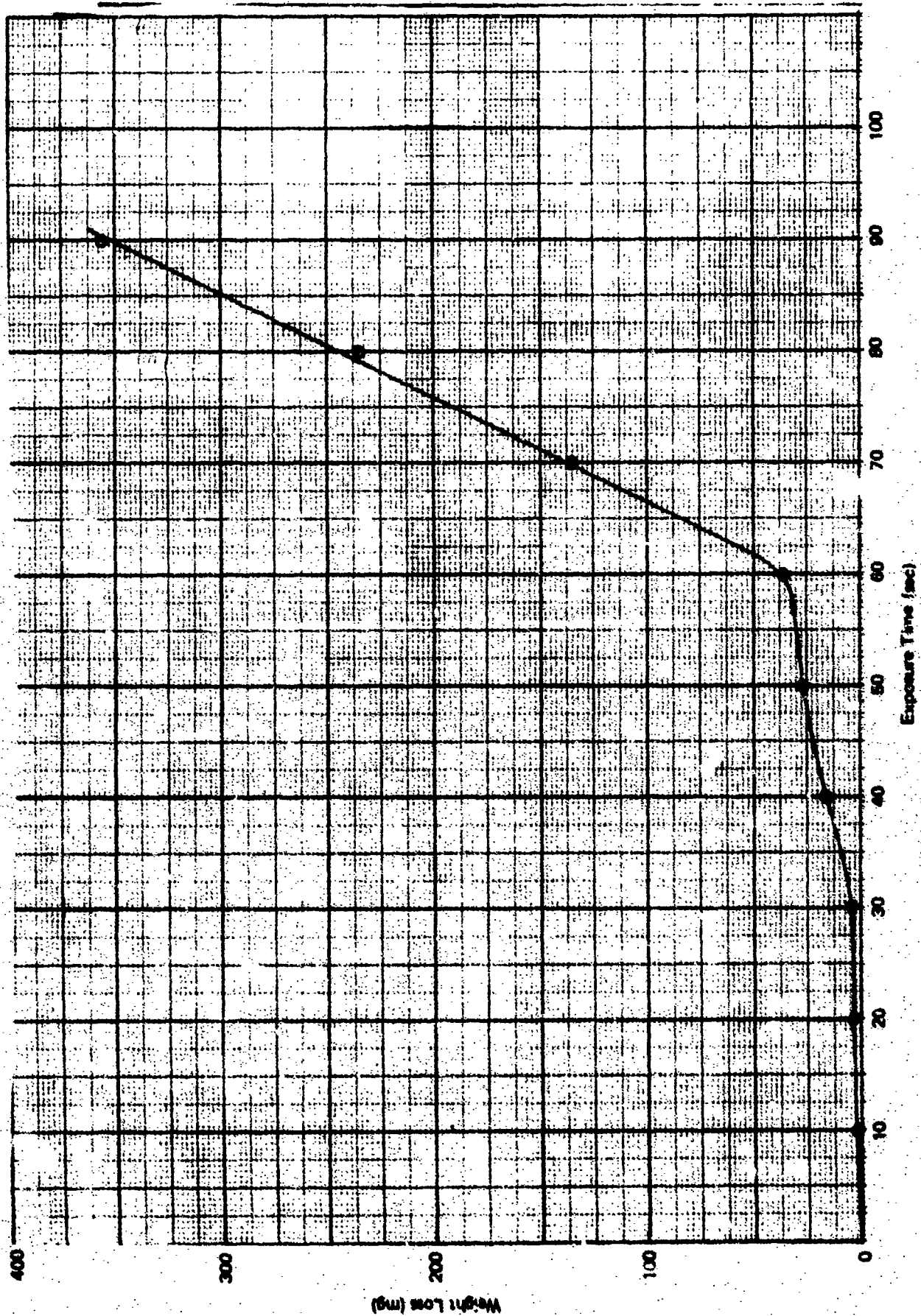specimen C-1.

FIGURE 66 Weight loss for graphite-fiber reinforced epoxy specimen C-1 in standard rainfield at 730 fps.
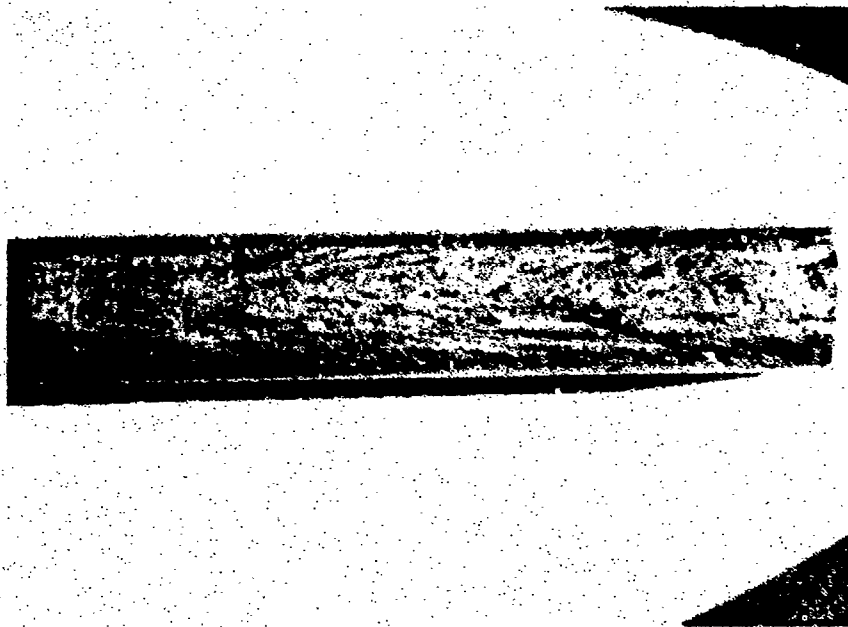
Figure 67 Condition of eroded surface of specimen J-1 at
end of test. (1.75X)
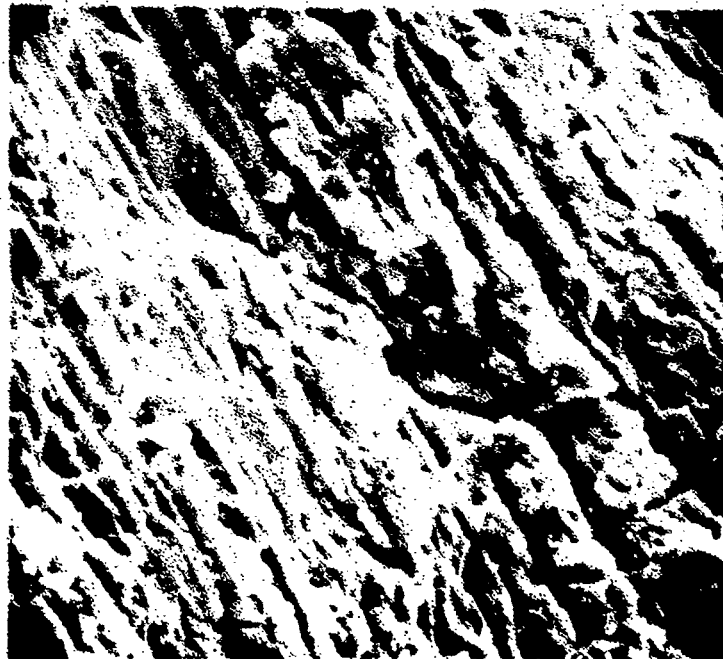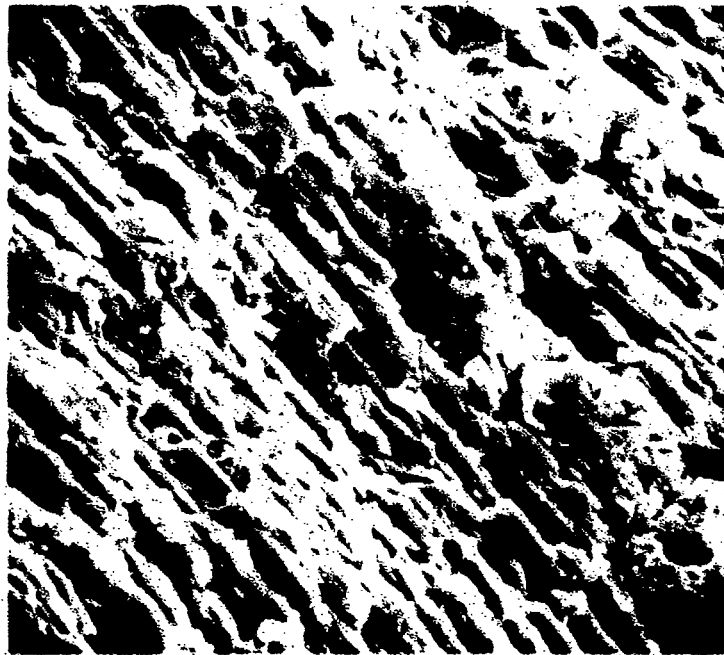
Figure 68   Sand eroded surfaces of specimen C-4 in the
            vicinity of the leading edge (650X).
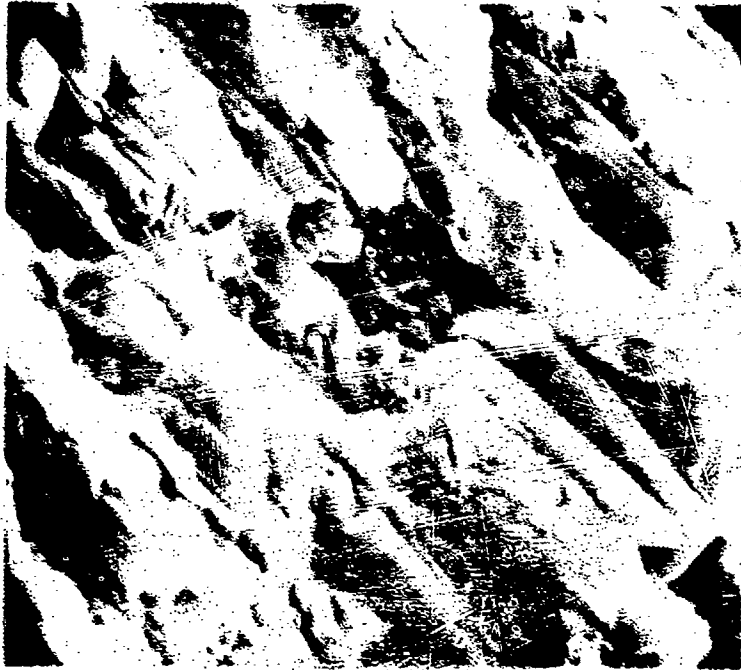
-172-

Figure 1.

erosion damage will be a combination of direct deformation and wear deformation. The micrographs in Fig. 68 and 69 depict the surface condition near the leading edge of the specimen, while the micrographs in Fig. 70 show the surface condition away from the leading edge where the overlying epoxy is still being removed. The micrographs for the erosion by 90-micron sand particles on specimen C-4 in Fig. 68(a) show areas where well-defined particle imprints can be identified. The fracture boundary crossing a number of fibers shows a degree of uniformity which would indicate that it was produced by the shearing action of an impacting, irregular-shaped sand particle. The primary erosion mechanism in this case is fragmentation of the matrix and fibers which occurs at a uniform rate throughout the entire exposure time except for the initial stage of the erosion process as evidenced by the linearity of the weight-loss curve in Fig. 71. The smoothness of the eroded surface after 100 mg weight loss can be seen in Fig. 72. The sand erosion of specimens C-4 to C-6 did not exhibit the dependence on the angle of attack for the impacting particles which was found to prevail for the polyethylene specimens. The degree of material removal was constant up to an angle of 60° as measured from the plane passing through the longitudinal axis and the leading edge of the aerodynamic-shaped specimen.

The micrographs in Fig. 73 show voids beginning to be exposed on the eroded surface of specimen C-4. When the material overlying a void is thin enough, there will be a localized weak area which will erode much more quickly than material volumes with no porosity. However the total effect for the number of localized weak areas of this sort is a relatively small perturbation in the overall erosion rate. The approximate thickness of the overlying material for the crack shown in Fig. 74 is 14 mils.

-161-
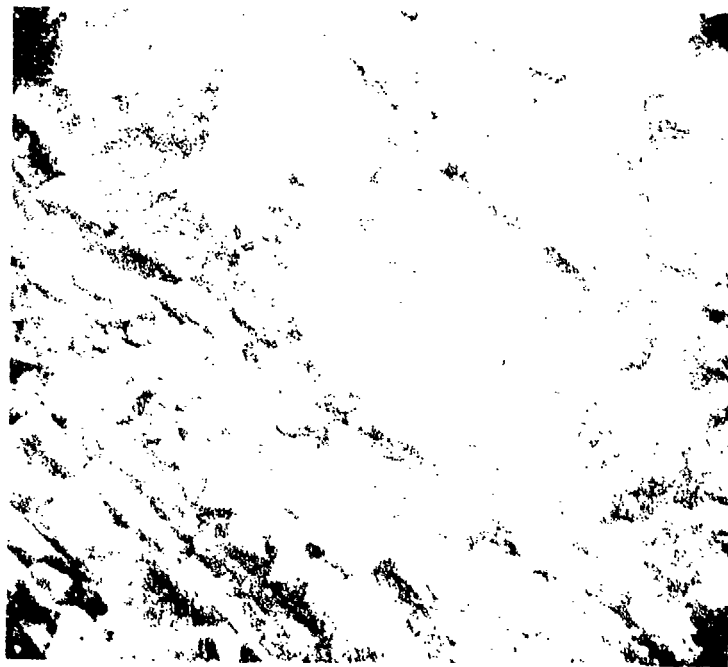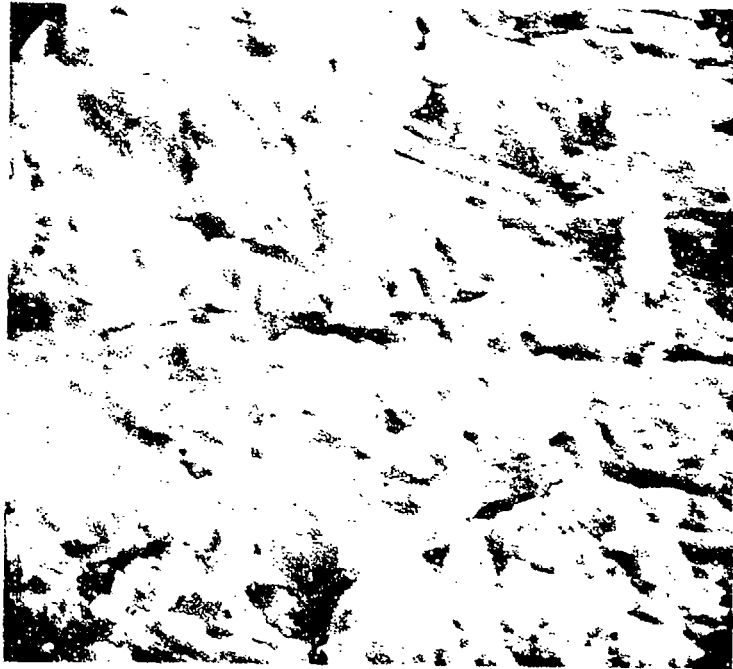
Figure 70 Sand erosion damage at areas away from
the leading edge on specimen C-4 (650X).
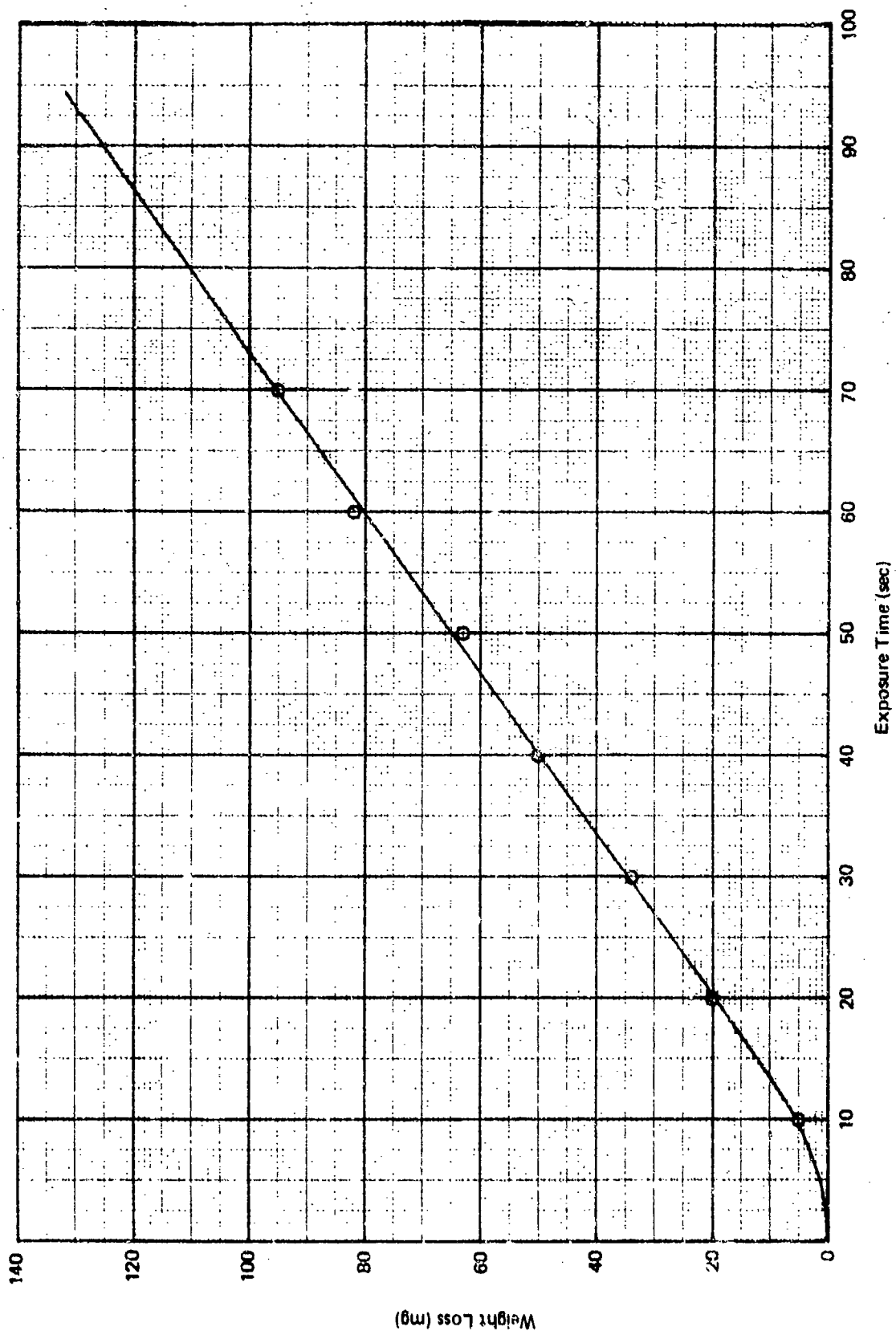
FIGURE 71 Weight loss for direct impacts of 90-micron sand on glass-fiber reinforced epoxy specimen C-4 at 730 fps.

-163-
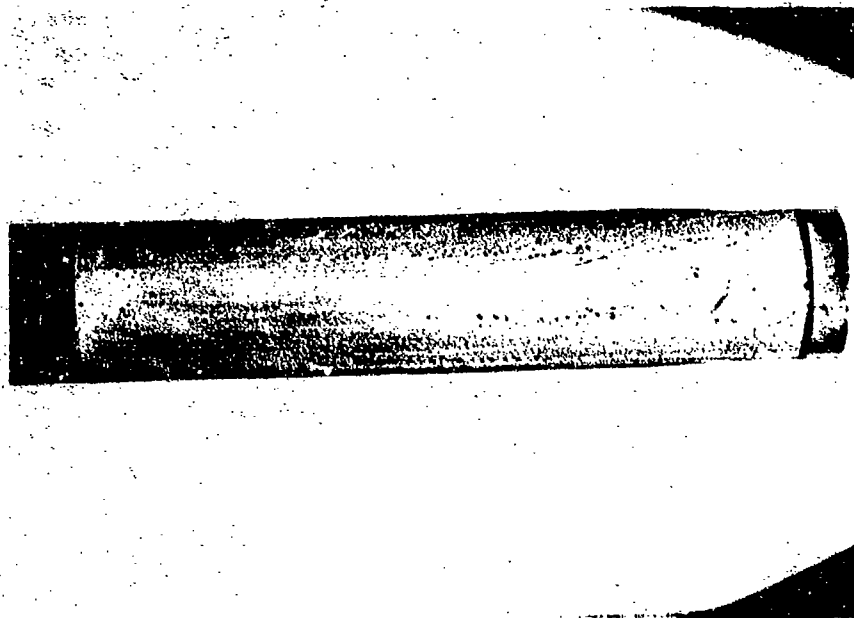
Figure 72   Condition of eroded surface of specimen C-4
at the end of test.   (175X)
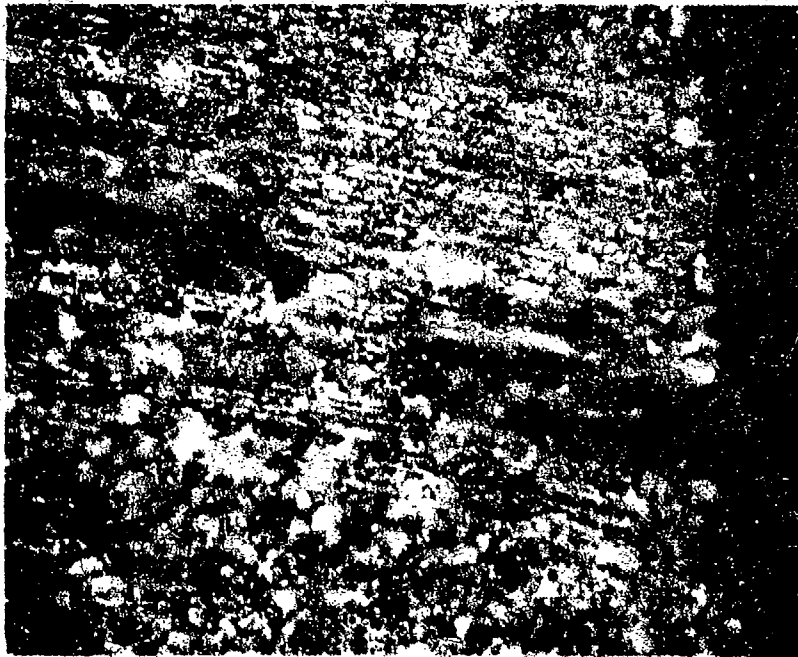
Figure 73 Voids in specimen C-4 exposed to 90-micron
sand (110x).

Figure 74 Cross-section of exposed void (110X).

The region just below the eroded surface was investigated in greater detail in order to asses the extent of the interaction between the impulsive loadings on the surface and voids near the surface. No interaction effects were observed in the cross sections examined. No cracks were found connecting the voids with the surface for the sand particle impacts.

5.0 GENERAL DISCUSSION

The analysis of multiple direct impacts of glass beads on glass plates can now be advanced on the basis of the microscopic observations and the general form of the weight-loss data. It was found that the volume of material removed from the specimen at any time t could be divided into three components as indicated in Eq. (2)

$$\Delta V(t) = \Delta V_1(t) + \Delta V_2(t) + \Delta V_3(t)$$

The explicit form of $\Delta V_1(t)$ was derived in Section 3.2.2

$$\Delta V_1(t) = \eta D \int_0^t K_1(t-\tau) g(D) n \varphi(\tau)(1 - \Delta A_1(\tau) - N(\tau)A_0) d\tau \qquad (17)$$

where $\Delta V_1(t)$ is the volume of material removed per unit surface area of the specimen. The growth-rate function $K_1(t)$ denotes the rate at which area is removed once a pit is nucleated and the sum of the remaining terms in Eq. (17) represents the number of pits nucleated per unit area. Means for obtaining the parameters appearing in Eq. (17) were described in Section 3.2.3.

As the exposure of the specimen continues a time will eventually be reached when the volume of the specimen assigned to $V_1(t)$ will be exhausted. If this value of the exposure time is denoted by t_1^*, then

$$\lim_{t \to t_1^*} \Delta V_1(t) = \eta D \qquad (41)$$

in accordance with Eq. (12). This condition requires that the integral in Eq. (17) equals unity when $t = t_1^*$. We further note that at this time

$$\Delta A_1(t_1^*) = 1 - N(t_1^*)A_0 \qquad (42)$$

where $N(t_1*)$ is the number of frustrums protruding from the surface of the specimen per unit area and A_0 is the average area of the ring fractures on the specimen's surface.

On the basis of the experimental observations, volume is not removed from the conical frustrums until the surrounding material has been removed. A reasonable form for $\Delta V_2(t)$ is

$$\Delta V_2(t) = \int_{t_1}^{t} K_2(D) n \varphi_2(t-\tau) \Delta A_1(\tau) d\tau \qquad (43)$$

The lower limit in the integral can be set equal to zero, however in some cases it may be advantageous to have a non-zero value. The function $K_2(D)$ is the time rate of volume removed per nucleated fracture resulting in material removal from an exposed conical frustrum. The sum of the remaining terms in Eq.(43) represents the number of critical fractures nucleated per unit area. The probability function $\varphi_2(t)$ is time-dependent, since it is found that a protruding frustrum becomes more susceptible to decomposition after a distribution of fractures develops within it due to repeated particle impacts. A second time-dependent factor has been incorporated into $\varphi_2(t)$ which is the fact that only a portion of the area occupied by the frustrums receives direct impacts from the glass beads due to the geometry of the frustrum distribution as shown in Fig. 6(c). As the cones disintegrate an increasing area is exposed to direct impacts. An appropriate term for the function $\varphi_2(t)$ would be a sigmoidal shaped curve which asymptotically approaches a constant value φ_* which is always less than or equal to unity. The constant value of φ_2 is reached when the surface of the specimen is highly fractured and small fragments are easily removed. At an exposure time t_1*, ΔA_1 reaches the constant value indicated in Eq.(42). Similarly, there will be a time when φ_2 is also constant, then Eq.(43) becomes

$$\Delta V_2(t) = \int_{t_1}^{t} K_2(D) n \varphi_2^* (1 - N(t_1^*) A_o) d\tau$$

$$= K_2(D) n \varphi_2^* (1 - N(t_1^*) A_o)(t - t_1) = (\text{const.})(t - t_1) \quad (44)$$

or the volume removed asymptotically approaches a linear func-
tion of time. A constant rate of material removal is found
to prevail as evidenced in the form of the weight-loss data
once most of the material has been removed from the surface
layer of the specimen. As the exposure to the erosive envi-
ronment continues, a point is reached where the entire surface
layer to a depth D is removed, then

$$\lim_{t \to t_2^*} \Delta V_2(t) = (1 - \eta) D \quad (45)$$

In the derivation of Eq. (43) we have assumed that all
the fragments removed from the surface of the specimen have
the same volume at all stages of the frustrum decomposition
and that the surface area of the specimen which participates
in the erosion process can be represented by $\Delta A_1(t)$. This
latter assumption is only an approximation to the actual
conditions, however it becomes quite involved to include an
estimate of the frustrums included in the area ΔA_1 for any
generic time t. This leads to the limiting form of $\Delta V_2(t)$
in Eq. (44) where, in a more realistic representation $(1 - N(t_1^*)
A_o)$ should be replaced by unity.

The microscopic investigations do not indicate that
there is a distinction between the removal of material from
the bulk specimen and that near the base of the frustrums.
This observation implies that

$$\Delta V_3(t) = \int_{t_2}^{t} K_2(D) n \varphi_2^* \Delta A_2(\tau) d\tau \quad (46)$$

where the lower limit is again taken to be a non-zero value
signifying the exposure time when this final phase of the

erosion process becomes operative. The exposed surface area, $\Delta A_2(t)$, at the base of the surface layer is difficult to describe. The following approximation is introduced into Eq.(46),

$$\Delta A_2(t) = \frac{\Delta V_2(t)}{(1-\eta)D} \qquad (47)$$

When $\Delta V_2 = \Delta V_2(t_2^*)$, $\Delta A_2(t) = 1$. Hence after the surface layer has been removed

$$\Delta V_3(t) = K_2(D)n\varphi_2^*(t-t_2) \qquad (48)$$

which is simply a linear function of time and a continuation of the latter stages of the erosion process contributing to $\Delta V_2(t)$. The evaluation of all the parameters appearing in ΔV_3 in Eq.(46) will be made in conjunction with Eq.(43).

The volume removed from the specimen, or equivalently the weight-loss, can be computed once the parameters appearing in Eq.(17), (43), and (46) are known. The required data and its acquisition for evaluating Eq.(17) was described in Section 3.2.3. The additional parameters introduced in Eq.(43) and (46) are $K_2(D)$ and $\varphi_2(t)$.

The expression for the fracture cone penetration depth D given in Eq.(24) shows that it is related to the impact velocity, the radius and density of the impacting beads, and the elastic constants for the bead and target materials through the Hertzian theory of impact. The magnitude of D is a function of the properties of the specimen in its initial state. However the functions K_2 and φ_2 are related to the highly-fractured surface of the specimen during the final stage of the erosion process as shown in Fig.6(d). It is very difficult to ascribe mechanical properties to the highly-eroded surface, so that at the present time K_2 and φ_2 will have to be evaluated experimentally. Future work will explore suitable analytical representations for these functions.

The above model is applicable to oblique impacts by glass beads, since no significant differences were observed in the general form of the erosion characteristics for this case. The weight-loss data indicated that, under nearly equivalent conditions used in the case of direct impacts, the magnitude of the weight loss at the same normal velocity and exposure times was two to three times greater for the oblique impact as compared to direct impact. The ring fracture diameters were found to be approximately equal for both impact conditions and in general agreement with the values of the maximum contact diameters calculated from the Hertzian theory of impact, however the penetration depths of the cone fractures were noticeably less for the oblique impacts especially as the impact velocity increased. It is concluded, for a reason yet to be discovered, that the differences in the weight loss data are due to a greatly increased probability for producing ring fractures for oblique impacts. However these differences can be readily assimilated in the general modeling context developed for direct impacts.

The direct and oblique impacts of irregularly-shaped solid particles dictates that more extensive modifications of the basic analytical model are required. At moderate impact velocities each particle is capable of removing material from the surface of the target. The weight-loss data indicate that a steady-state erosion rate is established after a very short incubation period. The irregularities in the weight-loss data for both direct and oblique impacts during the incubation period require additional research for clarification. For both impact conditions the normal component of the particle impact velocity was held constant, and it was found that the steady-state erosion rates were nearly indentical. The slightly greater values in Table IX for the oblique impacts may be due to the fact that the specimen receives approximately 30 percent more particle impacts per revolution in this case as indicated by the estimates provided in

Table V. However microscopic examination of the erosion damage occurring during the early stages of the erosion process did not reveal any significant difference between the direct and oblique impacts.

Due to the short duration of the incubation period and the rapid approach to a uniform rate of material removal, a general relation of the form given in Eq.(48) is an appropriate description of the weight-loss data. Of course, the form of the coefficients on the right-hand side of Eq.(48) will have to be modified. Some guidance in this regard will be obtained from the explicit form developed in the case of the 70-micron glass beads. However the characterization of irregularly-shaped particles in a manner suitable for incorporation into Eq. (48) has to be considered if this relation is to have general applicability. While it is possible to obtain statistical data pertaining to the size of irregularly-shaped particles, it is a very difficult task to obtain appropriate representations of particle shape as indicated in Section 3.4.1. The lack of an adequate representation for the particle shape was pointed out as a contribution to the failure of the correlation between the erosion rates and a simple model developed by Head and Harr.[16] This does not exclude consideration of the material properties of the irregularly-shaped particles which will also have a significant effect on the erosion rates. These problems require additional attention.

The derivations of a general theory for the erosion of glass plates by glass beads indicates the way in which the material properties, particle characteristics, and impact parameters influence the material removal process. While glass beads are not an erosive medium commonly encountered in practice, the mathematical analysis of the impact of glass beads on the pristine surface of the glass plates can be given in considerable detail. The more highly eroded the

-173-

surface of a brittle material becomes, the original surface
conditions no longer prevail and the problem is less suscep-
tible to mathematical analysis. However the value of the
above approach is that it provides insight into the general
structure for a predictive erosion theory and allows every
feature of the basic model to be more explicit than would be
possible in a more complex erosion process. The complexity
of the material response and erosive medium will be increased
as in our exploratory investigations of sand and liquid par-
ticle impacts on glass plates.

A means for evaluating the pressure distribution imparted
to a deformable surface by a spherical liquid drop was out-
lined in Section 3.5.1. The transient stress distributions
with an elastic half-space corresponding to the applied pres-
sure pulse can be determined in an approximate way using
Blowers' analysis.[32] It is estimated, on the basis of the
limited numerical data available, that the intensity of the
disturbances propagating into the elastic medium due to a
2mm drop impacting the elastic body at velocities up to 1000 fps
are considerably less severe than the results obtained from
simple, one-dimensional analyses would indicate. It cannot
be established that the transient stress distributions due
to a spherical liquid drop impacting a deformable surface can
be represented in terms of the equilibrium stress distributions
shortly after the drop first touches the surface as suggested
by Peterson[36] until after additional numerical calculations
employing the approach described in Section 3.5.1 have been
completed for contact times in the vicinity of $1\mu s$. The
results from the analysis of the transient stresses due to
liquid drop impacts on deformable materials will replace the
Hertzian analysis, if necessary, in the erosion modeling
studies, so the rain erosion of brittle materials can be
considered. The erosion tests established that material remo-
val from glass plates in a rain environment was a preferential
process of pit nucleation and growth, therfore the erosion
process conforms with the basic premise of our general erosion
model.

The erosion process for a typical, brittle material can be considered in terms of two major subdivisions: the incubation period and the period of uniform material removal. The erosion resistance of a specific material class can be improved in two ways. Once the material parameters affecting the removal of material in the incubation period are identified, they can be selected so the duration of the incubation period is extended. This means that the magnitude of the weight loss at a particular exposure time will be less for the modified material than for the original material. The second way to improve the erosion resistance is to select materials which have material properties that decreased the magnitude of the steady-state erosion rates. If the operative erosion mechanism during the incubation period is the same as that in the period when the steady-state erosion rate is achieved, then modification of the material parameters associated with material removal in the incubation period will also influence the steady-state erosion rates. This would be true for the solid particle erosion of brittle and semi-brittle materials. Hence, understanding and analyzing the events leading up to the initiation of material removal is a viable approach to prescribing the material characteristics which affect erosion behavior.

The erosion mechanisms have been identified for the UHMW polyethylene and the graphite-fiber reinforced epoxy specimens as described in Section 4.1 and 4.3. The sand erosion of UHMW polyethylene is due primarily to the cutting action of the irregularly-shaped particles striking the surface of the aerodynamically-shaped specimens away from the leading edge. The direct impacts of the sand particles along the leading edge simply produce permanent indentations in the polyethylene, but this process is not as effective in removing material. The sand erosion of the graphite-fiber reinforced epoxy specimens did not exhibit a significant angular dependence; material removal from the surface was

-175-

equally effective for both direct impacts and cutting deformations.

The rain erosion mechanisms for the graphite-fiber reinforced epoxy are particularly interesting. The process of material removal results from the following sequence of events. A water drop striking the specimen's surface will crack the epoxy surface layer through direct impact or upon impacting in one of the pre-existing shallow depressions on the surface. The cracks propagate along the fiber/matrix interface whenever possible which is an area of weakness in the composite structure. Small pitted regions appear on the specimen's surface. Additional cracks exist within the pits and are enlarged through the pressures applied by the direct impact and lateral outflow from drops striking in the vicinity of the cracked area. These loadings momentarily force the two faces of the crack apart and it extends further into the matrix material. The fracture mode in both the initiation stage of crack development and the penetration of cracks into the matrix corresponds to mode I deformations. Longitudinal cracks lying parallel to the direction of the carbon fibers are readily found on the eroded surface. Eventually large cracks penetrate the composite isolating small bundles of fibers and matrix which ultimately are only attached to the specimen at the ends of a short segment. The isolated bundles may consist of a few fibers or be composed of a grouping which is five to ten layers thick and an equivalent range in breadth. Additional droplet impacts penetrate the severed region below the small segment and force it outward from the surface. At this point the freed segment can be thought of as a rectangular beam fixed at both ends and loaded by a distributed load on one of its longitudinal faces. Removal of the segment results through fracture at its ends. It has not been determined whether the bending or transverse shear stresses represent the most severe condition.

The microscopic observation of the eroded surface and the above reasoning lead to two important aspects of the material removal process. First the fracture toughness for mode I deformations of the epoxy matrix should control the initiation of the fracturing process. It is only the mechanical behavior of the matrix material and not the mechanical properties of the composite which govern the fracture behavior under these conditions. However, it must be remembered that the fracture surface tends to propagate along the matrix/ fiber interface, so the bond established between these two components of the composite introduces a locally weakened area in the otherwise homogeneous matrix material. Secondly, the initial removal of small segments of the composite involves either mode I or mode II deformations, but in this case the crack is propagating in a direction transverse to the longitudinal fiber axes. The fracture toughness values must therefore correspond to this condition. This process continues as described in Section 4.3.1.

Having established the fundamental mode of failure of the composite at an intermediate to advanced stage of the erosion process, a micromechanical model can be developed which reflects these findings in quantitative terms. The first approximation provided here greatly simplifies the actual state of affairs. A number of conjectures must be introduced in order to arrive at a manageable problem. A meaningful analytical approach will be developed in future research on composites.

The nickel-coated composite specimens exposed to a sand environment failed by a loss of adhesion at the interface between the coating and the substrate. The coating then wrinkled as seen in Fig. 57 and 58. The average thickness of the coating was initially 3 mils for specimen D-3-3 and somewhat less than 6 mils for specimen D-6-6. On the basis of the weight loss for each specimen at the time the coatings

buckled and the area of the specimen exposed to solid particle impacts, the uniform reduction in the coating thickness is only on the order of a few tenths of a mil which would hardly reduce the thickness of the 6 mil coating to a critical thickness comparable to that for the 3 mil coating. The buckled pattern shown in Fig. 57 and 58 is identical to the buckling mode for a thin cylindrical shell of ductile metal subjected to uniaxial compression. This observation implies that there is a loss of shear resistance at the interface. It would seem that the centrifugal forces acting on the specimen when it is whirling at the end of the rotating arm in the AFML-Bell erosion facility contribute to the failure in this case. Although our calculations showed that the average thickness of the 3 and 6 mil coating did not reach the same critical value before failure occurred, the centrifugal force acting on the 6 mil coating would be greater than that acting on the 3 mil coating. The critical coating thickness would therefore have to be computed accounting for this difference. Support for our conjecture that sand erosion reduces the nickel coating to a critical thickness for both coating thicknesses is obtained by comparing the different failure modes found in the rain erosion tests, Fig. 50 and 54, where no measurable weight loss was recorded.

The research conducted within this program led to several preliminary concepts for erosion modeling studies in a variety of materials. The proposals made here will be developed in future research. The analytical modeling of significant features of the operative erosion mechanisms at various stages of the erosion process is beginning to establish the connection between material properties and the erosion behavior of specific material systems.

6.0 CONCLUSIONS

- The explicit form for a complete erosion theory has
  been derived for direct and oblique impacts of
  glass beads on glass plates. Future research will
  concentrate on replacing experimentally-determined
  parameters appearing in this theory with analytical
  expressions containing the impact parameters and
  material properties of the eroding particles and
  target.

- Exploratory investigations were initiated for the
  direct and oblique impacts of sand particles on
  brittle materials. A theory of erosion will be
  developed for these conditions based on the experi-
  mental observations and the explicit form of the
  theory for brittle materials eroded by small
  spherical particles.

- Advancement has been made in evaluating the transient
  stress distribution in an elastic half-space sub-
  jected to a time- and spatially-dependent pressure
  locally applied to its surface and approximating a
  liquid drop impact. The results obtained from
  this analysis will be used to extend the erosion
  model to liquid drop impacts.

- Erosion tests confirmed that the rain erosion of glass
  plates was a pit nucleation and growth process, and
  therefore glass plates provide an ideally brittle
  response for extension of the basic erosion model
  to liquid drop impacts.

- The erosion mechanisms for UHMW polyethylene exposed
  to sand and rain erosion have been identified.
  Material removal by sand erosion is due primarily

to the cutting action of the particles striking
the target obliquely. Rain erosion of UHMW poly-
ethylene is a highly preferential process of pit
nucleation and growth which conforms to the basic
hypothesis used in the erosion modeling studies of
brittle materials.

• The erosion of nickel-coated glass-fiber reinforced
epoxy specimens requires further investigation.
It is suggested that an interaction occurs between
the centrifugal forces applied to the specimen on
the rotating arm and the stability of the reduced
coating thickness as material is eroded from the
surface. The shear resistance at the coating/sub-
strate interface appears to be quite low, and an
analysis based on the buckling of a thin cylindri-
cal shell in compression is proposed. A different
form of failure, cracking and localized pitting of
the coating, was found for rain erosion. The
weight loss was negligible in this case, and the
buckling instability did not appear. In general,
the stress wave interactions at the coating/sub-
strate interface due to locally applied pressure
pulses on the surface for both sand particles and
rain drops should be considered in understanding
adhesion failures for coatings.

• The erosion mechanisms for graphite-fiber reinforced
epoxy specimens exposed to sand and rain erosion
have been identified. The rate of material removal
by sand is the same due to direct deformation and
the cutting action of the particle striking obliquely.
In this regard the nature of the erosion process
is the same as that for glass plates eroded by sand
particles. The analytical description of the latter
case will therefore be directly applicable to the

sand erosion of the composite material which behaves
in a brittle manner. The rain erosion mechanisms
were quite different from the mechanisms associated
with sand. A significant material property which
affects the erosion behavior is the fracture tough-
ness of the epoxy matrix and the composite material.
A micromechanical model is proposed for relating
fracture toughness to the erosion process.

7.0 REFERENCES

1. Adler, W. F. and Sha, G. T., Analytical Modeling of Subsonic Particle Erosion, AFML-TR-72-144 (July 1972).

2. Tsai, Y. M. and Kolsky, H., "A Theoretical and Experimental Investigation of the Flaw Distribution on Glass Surfaces", J. Mech. Phys. Solids, 15, 29 (1967).

3. Benbow, J. J., "Cone Cracks in Fused Silica", Proc. Phys. Soc. (London). 75, 697 (1960).

4. Bowden, J. P., and Field, J. E., "The Brittle Fracture of Solids by Liquid Impact, by Solid Impact, and by Shock," Proc. Roy. Soc. (London), A282, 331 (1964).

5. Hamilton, B., and Rawson, H., "The Determination of The Flaw Distribution on Various Glass Surfaces from Hertz Fracture Experiments", J. Mech. Phys. Solids, 18, 127 (1970).

6. Roesler, F. C., "Indentation Hardness of Glass as an Energy Sealing Law", Proc. Phys. Soc. (London), B69, 55 (1956).

7. Roesler, F. C., "Brittle Fracture Near Equilibrium," Proc. Phys. Soc. (London), B69, 981 (1956).

8. Finnie, I., "The Mechanism of Erosion of Ductile Metals", Proc. Third U.S. National Cong. Appl. Mech., New York: American Society of Mechanical Engineers, 1958, 527.

9. Finnie, I., "Erosion of Surfaces by Solid Particles", Wear, 3, 87 (1960).

10. Bitter, J. G. A., "A Study of Erosion Phenomena, Parts I and II," Wear, 6, 1969 (1963).

11. Nielson, J. H. and Gilchrist, A., "Erosion of A Stream of Solid Particles," Wear, 11, 111 (1968).

12. Hausner, H. H., "Characterization of the Powder Particle Shape", Particle Size Analysis, London: The Society of Analytical Chemistry, 1967, 20.

13. Heywood, H., Discussion of Reference 7, ibid, p. 27.

14. Kaye, B. H., "Some Aspects of the Efficiency of Statistical Methods of Particle Size Analysis", Powder Technology, 2, 97 (1968/69).

15. Head, W. J., Pacala, T., and Poole, J., Final Report on Phase I of Allison-Purdue Dust Technology Program, Paper presented at the Man-Mobility-Serviceability Forum, April 11-12, 1967, General Motors.

16. Head, W. J. and Harr, M. E., "The Development of a Model to Predict the Erosion of Materials by Natural Contaminants", Wear, 15, 1 (1970).

17. Lineback, L. D., Head, W. J., and Manning, C. R., "Modification and Extension of a Model for Predicting the Erosion of Materials", paper presented at the Forum on Gas Turbine Erosion Problems, Sponsored by the ASME and ASTM, San Francisco, California, March, 1972.

18. Heywood, H., Small Particle Statistics New York: Elsavier Publishing Company, 1953.

19. Jenkins, D. C., and Booker, J. D., "The Impingement of Water Drops on a Surface Moving at High Speed", in Aerodynamic Capture of Particles, E. G. Richardson (Editor). New York: Pergamon Press, 1960.

20. Bowden, F. P. and Brunton, J. H., "The Deformation of Solids by Liquid Impact at Supersonic Speeds," Proc. Roy. Soc. (London), A263, 433 (1961).

21. Field, J. E., Camus, J. J., and Gorham, D. A., "Single Impact Erosion Processes", Proc. Third Int. Conf. on Rain Erosion and Associated Phenomena, Elvetham Hall, Hampshire, England (August 1970) 303.

22. Fyall, A.A., "Single Impact Studies with Liquids and Solids", Proc. Second Conference on Rain Erosion, Meersburg, West Germany (August 1967).

23. Brunton, J. H. and Camus J. J., "The Flow of a Liquid Drop During Impact", Proc. Third Int. Conf. on Rain Erosion and Associated Phenomena, Elvetham Hall, Hampshire, England (August 1970) 327.

24. Engel, O.G., "Waterdrop Collisions with Solid Surfaces", J. Res. Nat. Bur. Stand., 54, 281 (1955).

25. Hancox, N. L., and Brunton, J. H., "The Erosion of Solids by the Repeated Impact of Liquid Drops", Phil. Trans. Royal Soc. London, A260, 121 (1966).

26. Heymann, F. J., "On the Shock Wave Velocity and Impact Pressure in High-Speed Liquid-Solid Impact", J. Basic Engng., Trans. ASME, 90B, 400 (1968).

27. Heymann, F. J., "High-Speed Impact Between A Liquid Drop and a Solid Surface", J. Appl. Phys., 40, 5113 (1969).

28. Morris, J. W., Jr., "Mechanistic Investigation of Rain Erosion", AFML TR-69-287, Part II, September 1969.

29. Huang, Y.C., "Numerical Studies of Unsteady, Two-Dimensional Liquid Impact Phenomena", Ph.D. Dissertation, Department of Mechanical Engineering, University of Michigan, (1971).

30. Huang, Y.C., Hammitt, F., and Yang, W. J., "Hydro-dynamic Phenomena During High-Speed Collision Between Liquid Droplet and Rigid Plane," Paper No. 72-WA/FE-30 presented at the Winter Annual Meeting of the American Soc. Mech. Engrs., New York (November 26-30, 1972).

31. Tyler, L. D., "The Flow Dynamics of a Liquid Drop During High-Speed Impact", Bull. American Physical Soc., 16 (11), 1319 (1971).

32. Blowers, R. M. "On the Response of an Elastic Solid to Droplet Impact", J. Inst. Maths. Applics., 5, 167 (1969).

33. Chu, Boa-Teh, "Finite Amplitude Waves in Incompres-sible Perfectly Elastic Materials", J. Mech. Phys. Solids, 12, 45 (1964).

34. Bland, D. R., "Dilatational Waves and Shocks in Large Displacement Isentropic Dynamic Elasticity", J. Mech. Phys. Solids, 12, 245 (1964).

35. Davidson, L., "Propagation of Plane Waves of Finite Amplitude in Elastic Solids," J. Mech. Phys. Solids 14, 249 (1966).

36. Peterson, F. B., "Some Consideration of Material Response due to Liquid-Solid Impact", Paper No. 72-WA/FE-27 presented at the Annual Winter Meeting of Amer. Soc. Mech. Engrs., New York, November 26-30, 1972.

37. Love, A. E. H., "The Stress in a Semi-Infinite Solid by Pressure on Part of the Boundary", Trans. Royal Soc. (London), A228, 377 (1929).

38. Eason, G., "The Displacements Produced in an Elastic Half-Space by a Suddenly Applied Surface Force", J. Inst. Maths. Applics., 2, 299 (1966).

39. Adler, W. F., Morris, J. W., Jr., and Wahl, N. E., Supersonic Rain and Sand Erosion Research: Characterization and Development of Erosion Resistant Materials, AFML-TR-72-85 (May 1972).

40. Weaver, J. H., Electrodeposited Nickel Coatings for Erosion Protection, AFML-TR-70-111 (July 1970).